UNIVERSITAT DE BARCELONA

Biochemical and mechanical changes of the extracellular matrix during lung metastasis

Maria Leonor Barreto Torres de Mendonça Narciso

UNIVERSITAT DE BARCELONA

BIOCHEMICAL AND MECHANICAL CHANGES OF THE EXTRACELLULAR MATRIX DURING LUNG METASTASIS

Doctoral thesis dissertation presented by

Maria Leonor Barreto Torres de Mendonça Narciso

to obtain a doctoral degree by the University of Barcelona in accordance with the requirements of the international PhD Diploma

Directed by:

Dr. Isaac Almendros López and Dr. Núria Gavara Casas

The Institute for Bioengineering of Catalonia (IBEC)

Unit of Biophysics and Bioengineering

Doctoral Programme in Medicine and Translational Research

Faculty of Medicine and Health Sciences, University of Barcelona

November 2022

Para os meus avós,

Álvaro, Antero, Orlinda e Luíza, por me guiarem e inspirarem.

Obrigada.

Acknowledgments

A PhD dissertation is not a work usually done in a vacuum and mine certainly was not. I am very grateful to have been supported by so many people throughout the last three years and I would like to mention a few.

Firstly, I would like to express my deepest appreciation to my supervisors, Dr. Isaac Almendros and Dr. Núria Gavara, for their support and invaluable feedback. Both encouraged and trusted my scientific instincts at every step of the way, allowing me to grow as a researcher, for which I am deeply grateful. I would also like to extend my sincere thanks to Prof. Ramon Farré and Prof. Daniel Navajas who gave me this opportunity three years ago and have supported my work and growth ever since. Additionally, this endeavour would not have been possible without the generous support from the Marie Skłodowska-Curie fellowship, who financed my research and integrated me in a network of excellent scientists, where I learned so much. So, thank you Phys2Biomed.

Moving to Barcelona for my PhD would have been much harder if I had not found wonderful friends that made me feel at home while I was here. I am blessed to have met too many fantastic people to name, but I would like to highlight a few. To Irene, my first friend in Barcelona. You have held my hand through everything, from my first cockroach infested apartment to excruciating dentist appointments, I truly don't know what I would have done without you. To Alvaro, whose unwavering support could always turn my experimental disappointments into victories. I will forever keep a bag of frozen nuggets just in case you want to visit. To Esther, for being the best teacher and role model any first-year PhD student could ask for. I will be an accomplished scientist when I am as good as you. To África, whose kindness compelled her to stay in the lab until I left, resulting in many long nights that I will hardly ever forget. Thank you for teaching me Spanish and for helping me in countless experiments. I could not have undertaken this journey without Constança, my Portuguese comrade. We have done this PhD side-by-side, every step of the way, and your friendship has made it so much more fun. And finally, to Kate, which, besides being a magnificent friend, has had the patience to proofread this entire thesis. In her own words: "Without this woman, I don't know where this thesis would be, probably, it wouldn't be at all". I couldn't have said it better myself.

When I started my PhD in October 2019, I could not have imagined the (global) challenges that we were all about to face in the years ahead. Luckily, I had just joined an

incredibly supportive lab that was always ready to help out. A huge thank you to every single one of you at UBB, but specifically to Natalia, Ale, Anna, Hector, Nanthilde, Carol, Patri and Berni for your scientific wisdom, time and friendship. I truly believe this is a spectacular lab full of creative, hard-working, excellent scientists and I am excited to see what's to come for all of you.

I would also like to thank my mother, Cristina, my father, Francisco, and sister Madalena that kept me constant (virtual) company through the daily commutes to work, late experiments, and endless writing marathons. No matter the distance, they never let me feel alone. To the rest of my family, Catarina, Katya, Tio Jaime, Lula and Mathi who have listened to hours long conversations about immunostaining and biomechanics with tremendous patience, thank you for being my relentless cheerleaders.

I would be remiss in not mentioning the people that specifically supported me in the last month of my PhD thesis and dragged me over the finish line. Besides the family and friends I've already mentioned, I want to thank Ameera and Geri for all the tea and talks, Joana for the kindness and selflessness and David for the Mario kart and patience. I would probably still be writing the thesis without your help.

Finally, I would like to thank João, who unconditionally and passionately supported my dreams even when they took me far away from him, which is the greatest act of love one can ask for. There will never be enough words to thank you.

Funding

Maria Leonor Narciso was funded by the H2020 European Research and Innovation Programme under the Marie Skłodowska-Curie grant agreement “Phys2BioMed” contract no. 812772.

Table of Contents

Index of Figures

Abbreviations and Acronyms

3D: three-dimensional

AFM: atomic force microscopy

APTES: (3-Aminopropyl)triethoxysilane

BM: basement membrane

CAF: Cancer-associated fibroblasts

CHAPS: 3-[(3-Cholamidopropyl) dimethylammonio]-1-propanesulfonate

CT: Computerized tomography

DAPI: 4′,6-diamidino-2-phenylindole

DNAse: Deoxyribonuclease

ECM: extracelular matrix

EMT: Epithelial to mesenchymal transition

FGF: Fibroblast growth factor

GAGs: Glycosaminoglycans

H&E: Hematoxilin and eosin

IM: Interstitial matrix

IPF: Idiopathic pulmonary fibrosis

LOX: Lysyl oxidase

MMP: Metalloproteinase

MPM: Malignant pleural mesothelioma

MRI: Magnetic Resonance imaging

NSCLC: Non-small cell lung cancer

NTD: Nintedanib

PDGF: Platelet-derived growth factor

PD-L1: Programmed death-ligand 1

PDT: Photodynamic therapy

PET: Positron emission tomography

PFD: Pirfenidone

PG: Proteoglycan

RNAse: Ribonuclease

SCLC: Small cell lung cancer

SD: Sodium deoxycholate

SDS: Sodium dodecyl sulfate

SEM: Scanning Electron Microscopy

TAF: Tumor-associated fibroblasts

TIMP-1: Tissue inhibitors of metalloproteinases

TME: Tumor microenvironment

VEGF: Vascular endothelial growth factor

List of Articles that comprise the Thesis

Thesis in the form of a compedium of articles. This thesis is comprised of four objectives and four articles (three published and one unpublished).

Article 1

Authors: **Maria Narciso**, Anna Ulldemolins, Constança Júnior, Jorge Otero, Daniel Navajas, Ramon Farré, Núria Gavara and Isaac Almendros.

Title: “Novel Decellularization Method for Tissue Slices”

Name of journal, year, volume and pages: Frontiers in bioengineering and biotechnology, 2022, Pages 271

Impact factor and quartile: 6.064, Q1 in Biomedical Engineering (JCR, 2021)

Article 2

Authors: **Maria Narciso**, Anna Ulldemolins, Constança Júnior, Jorge Otero, Daniel Navajas, Ramon Farré, Núria Gavara and Isaac Almendros.

Title: “A fast and efficient decellularization method for tissue slices”

Name of journal, year, volume and pages: Bio-protocol, 2022, nº22, pp. e4550-e4550

Impact factor and quartile: Not available as of 2022

Article 3

Authors: **Maria Narciso**, Jorge Otero, Daniel Navajas, Ramon Farré, Isaac Almendros and Núria Gavara.

Title: “Image-Based Method to Quantify Decellularization of Tissue Sections”

Name of journal, year, volume and pages: International Journal of Molecular Sciences, 2021, Volume 22, Issue 16, Pages 8399

Impact factor and quartile: 6.208, Q1 in Biochemistry and Molecular Biology (JCR, 2021)

Article 4

Authors: **Maria Narciso,** Africa Martinez, Constança Júnior, Massimiliano Berardi, Natalia Diaz-Valdivia, Anna Uldemolins, Kate Neal, Daniel Navajas, Ramon Farre, Jordi Alcaraz, Isaac Almendros and Núria Gavara

Title: “Lung Micrometastases Display ECM Depletion and Softening While Macrometastases Are 30-Fold Stiffer and Enriched in Fibronectin”

Name of journal, year, volume and pages: [submitted to] TBD

Impact factor and quartile: TBD

Thesis Summary

The mechanical properties of a tumor play an important role in cancer progression and therapeutic response. In fact, the stiffening of the tumor microenvironment has been linked to therapy resistance and an increased invasive behaviour. It is well-known that tumors are stiffer than their surrounding microenvironment, and recent data showing that the overexpression of certain ECM proteins, such as collagen and laminin is linked to worst prognosis and decreased therapeutic success of clinical patients, suggest an important role of the ECM on cancer development. However, the contribution of the mechanical properties of the cancer ECM during metastasis formation has not been studied in detail due to experimental limitations. In this doctoral thesis, we hypothesised that the mechanics of the ECM of lung metastases evolves during tumor growth and depends on the primary tumor site. Consequently, we set out to characterize biochemically and mechanically the ECM of lung metastases from different primary tumors and in response to anti-fibrotic treatment, specifically to nintedanib. To perform this study, we developed a novel decellularization procedure that efficiently produces acellular lung metastases sections while also preserving the tissue mechanics and the ECM's biochemical components. The optimal decellularizing agent was determined by comparing reagents from six pre-existing decellularizing protocols with different methodologies in terms of ECM preservation, sample attachment and decellularization efficiency. This last parameter is customarily assessed by using DNA quantification kits, but we decided to develop a cheaper, quicker, and more practical alternative: an automated image-based algorithm in Python that can analyse dozens of images in minutes, as well as quantify other fluorescent images after immunostaining, thus also providing information on matrix preservation. With the combination of these two techniques, we were able to quantify the DNA remaining on the sample after decellularization, quantify ECM proteins before and after decellularization, and thus select sodium deoxycholate as the best option for 'on-slide decellularization'. This protocol was applied to lung sections from mice injected with either mouse melanoma cells (B16F10) or Lewis lung Carcinoma cells (LLC1) that metastasized to the lungs. To measure ECM stiffness, we carried out force-indentation measurements using Atomic Force Microscopy (AFM) on

decellularized lung sections where tumors were identified. Decellularized metastases displayed distinct ECM structures that were similar in both models: a surrounding capsule, an interior dense ECM and a partially empty cavity where cancer cells used to be and where ECM was scarce. However, tumors from lung carcinoma (CAR) and melanoma (MEL) lung metastases showed different invasion phenotypes: CAR metastases infiltrated nearby tissues, forming tumor infiltration areas (TIA) while MEL metastases spread to different areas of the tumors, giving rise to micrometastases. Both these areas (TIA and micrometastases) represent the early stages of tumor invasion and showed a softening of the ECM (0.21±0.11kPa and 0.21±0.05kPa, for CAR and MEL, respectively), when compared to healthy lung ECM (0.42±0.09 kPa), as well as a depletion in collagen IV, collagen I and laminin, but a slight increase in fibronectin. The ECM from CAR macrometastases was more than 4x stiffer (1.79±1.32 kPa) than healthy lung ECM (0.42±0.09 kPa), while also showing a stark increase in fibronectin deposition (267.8±55.3% of the healthy lung ECM fibronectin) and a reduction of collagen I and IV and laminin. The ECM of MEL macrometastases on the other hand, showed a 17x fold increase in stiffness (6.39±3.40 kPa) when compared to healthy tissue, while also displaying a sharp increase in fibronectin (249.2±85.0% of the healthy lung ECM fibronectin), slightly increased levels of collagen I, and reduced collagen IV and laminin. In an attempt to soften the MEL ECM, we decided to administer the anti-fibrotic and anti-angiogenic drug, nintedanib. However, nintedanib surprisingly led to a significant increase in ECM deposition from 6.3±6.4% to 26.4±12.3% of the tumor area, and a doubling in tumor ECM stiffness from 6.39±3.40kPa to 12.35±5.74kPa, with and without nintedanib treatment, respectively. Since this increase in ECM deposition was strongly correlated with a sharp increase in tumor necrosis, it implies a connection between tumor vascularization (or lack thereof) and ECM production. Overall, the results described in this work suggest that the tumor ECM mechanics change throughout tumor development and can be an indicator of underlying tumorigenic mechanisms. Additionally, tumor ECM is heavily influenced by the primary site of the tumor, as evidenced by the different ECM structures, stiffness and composition of the melanoma and lung carcinoma metastases.

Resumen (ES)

Las propiedades mecánicas del tumor desempeñan un papel importante en la progresión del cáncer y la respuesta terapéutica. De hecho, la rigidez del microambiente tumoral se ha relacionado con una mayor resistencia terapéutica y comportamiento invasivo. Es conocido que los tumores son más rígidos que su microambiente circundante y que datos recientes demuestran que la sobreexpresión de ciertas proteínas de la matriz extracelular (MEC), como el colágeno o la laminina, están relacionadas con un peor pronóstico y disminución del éxito terapéutico en pacientes; sugiriendo un rol esencial de la MEC en el desarrollo del cáncer. A pesar de ello, la contribución de las propiedades mecánicas de la MEC en cáncer durante la formación de la metástasis no ha sido estudiada en detalle, debido a las limitaciones experimentales que presenta. En esta tesis doctoral, se plantea la hipótesis de que la mecánica de la MEC en las metástasis pulmonares tiene una evolución durante el crecimiento del tumor y que depende de la localización del tumor primario. Por consiguiente, nos propusimos caracterizar bioquímica y mecánicamente la MEC de metástasis pulmonares de distintos tumores primarios y la respuesta al tratamiento antifibrótico con el fármaco nintedanib. Con el objetivo de llevar a cabo este estudio, desarrollamos un novedoso procedimiento de descelularización que produce eficientemente secciones de metástasis pulmonares acelulares, preservando, al mismo tiempo, la mecánica del tejido y los componentes bioquímicos de la MEC. El agente descelularizador óptimo se determinó comparando los reactivos de seis protocolos de descelularización preexistentes con diferentes metodologías de preservación de la MEC, fijación de la muestra y eficiencia de descelularización. Este último, se evalúa habitualmente mediante el uso de kits de cuantificación de ADN, sin embargo, decidimos desarrollar una alternativa más barata, rápida y práctica: un algoritmo totalmente automatizado basado en imágenes de Python con capacidad para analizar docenas de imágenes en minutos, así como cuantificar imágenes fluorescentes tras la inmunotinción, proporcionando así información sobre la conservación de la matriz. Con la combinación de estas dos técnicas, fuimos capaces de cuantificar el ADN presente en la muestra tras el proceso de descelularización, cuantificar proteínas de la MEC antes y después de la descelularización y también, seleccionar el desoxicolato de sodio como la mejor opción para realizar el protocolo

de descelularización sobre un portaobjetos de vidrio mientras las muestras están firmemente adheridas a este. Este protocolo se aplicó a secciones de tejido pulmonar de ratones inyectados con células de ratón (B16F10) o células de carcinoma de pulmón de Lewis (LLC1) que formaron metástasis en los pulmones. La rigidez de la MEC fue analizada mediante medidas de fuerza-indentación por Microscopía de Fuerza Atómica (AFM) en secciones pulmonares descelularizadas donde se identificaron los tumores. Las metástasis descelularizadas mostraron estructuras de la MEC diferenciales que fueron compartidas en ambos modelos: una cápsula circundante, una MEC interior densa y una cavidad mayoritariamente vacía donde se encontraban las células cancerosas y la MEC era escasa. Sin embargo, los tumores de metástasis pulmonares de carcinoma (CAR) y melanoma (MEL) mostraron fenotipos de invasión diferentes: las metástasis de CAR se infiltraron en tejidos cercanos, formando áreas de infiltración tumoral, mientras que las metástasis de MEL se extendieron a diferentes zonas de los tumores, dando lugar a micrometástasis. Ambas zonas representan las primeras etapas de la invasión tumoral y mostraron un reblandecimiento de la MEC (0,21±0,11kPa y 0,21±0,05kPa, para CAR y MEL respectivamente) en comparación con la MEC de pulmón sano (0,42±0,09 kPa), así como una disminución del colágeno IV, colágeno I y laminina, pero un ligero aumento de la fibronectina. La MEC de las macrometástasis de CAR fueron 4 veces más rígida (1,79±1,32 kPa) que la MEC del pulmón sano (0,42±0,09 kPa), al mismo tiempo que mostraba un marcado aumento de la deposición de fibronectina (267,8±55,3% de la fibronectina de la MEC del pulmón sano) así como, una reducción de los niveles de colágeno I y IV y de laminina. Por otro lado, la MEC de las macrometástasis de MEL, mostró un aumento de la rigidez 17 veces mayor (6,39±3,40 kPa) en comparación con el tejido sano, al mismo tiempo que mostraba un fuerte aumento de la fibronectina (249,2±85,0% de la fibronectina de la MEC del pulmón sano), un ligero aumento de los niveles de colágeno I y una reducción de los niveles de colágeno IV y la laminina. En un intento de suavizar la MEC de MEL, decidimos administrar el fármaco antifibrótico y antiangiogénico nintedanib. Sin embargo, éste sorprendió al provocar un aumento significativo de la deposición de ECM del 6,3±6,4% al 26,4±12,3% del área del tumor, y una duplicación de la rigidez de la ECM del tumor de 6,39±3,40kPa a 12,35±5,74kPa, sin y con tratamiento, respectivamente. Dado que este aumento de la deposición de MEC estaba fuertemente correlacionado con un fuerte aumento de la necrosis tumoral, implica una conexión entre la vascularización del tumor (o la falta

de ella) y la producción de MEC. Por lo tanto, concluimos que los resultados descritos en este trabajo sugieren que la mecánica de la MEC tumoral cambia a lo largo del desarrollo del tumor y puede ser un indicador de mecanismos tumorigénicos subyacentes.

Chapter I.

INTRODUCTION

Lung in health and malignancy

Lung structure in health

The lungs are one of the most vital organs in the human body. They are the major organ of the respiratory system and perform the exchange of oxygen and carbon dioxide between our body and the atmosphere. Atmospheric air enters through the nose into the conducting zone of the respiratory system, where no gas exchange takes place. This area starts in the trachea, into the bronchi up until the terminal bronchioles and it serves a purely conductive role, hence the name of the air volume it holds is called “dead space volume”. Terminal bronchioles divide into respiratory bronchioles that have some alveoli in their walls. Respiratory bronchioles will then divide into alveolar ducts, which are small tubes which open into alveolar sacs in their distal portion, which in turn are comprised of many alveoli (Figure 1). Clusters of alveoli form a respiratory functional unit called the acini. The amount of air that actually reaches the alveoli and is used for gas exchange is very reduced and is called the alveolar ventilation (1–4).

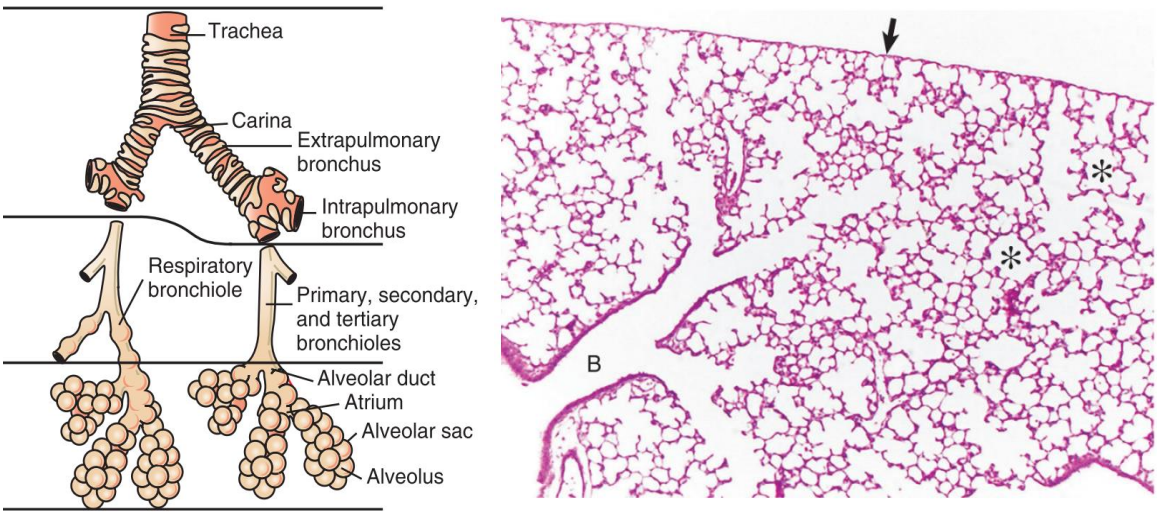

Figure 1 - *Lung structure in health. (Left) - Internal structure of the lungs, from the Trachea to the alveoli. (Right) – H&E-stained lung section from rats. B- bronchioles, * represent alveoli locations and the arrow indicate the pleura. Adapted from (1).*

The alveolar wall is a very thin membrane that separates the air compartment and the blood compartment (capillary lumen) and is composed of two distinct cell layers: an epithelium that faces the alveolar compartment and an endothelium that faces the capillary lumen. In between these two layers there is the interstitium and the three of them constitute the blood-air barrier (Figure 2). The alveolar epithelium is composed mainly of alveolar type I cells, which are squamous and line 95% of the alveolar surface, but also have single alveolar type II cells interspersed. Alveolar type II cells are cuboidal and are responsible for the secretion of surfactant, an important contributor to lung homeostasis. The secreted surfactant forms a layer in the alveolar compartment that stabilizes alveolar structure and helps prevent alveolar collapse by lowering surface tension. Surfactant also has immune functions since it interacts with pathogens, eliminates them and prevents their propagation (5). Finally, the interstitium is occupied by extracellular matrix (ECM) and cells, the most abundant being fibroblasts and myofibroblasts, but also interstitial macrophages and mast cells (1,6).

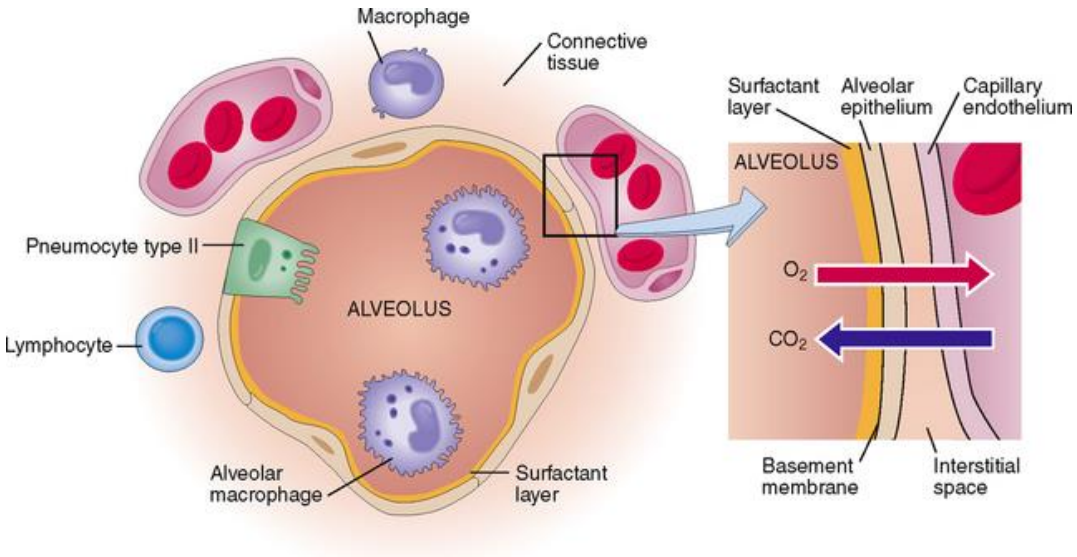

Figure 2 - *Alveolar structure and blood-air barrier. The alveolus is lined with alveolar type I and type II cells, lying on a basement membrane that separates them from the interstitial spaces around the alveolar capillaries. The interstitium is composed of fibroblasts, macrophages, and lymphocytes. Adapted from (4).*

Lung cancer

Lung cancer is one the world's largest health concerns that results from the neoplastic transformation of the lung epithelium. Lung cancer is the main culprit of all cancer related deaths, accounting for 22% of cancer mortality in 2021. Considering all stages and types, lung cancer has one of the lowest 5-year survival rates at only 21% (7). The main reasons for this high mortality rate are that 1) patients are diagnosed at a late stage of the cancer progression, due to the typical asymptomatic presentation of the disease in its early stages and are consequently diagnosed when the primary site has already metastasized, and 2) there are currently no curative treatment options (8). Risk factors for developing lung cancer include tobacco and smoking, exposure to asbestos and reduced air quality, lung damage after infection, and genetic factors (9). Lung cancer can be split into many subtypes, but the most relevant are malignant pleural mesothelioma (MPM), small-cell lung carcinoma (SCLC) and non-small cell lung carcinoma (NSCLC). NSCLC can be further classified as adenocarcinomas (50%), squamous cell carcinoma (40%). The remaining are attributed to less frequent cancer types (10%) (9–11).

Lung cancer diagnosis is typically performed by histological analysis of either tumor biopsies or from samples from resected tumors, after an initial discovery via one of many available imaging tools, including computed tomography (CT), magnetic resonance imaging (MRI) and positron emission tomography (PET) (8). To decide the best therapeutic course, it is not only important to classify the type of lung cancer but also to identify some molecular aberrations, markers and genetic mutations. There are four main treatment options for patients diagnosed with lung cancer: surgical intervention, radiotherapy, chemotherapy and biological/immunotherapy. Surgical intervention is the first line of treatment but unfortunately it is not an option for tumours too far advanced to be resected, resulting in what are called inoperable tumors. This is also the case for cancers that have already metastasized greatly. Chemotherapy and/or radiotherapy are options that

can help improve resectability for later operative intervention. However, they are also used as a second line of therapy after initial tumor resection. The specific compound used in chemotherapy will not only depend on the histological features of the tumor, but also on the genetic mutations of said tumor, since drugs that target the products of these mutated genes have been created for cancer treatment (8). Lastly, immunotherapeutic drugs such as pembrolizumab or nivolumab, which are antibodies against programmed death-ligand 1 (PD-L1), have shown great promise in the treatment of metastatic NSCLC (12–14).

Metastatic spread

Cancer diagnosis is commonly made when the primary tumor has already formed multiple secondary lesions, significantly complicating treatment options and worsening the disease prognosis. These secondary lesions are called metastases and they occur when cells from a primary tumor spread to either surrounding tissues or distant sites. When they occur, they are considered a hallmark of an aggressive cancer type and are linked to a significant increase in mortality (15).

When a tumor first starts to grow, its first necessity is to establish a viable blood supply that can provide nutrients and oxygen. Eventually, the growth rate of the tumor makes it impossible for the angiogenesis to keep up with the tumors' demands, resulting in intra-tumoral hypoxia and consequent cell death. At this stage, necrosis and hypoxia will induce some tumors to reduce their cell metabolism and division, but in others it will trigger invasion and metastasis (Figure 3). In hypoxic areas, specifically, epithelial to mesenchymal transition (EMT) is increased, a feature common to most metastatic cells. EMT is a phenomenon in which epithelial cells transform from organized, polarized into isolated mesenchymal-like cells with invasive properties (16,17). Since epithelial cells undergo apoptosis when they are no longer attached to matrix, EMT is necessary for metastatic invasion since cells need to detach from the ECM in order to invade other tissues. Once

the cell detaches from the primary site, it invades through the basement membrane of the ECM surrounding the tumor until it reaches lymphatic or blood vessels. There, the intravasion of the metastatic cells occurs into the lympathic/blood stream until they reach the target-organ, and the reverse process occurs. Once the metastatic cells arrive to their destination, the EMT is reversed, and they regain epithelial features (18,19).

Interestingly, there is mounting evidence that indicates that the tumor can prepare distant sites for metastatic spread even before any cells detach from the primary tumor site, forming so called “pre-metastatic niches” (20–22). It has been shown that in mouse models, primary tumors such as breast cancer, melanoma and colorectal cancer secrete extracellular vesicles that will prepare locations in the target-organ (e.g. the lung) for the accommodation of the new metastases. These factors and vesicles promote the production of growth factors, chemoattractants, ECM-modulatory proteins among other components meant to facilitate metastatic invasion and growth.

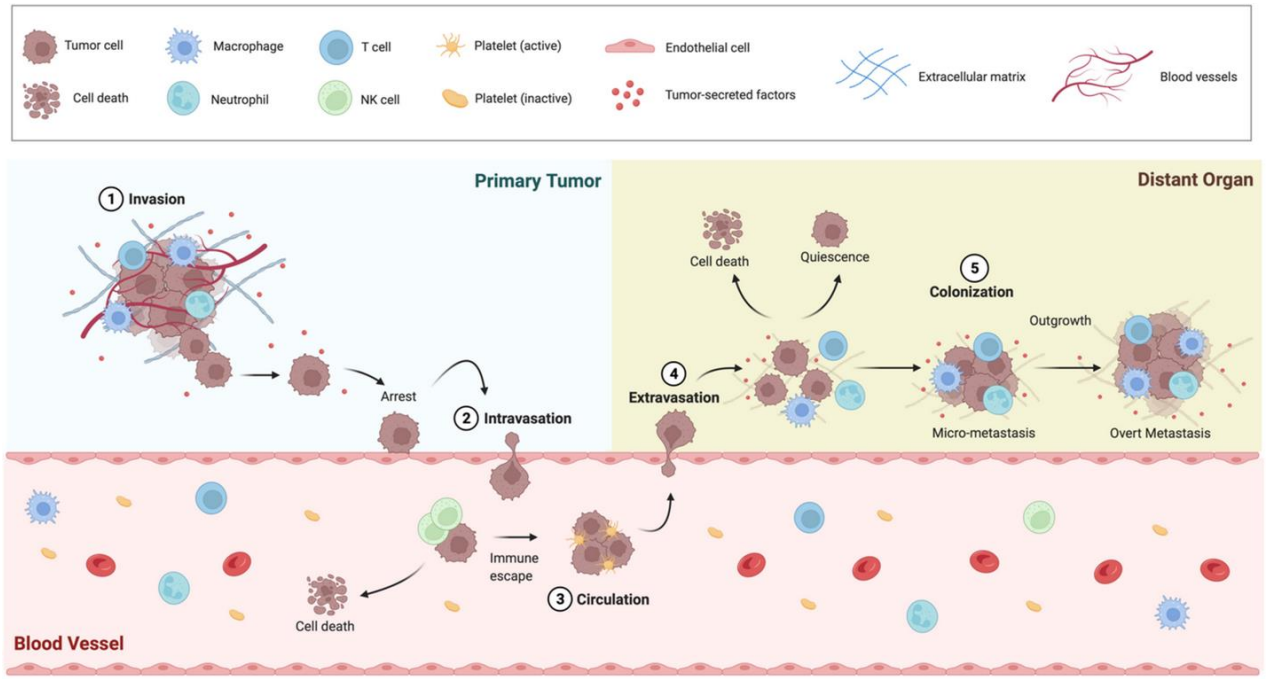

Figure 3 - *Metastatic Progression. The metastatic process starts with local invasion of the primary tumor towards the vasculature. After arriving to the capillaries, cells enter the circulatory system (intravasion). Circulating tumor cells (CTCs) are vulnerable to the attacks of the immune system. CTCs that manage to escape immune cells disseminate to secondary sites, following the circulatory fluid flow. Upon their arrival in the vasculature of secondary sites, CTCs extravasate and invade and settle in a pre-metastatic niche. At the metastatic site, the secondary lesion may be either eliminated or enter in a quiescent state. Once the cancer cells leave the dormant state, they reinitiate proliferation and tumor growth to form micrometastases and later complete tumors. Adapted from (15).*

Lung-seeking metastasis

Metastasis to the lungs is an extremely common phenomenon in cancer. In fact, pulmonary secondary tumors are the second most common type in metastatic cancer, accounting for 20-54% of all cases (23). This occurrence can be explained by many factors (24):

- **Easy access**: Metastatic cancer cells can reach the lungs through many different ways, including via lymphatic and blood vessels or through direct invasion from adjacent tissues.
- **Smoking**: it has been shown in both mice models and patients that smoking will increase the chances of developing lung metastases in breast carcinoma, esophageal cancer and colorectal cancer (24–26). This is due to the smoke-induced chronic inflammation that potentially contributes to metastasis formation and growth.
- **Immune activity of the lung**: lung alveolar type II cells recruit neutrophils through chemokine secretion. In turn, neutrophils support the proliferation of certain types of metastatic clusters. Some neutrophil secretions can also destroy anti-tumorigenic factors and thus promote metastases in the lung.
- **Genetic factors**: recently, genetic analysis has revealed some genes specifically associated with lung metastasis in animal models with breast cancer.

After leaving the primary tumor site and entering the blood stream, disseminated tumor cells enter the lung parenchyma by disrupting the lung endothelial layers. The most common origin for these secondary lung lesions includes colorectal cancer, head and neck cancer, breast cancer, urologic (kidney, ureter, prostate, testes) cancer and melanoma (22,24).

Lung Extracellular matrix

Extracellular matrix structure and composition

The extracellular matrix (ECM) is the acellular component to all tissues that provides physical and biochemical support to cells, tissues and organ architecture. The ECM is composed of an organized network of macromolecules whose exact composition and structure is tissue dependent. These structures can be made up from over 300 core structural components (27), which are mostly fibril-forming proteins but can also be made up of glycosaminoglycans which, when linked to proteins, form proteoglycans (PGs). There are two main compartments of the ECM: the basement membrane (BM) and the interstitial matrix (IM). The BM is a sheet-like structure and consists predominantly of two networks: collagen type IV and laminin, but also contains nidogens and PGs. This type of ECM is located underneath cells, facilitating endothelial and epithelial cell attachment via integrins, and regulating cell organization and differentiation (28). The IM or interstitial space, on the other hand, is located underneath

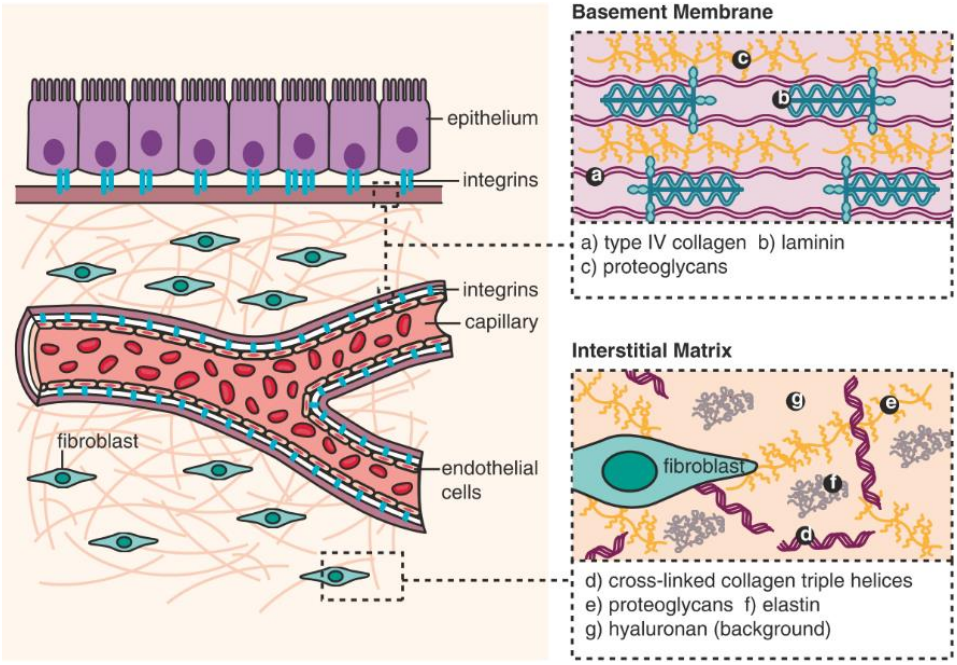

Figure 4 – *Representation of the ECM structure. The ECM is subdivided into basement membrane (BM) and interstitial matrix (IM). Adapted from (34).*

the BM and is mainly composed of networks of fibrous proteins, such as fibrillar collagens, elastin, fibronectin (**Figure 4 –** Representation of the ECM structure. The ECM is subdivided into basement membrane (BM) and interstitial matrix (IM). Adapted from (34).). The ECM, namely the IM, also serves as a reservoir and the place for the exchange of cell secretions, growth factors, ions, nutrients, metabolites and signals (29).

Fibroblasts and ECM agents

The ECM, and more specifically the IM compartment, is also the home of (myo)fibroblasts which are the major producers of ECM (28). These cells also secrete protein-degrading enzymes, the metalloproteinases (MMPs), and their inhibitors which in turn regulate ECM turnover. Fibroblasts are typically spindle-shaped cells that can differentiate into myofibroblasts, which specialize in ECM production. Myofibroblasts deposit collagen type I, III and IV as well as laminin and fibronectin which is especially important in tissue injury events, where the fibroblasts migrate to the injury site, differentiate and close the wound (30).

Post-translational modifications of the ECM also change the structure and function of the ECM. These modifications can be protein crosslinking, transglutamination, oxidation, glycation and glycosylation, among others (27). One of the most important agents of these modifications are the extracellular enzymes from the lysyl oxidase (LOX) and transglutaminase family. These enzymes are the main components responsible for the crosslinking of elastin and collagen, a crucial step in their biosynthesis (31).

The Pulmonary ECM

In the lungs, the ECM plays a particularly paramount role. The pulmonary ECM determines not only the tissue architecture but enables elastic recoil during breathing and provides mechanical stability (32). In the lung, the BM

covers the basal side of epithelia and endothelia while the IM maintains the three-dimensional (3D) structure and biomechanical features of the lungs (Figure 5).

Collagens make up roughly 30% of the total protein mass in the human body and are the most abundant type of ECM protein. Collagen type I is the most abundant of collagens since it constitutes 90% of all the collagen in the body. In the lungs, there are over 20 types of collagens that can be fibrillar (types I, II, III, V and IX) or non-fibrillar (IV) (27,33,34). The most abundant fibrillar collagens in the lung are collagens type I and III. These elements have great tensile strength, but low elasticity, so they mostly play a structural role in the architecture of bronchi, alveoli, and blood vessels. Elastic fibres, on the other hand, have low tensile strength but high elasticity, which enables the lung to elastically recoil during breathing. For this reason, the IM of alveoli is mostly composed of intertwined fibre networks composed of collagen type I and III and elastic fibres. These elastic fibres are made up of crosslinked **elastin** in its core and microfibrils made up of glycoproteins in its periphery. After fibril formation, the LOX enzyme crosslinks elastin and collagen, an essential process that provides the necessary tensile strength of the lungs. This enzyme is associated with the pathological processes in several pulmonary diseases, like idiopathic pulmonary fibrosis (IPF) and lung cancer (31,35,36).

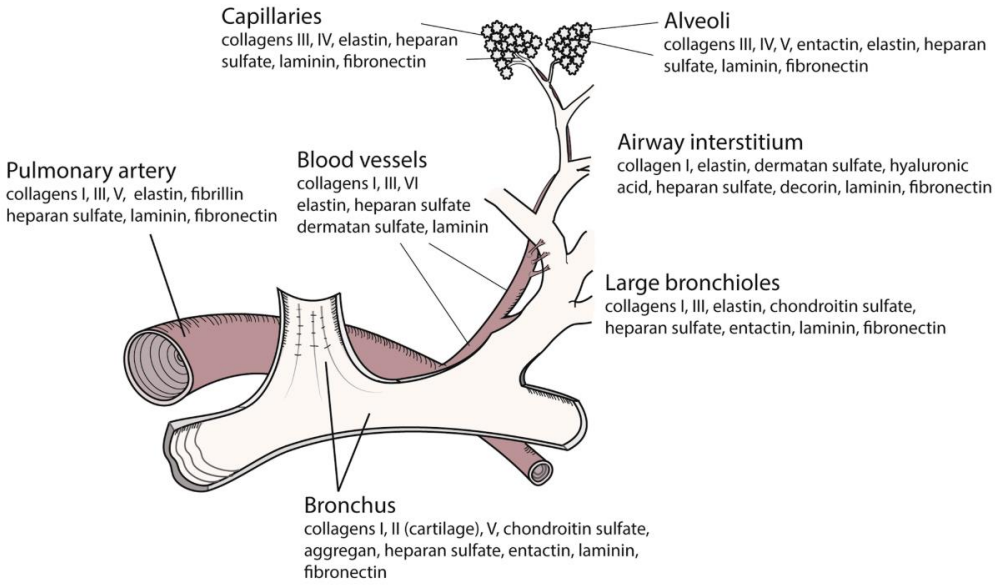

Figure 5 - *Local ECM composition in a human lung. Adapted from (33).*

Even though laminin and fibronectin do not contribute significantly to the lung's mechanical features, these proteins still play important roles in cell survival and homeostasis. **Laminin**, for one, is one of the most important components of the BM and it plays a major role in cell attachment since it has several integrin binding sites (33). It also plays an important role in cell proliferation since laminin chains induce apoptosis (37). In the lungs, as in other tissues, laminin has multiple binding sites to other ECM proteins (mainly collagen IV) that help stabilize the lung's architecture. **Fibronectin** is a dimeric fibrillar glycoprotein in the IM and like laminin, it plays an important role cell and ECM attachment. It is composed of two large subunits and each one has specific binding sites to ECM proteins like collagen and cell surface receptors. Fibronectin also regulates cell migration and differentiation to the binding of cells to specific migration or differentiation inducing proteins. In the lungs, fibronectin functions as a "magnet" for certain cells, like alveolar type II cells (38). These cells preferentially adhere to fibronectin instead of other ECM proteins, like laminin and collagens, so it is suggested that they migrate in the direction of fibronectin for better attachment (33).

Lung tumor microenvironment

Tumors are much more than just a conglomerate of cancer cells. They are composed of other cells like fibroblasts and immune cells that proliferate, migrate and support the tumor as well as the extracellular matrix and blood vessels. This non-cancerous component of the tumor is typically called the tumor microenvironment (TME) and it has a major impact on tumor progression, proliferation and invasion (Figure 6). In lung cancer, the TME not only influences tumor progression but determines the tumor's response to therapy and so the TME has become a topic of interest when developing new lung cancer therapeutics (22).

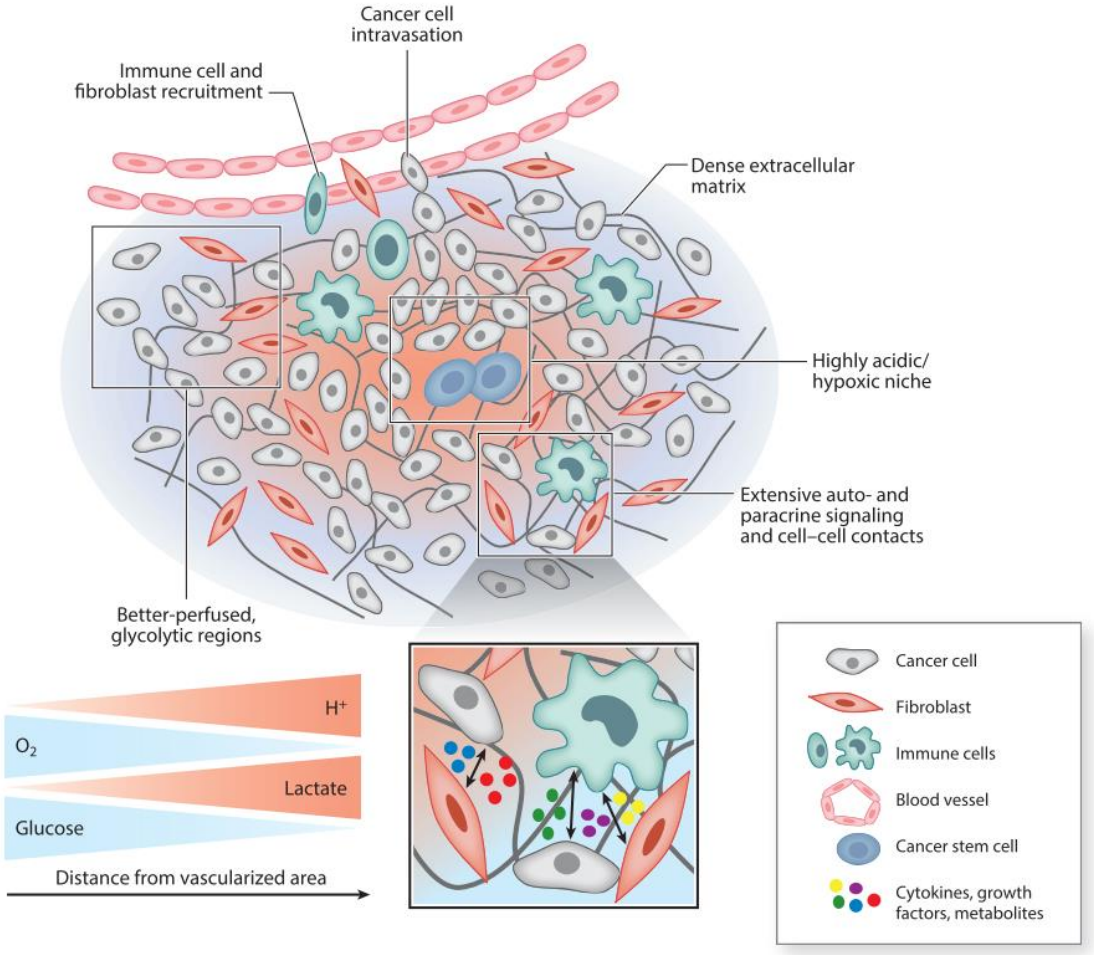

Figure 6 - *Representation of the tumor microenvironment (TME) of a solid tumor. Cancer cells and stromal cell types coexist in the TME where they interact and influence each other. Adapted from (39)*

Endothelial cells and angiogenesis

During the initial stages of tumorigenesis, tumors use diffusion to obtain oxygen and nutrients from the host. However, the build-up of metabolites, waste and lack of oxygen eventually leads to the TME becoming hypoxic and toxic. At that point, tumors will strive to establish their own blood supply by producing and secreting pro-angiogenic factors. Pro-angiogenic factors are a well-known component of the TME which are promoted by oncogenes, hypoxia and mechanical and oxidative stress (39). The most important molecule in tumor angiogenesis is vascular endothelial growth factor (VEGF), which is a growth factor derived from platelets that binds to the transmembrane receptor receptor tyrosine kinase inhibitor in endothelial

cells. Other important angiogenic factores include platelet-derived growth factor (PDGF) and fibroblast growth factor (FGF). VEGF can be produced by many of the components of the TME like endothelial cells and fibroblasts, mas its mostly produced by cancer cells. Briefly, VEGF will provoke endothelial cell migration and induce them to form new blood vessels by promoting the differentiation of endothelial precursor cells, endothelial cell proliferation and angiogenic remodelling. Endothelial cells form a thin layer called the vascular endothelium that separates the bloodstream from tissues, while transporting and delivering nutrients, immune cells and sprouting to form new blood vessels. Often, tumor vasculature will be immature and lack the structural integrity that healthy blood vessels have. This feature can be beneficial for the metastatic spread, since intravasation (i.e., when tumor cells escape the primary tumor site and enter the vasculature) will be facilitated (20,40).

Cancer associated fibroblasts (CAFs)

Under healthy conditions, fibroblasts are spindle-shaped cells that respond to tissue injury by reversibly transforming (i.e. activation) into myofibroblasts. Myofibroblasts have added characteristics that can facilitate wound healing, such as contractile properties, higher proliferation and increased ECM deposition capabilities. After tissue repair, myofibroblasts can either revert to fibroblasts or undergo apoptosis. Cancer associated fibroblasts (CAFs), or tumor-associated fibroblasts (TAFs) share a similar phenotype to myofibroblasts: they express fibroblast activation protein, produce copious amounts of fibronectin and also express alpha smooth muscle actin. CAFs however, never reverse their phenotype, hence the term given to tumors as the ‘wounds that never heal’. Most CAFs originate from tissue-resident fibroblasts after signalling via tumor-derived TGF-β1, but they can also be products of epithelial cells after EMT (20,40,41). CAFs account for 80% of the fibroblasts residing in the TME and is often synonymous with the presence of desmoplasia. A tumor rich in CAFs is

usually synonymous with a poorer diagnosis and disease reoccurrence in some types of cancers, like colorectal cancer.

CAFs have many functions within the tumor microenvironment. They produce the majority of the tumor ECM, namely collagens and fibronectin, as well as other extracellular components, like cytokines and growth factors. Specifically, they secrete TGF-β which in turn promotes EMT and neoangiogenesis in the tumor. However, they also play a major role in degradation and remodelling of the ECM surrounding the primary tumor which allows for tumor cell invasion of nearby tissues and distant sites. It is important to note that since fibroblasts are very heterogeneous from tissue to tissue, the same will happen with CAFs from tumor to tumor, leading to equally different roles depending on the type of cancer.

Cancer extracellular matrix

In tumors, the exacerbated deposition of ECM, a phenomenon known as desmoplasia, has been greatly linked to a poorer prognosis in clinical settings (42,43). Lung cancer, specifically adenocarcinoma and small cell lung cancer, exhibit high levels of desmoplasia (44). Collagens, specifically collagen type I, are often amongst the overexpressed proteins in the lung TME, but this increase in ECM deposition can be made up of many proteins, like elastin, hyaluronic acid, tenascin C, fibronectin, versican and laminin (45–47). In the TME, the ECM is present in an unregulated and disorganized matter, and it has been widely reported that certain ECM proteins influence tumorigenic proliferation, invasion and overall development. High levels of laminins are correlated with poorer prognosis in lung cancer patients and protect against tumor cell apoptosis, enhanced EMT and overall invasiveness. The overexpression of different types of collagens are seen in many lung tumors and create a permissive lung environment, increase tumor stiffness and promote tumor progression. Fibronectin was found to have inflammatory effects in lung cancer cells in vitro (48), as well as being correlated with resistance to chemotherapy in lung cancer patients (49).

However, not all ECM proteins in the lung cancer TME are tumor promoting: decorin, for instance, is a tumor suppressor for NSCLC and inhibits tumor growth, EMT and consequently metastases formation (50,51).

In addition to the biochemical composition of the tumor ECM, the structural rearrangements of the tumour microenvironment carried out by the CAFs also influence cancer cell behaviour, as seen in breast cancer matrices (52) where the tumor ECM was remodelled to orient collagen fibres perpendicularly to the tumor boundary, thus facilitating breast cancer cell invasion of the adjacent tissues (52–54). Once again, patients where this ECM realignment has been reported correlated with poorer outcomes and reduced therapeutic success (54). On the other hand, the degradation of the ECM via metalloproteinases also has a structural purpose since it allows for migration of vessels through the tumor as well as the invasion of surrounding tissues. Just as it does for healthy tissue, the tumor ECM serves as a reservoir for cytokines and pro-angiogenic growth factors, like VEGF, FGF, PDGF, TGF-β.

Lung cancer therapies targeting the ECM

Nowadays, the microenvironment, where cells grow and pathologies progress, is considered to be just as important as the cellular components that are involved in the development of a certain disease. Within that microenvironment lies the ECM, which has shown to be significantly modified in many conditions, such as inflammatory and autoimmune conditions but also in malignancy. Thus, interest in targeting the diseased ECM rather than the cells has been rapidly increasing in the last few years. The ECM can also serve as a reservoir and play a part in regulating drug delivery, features that make it a strategic target for cancer pharmaceuticals. However, to date the therapeutic options that target specifically the lung cancer ECM are scarce. Additionally, it is also important to study the effect that medications have on the ECM, which is so far an underexplored area.

For instance, corticosteroids are a standard treatment option for inflammatory lung diseases. However, this medication has been shown to significantly alter the ECM in asthma and COPD, namely causing increased ECM deposition of PGs and collagen type III in the lungs (30,55,56). Currently, only two ECM-targeting medications have been approved for lung pathologies: **pirfenidone** (PFD) and **nintedanib** (NTD). Both these medications are generally referred to as “anti-fibrotic” medications and have been mostly used for the treatment of IPF by slowing down the rate of decline in lung function but have also been used for the treatment of NSCLC and other malignancies, like ovarian cancer (57). However, their exact mechanism of action in the lung is not fully understood.

Pirfenidone

PFD is an oral medication that was originally developed as an anti-inflammatory drug since, after its administration, there was an accumulation of immune cells and a decrease in production of cytokines. It is a small hydrophobic molecule and, for that reason, does not require a receptor to enter through the cell membrane and is quickly absorbed by the gastrointestinal tract. PFD has been shown to decrease the production of fibrogenic growth factors like TGF-β1 and modulate the expression of MMPs, and consequently reduce fibroblast proliferation, myofibroblast differentiation, as well as fibronectin and collagen deposition (58).

In recent cancer studies, PFD was used in tandem with photodynamic therapy (PDT) which is a therapeutic procedure with tumor suppressive features that is hindered by the hypoxic environment within a tumor (58,59). In mice models, PFD was successfully administered in an effort to reduce the fibrosis inside the tumor, thus leading to decreased intratumoral solid stress and decompression of blood vessels, also decreasing hypoxia in the tumor.

Nintedanib

NTD (BIBF1120), on the other hand, was originally developed as an anti-angiogenic drug for oncological applications. It is a receptor tyrosine kinase inhibitor that mainly targets the vascular endothelial growth factor (VEGF), the platelet derived growth factor (PDGF), the fibroblast growth factor (FGF) and TGF-β receptors. This multi-receptor inhibition has shown to decrease fibroblast proliferation and to inhibit (myo)fibroblast differentiation, leading to significant reductions in total collagen content and overall lung fibrosis. In mice models, NTD was also shown to have anti-inflammatory effects by reducing lymphocyte, neutrophil and inflammatory cytokine presence in bronchoalveolar lavage fluid (57).

Although it has mainly been used to treat IPF, NTD has also been approved by the European Union as a treatment for lung cancer, namely NSCLC, in combination with docetaxel, a cytotoxic drug. In fact, NTD has shown anti-tumor effects in many cancer types, like ovarian, human renal cell carcinoma, colorectal and prostate carcinoma (57,60).

However, there are other ECM-based therapeutic strategies worthy of exploration for lung cancer applications. One of the most promising therapeutic targets among them is matrix crosslinking, since increased ECM stiffness has been linked to an increase in covalent crosslinking (61). For this reason, the inhibition of LOX2 enzyme has been explored as a therapeutic approach for IPF, since LOX was shown to be increased in the lungs of patients afflicted by this disorder (36,62). Duch et. al has also recently revealed the tissue inhibitor of metalloproteinase-1 (TIMP-1), an important regulator of extracellular matrix turnover, as a novel therapeutic target in lung cancer. In this study, researchers used mice models to show that the reduction of TIMP-1 led to less aggressive tumors. However, the exact effects of the reduction of TIMP-1 on ECM composition and stiffness are still to be elucidated (63).

The immune microenvironment

The immune component within the TME is one of the most important in tumor dynamics since immune cells can have either tumor-supressive or tumor-promoting functions. Chronic inflammation of the tissues, for example, is a well-known promoter for tumor invasion and malignancy progression in a number of different cancers.

Based on immune activity in the TME, tumors can be classified according to their level of immune infiltration into one of three categories of immunophenotypes: immune-inflamed (i.e. “hot tumors”), immune-excluded and immune-desert phenotypes (i.e. “cold tumors”) (Figure 7). Hot tumors will have a high level of T cell infiltration, expression of PD-L1 and overall immune activity, making them more responsive to certain immune-focused medications, such as nivolumab and pembrolizumab. Immune-excluded and immune-desert tumors are both categorized as “cold tumors”, where in the former there are T cells present, but they cannot properly infiltrate within tumor boundaries, while in the latter, T cells and other immune tumor-suppressing agents are absent from the TME and its periphery entirely (64,65). For this reason, “cold tumors” rarely respond to immune checkpoint inhibitors when compared to their “hot” counterparts. For this reason,

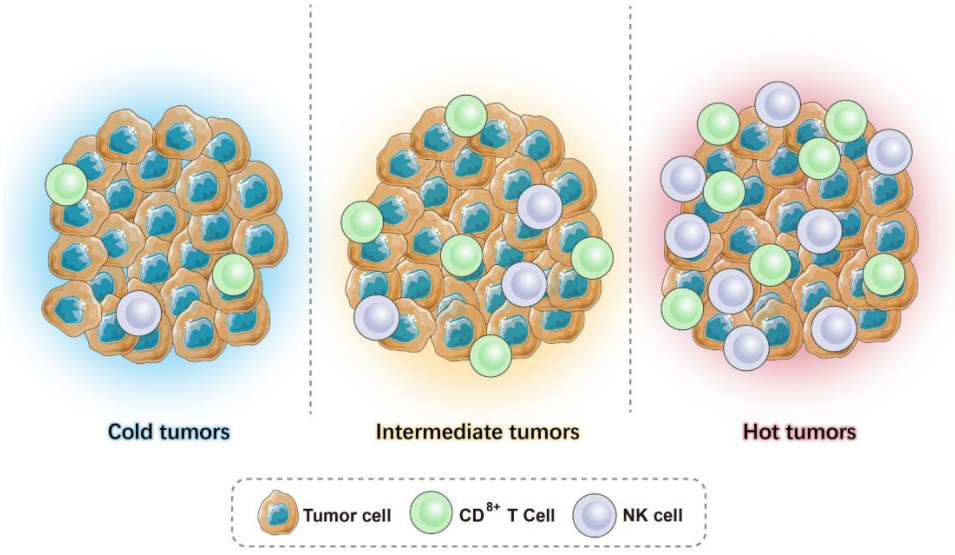

Figure 7 - *Representation of hot tumors, cold tumors, and intermediate tumors regarding tumor immune activity. Adapted from (65).*

improving T cell infiltration in the TME has been a growing research topic in recent years in order to convert previously cold tumors into inflamed tumors.

Tissue Decellularization

To properly study the ECM's properties, it is necessary to isolate it from the surrounding cells in a process called decellularization (Figure 8**Erro! A origem da referência não foi encontrada.**). For this process to be successful it requires the elimination of all cells and its components while preserving as much of the ECM as possible. However, effective decellularizing agents are often too aggressive on the ECM components, so it is important to find a balance between effective decellularization and matrix preservation. Most commonly, decellularization is performed on tissues or tissue sections, but can also be used *in vitro* to isolate the newly produced ECM from the surrounding fibroblasts, for instance. For these reasons, decellularization protocols are adapted to each sample type due to their inherent differences in ECM composition and architecture.

Decellularized tissues specifically have a wide range of applications. Clinically, decellularized tissues can serve an important role in tissue and organ failure. Currently, the deficit between patients in need of organ donation and organ donors is increasing. Tissue decellularization makes organs unspecific since cells and their DNA are removed, while maintaining the tissue's architecture, composition and mechanics. This ECM scaffold could then be repopulated with the patient's own cells to produce compatible tissues (66). Commercially, a number of tissues from humans, pigs and cows have been decellularized to create scaffolds as clinical solutions for tissue regeneration and repair, such as Pelvicol, AlloDerm, MatriStem and Dura-Guard® (67). Nonetheless, decellularized ECM is also crucial in basic research applications. In fact, it can be used to create ECM hydrogels for cell culture and provide a more physiological environment than synthetic hydrogels (68). The study of the ECM in itself is also of great scientific interest. By understanding the changes in ECM

composition, structure and stiffness that accompany disease progression, we can better understand the conditions cells are exposed to and their consequent behaviour. This study is especially useful in diseases characterized by aberrant ECM deposition, like IPF (69). With these applications in mind, it is unsurprising the recent growing interest in decellularization and decellularized tissues (70).

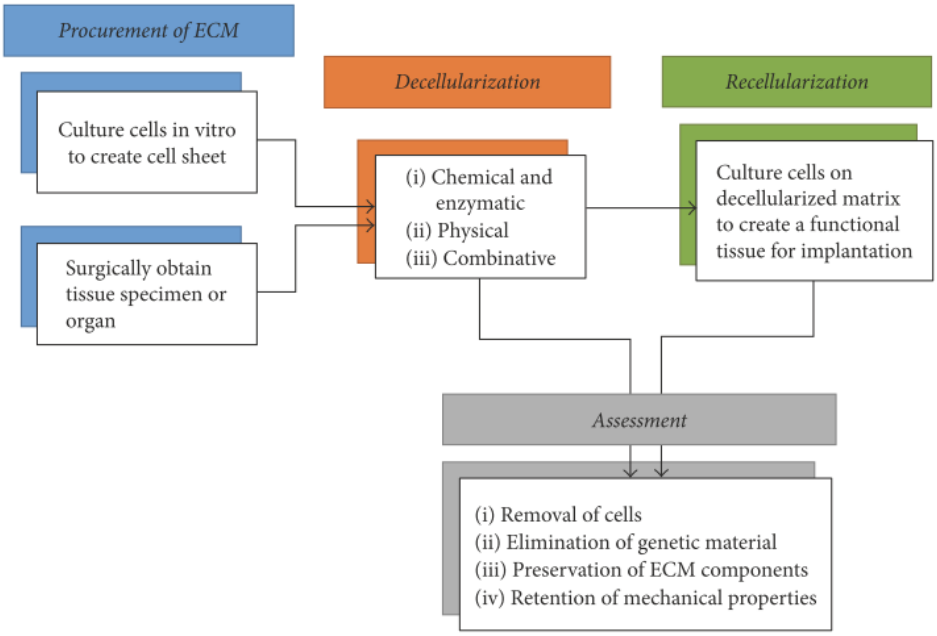

Figure 8 - *Use of acellular tissues for tissue engineering, from sample procurement to recellularization. Adapted from (74).*

Decellularization methods

A decellularization protocol can look different for different applications. In some applications, like full tissue repopulation, the whole organ must be decellularized, while for others, like the creation of ECM hydrogels, it is only necessary to decellularize a large tissue block since the ECM will be later lyophilized (71). For this reason, there are several types of decellularization methods, but we will focus on the two most common: perfusion and immersion/agitation.

Decellularization by perfusion

To decellularize complete organs, it is common to employ the perfusion decellularization technique. In this technique, the decellularizing agents flow through the tissue's vasculature at physiological pressures to reach the entire organ (72,73). In most organs, the main artery is cannulated, while in the lung, the airways are also used to perfuse reagents. Perfusion is usually stopped when the organ loses its original colour and turns white and/or transparent (Figure 9).

One downside of this technique is that applying and controlling the appropriate fluid pressure is not an easy feat and applying the wrong pressure could damage the entire organ. Additionally, this technique requires easy access to the organ's blood vessel system, which will not be feasible for small animals, small tissues, or certain organs, like skin, tendons and cartilage.

Figure 9 – *(Mouse) Lung decellularization after perfusion of decellularization agents through the trachea and vasculature. Adapted from (72), a work developed in our Unit of Biophysics and Bioengineering*

Decellularization by immersion

When access to the vasculature is difficult or non-existent, the immersion technique represents a viable alternative. As the name suggests, the

tissue or organ is submerged into the decellularizing agents which is often coupled with orbital agitation, which facilitates cellular removal. The decellularizing solution passes through the tissue by diffusion. This technique is also useful when decellularizing thick tissue sections, where the tissue is frozen, sectioned and those sections are submerged in the decellularizing solution.

When compared to perfusion, this method has the limitation of needing increasing decellularization periods depending on tissue mass. Additionally, excessive agitation can disrupt the ECM and would only be suited for thicker tissue sections, since thin sections are too fragile to be easily manipulated into and out of a decellularizing solution.

Decellularizing agents

The reagents and methods that cause cell disruption or detachment in a decellularization protocol are called decellularizing agents. These can be physical, chemical or enzymatic (29,70,74). Thus far, there is no consensus on the best protocols for each type of sample, so a protocol must be optimized depending on the tissue origin, ECM and cell density and morphology. However, the most common approach is not to use one of these agents but a combination of several.

Physical decellularizing agents

One of the most common physical agents, and often the first step in any decellularization procedure, is **freezing or freeze-thawing cycles**. By freezing and thawing the tissue, ice crystals are formed inside the cell, disrupting the cell membrane and potentially causing cell lysis. The previously mentioned **orbital agitation and sonication** also constitute physical decellularizing agents, since they can assist other agents in cell lysis and removal of cell remnants. **High hydrostatic pressure** (greater than 600MPa) applied to the tissue is also sufficient to lyse the cells.

However, any physical decellularization procedure requires a careful wash of the tissue sample to remove cellular debris and usually is not sufficient in removing remnant DNA alone.

Chemical decellularizing agents

Among the chemical decellularizing agents, there is **hypertonic** and **hypotonic salt solutions** like sodium chloride or ultra-pure water (miliQ), respectively. These agents use osmotic pressure to kill cells and explode the cell membrane, which is usually gentle on the ECM but not enough to completely remove cellular material. Another chemical strategy is the tissue incubation in *acidic or basic solutions*, like peracetic acid or ammonia hydroxide. These solutions dissolve the cell membrane and disrupt nucleic acid, but have been shown to be very aggressive on the ECM components (i.e. collagen and glycosaminoglycans) and significantly increase the stiffness of the matrix (70,74).

Surfactants (or detergents) are the most common decellularizing agents and work by solubilizing the phospholipid cell membrane leading to cell disruption. Surfactants can be ionic, non-ionic or zwitterionic, according to their charge. Ionic surfactants have a polar group and for that reason have a stronger effect than non-charged surfactants, disrupting non-covalent bonds between proteins. For that same reason, they are considered to be harsher on the ECM and more difficult to remove from the sample. The most common examples of ionic surfactants are **sodium dodecyl sulphate** (SDS) and **sodium deoxycholate** (SD), which are both anionic, meaning they are negatively charged. Although efficient in removing cellular material, SDS is extremely cytotoxic and alters the ECM architecture, while SD causes agglutination of DNA which then remains on the sample. Non-ionic surfactants have no polar groups in their structure, so they are considered mild surfactants and more easily removed. The most used is **Triton X-100**, which is commonly used to target lipid-lipid and lipid-protein interactions as well as to remove SDS and SD from the ECM.

However, Triton X-100 usually does not remove enough of the cellular material and is commonly paired with stronger decellularizing agents. Lastly, zwitterionic surfactants such as 3-[(3-cholamidopropyl)dimethylammonio]-2-hydroxy-1-propanesulfonate (**CHAPS**), have both negative and positive groups in their structure but have an overall neutral charge. For this reason, they are considered an intermediate between ionic and non-ionic surfactants, since they are efficient in breaking down protein-protein interactions but are less harsh on the matrix (70,74–76).

Enzymatic decellularizing agents

Enzymatic decellularizing agents are usually used as a supplement to other strategies as a final step to remove cell debris. Among these agents, trypsin is commonly used to detach the cells from the matrix in combination with EDTA, that breaks cell-matrix bonds. Pepsin has also been used for its ability to target peptide-peptide interactions, like trypsin. However, both trypsin and pepsin can lead to extensive ECM damage if left for too long.

After the dissolution of the cell membrane, the nuclear material tends to remain attached to the ECM. To solve this issue, it is typical to employ enzymes like deoxyribonuclease (DNAse), ribonuclease (RNAse) or benzonase to eliminate the leftover nuclear material (70,74).

Decellularization quantification

Since it has not been possible to establish a standard decellularization protocol for tissues and samples, there are subsequently no common criteria to determine the efficiency, success, and quality of any given decellularization procedure. In this section, we detail these criteria and the methods used to determine them.

Cellular removal assessment

The most common way to assess the cellular removal efficiency of a given decellularization method is by assessing the nuclei and/or DNA left in the sample after a decellularization protocol. This assessment can be done qualitatively or quantitatively. For qualitative assessments, cell nuclei are stained with either a fluorescent dye (4',6-Diamidino-2-Phenylindole Dihydrochloride (DAPI) or Hoechst 33342) or with a histological stain such as Hematoxylin and Eosin (H&E), and the lack of visible nuclei in the stained samples classifies the sample as successfully decellularized (77–80). Another example of a qualitative decellularization assessment is by the visual appearance of the organ after decellularization, since tissues will often lose their natural pink tone and become white or transparent when cells are removed (81,82). However, the most common approach is to quantify the DNA present in the tissue with absorbance-based DNA quantification (83–85). This step is typically performed by using commercially available DNA quantification kits which work by digestion of the decellularized tissue, purification of the DNA, and lastly the use of a spectrophotometer to quantify the amount of DNA per milligram of dry tissue. In 2011, Peter Crapo set a gold standard for what was to be considered a decellularized sample, where tissues should not have more than 50 ng of DNA per mg of tissue (86). As a result, this gold standard has been widely accepted in the decellularization community. Peter Crapo also suggested that DNA fragment length should be below 200 bp, as analysed by gel electrophoresis, but this criterion has not been largely adopted.

ECM preservation assessment

In addition to the efficiency of the cellular and nuclear removal from the tissue, other criteria have been described to assess the resulting ECM scaffold. One of the most important is the preservation of ECM components. This is usually performed by immunohistochemistry and immunofluorescence of ECM proteins such as collagen I, laminin,

fibronectin, elastin, GAGs, among others (depending on the research application). Other techniques include mass spectrometry, western blot, and quantitative colorimetric assays, like Fastin™ Elastin Assay. Due to the structural and functional differences between the IM and BM compartments of ECM, it is important to assess the main components from both since the decellularizing agents will have different effects on different components, a fact that is often overlooked. It is important to note though, that many of these techniques should be corrected for the change in weight of the sample, since the removal of the cells will cause a significant decrease in the sample's total mass. For instance, if the amount of elastin per milligram of dry weight is the same before and after decellularization, this likely means that there was a significant reduction in total protein content as a result of the decellularization procedure.

3D architecture and structure preservation

In some research applications, like tissue transplantation, it is essential that the tissue not only maintains its composition, but its 3D structure in order to foster and maintain the adequate cellular phenotypes. Perfusion decellularization, for example, can disrupt the organs' structure and/or vasculature if performed at above normal pressure. To assess the micro-architecture of the tissues, scanning electron microscopy (SEM) is a valuable tool that can show any damage that has been done to the ECM. The vasculature's integrity, on the other hand, can be assessed by perfusing dyes or angiography.

Biomechanics assessment

Depending on the biomedical application, it might also be important to assess the preservation of biomechanical properties of the decellularized tissue. This is especially the case for decellularized tissues like tendon or cartilage that are often subjected to mechanical stress tests to assess its macroscale mechanic properties. Other

methods to measure macroscale mechanics include uni- and biaxial mechanical testing. Atomic force microscopy (AFM) is a technique that is commonly used to measure the microscale mechanics of tissue sections before and after decellularization. However, as mentioned previously, by removing the complete cellular component of the tissue, we are significantly decreasing the tissue density which will naturally affect the overall tissue's mechanical properties, even if the ECM's mechanics remain intact. For that reason, it is not expected in all samples that they maintain the exact same viscoelastic behaviour once cells are removed, but rather that the mechanical features are within the same order magnitude and are not drastically different. In fact, it is common to see a slight decrease in stiffness in many mechanical measurements of native and decellularized tissues.

Biocompatibility assessment

Many decellularized tissues are meant for later cell repopulation and thus are required to be biocompatible and conducive to cell culture applications. Decellularizing agents, like SDS, are cytotoxic and should be thoroughly removed from the ECM scaffold before cell seeding. In some instances, it is necessary to quantify remnant surfactants using staining kits and spectrophotometry. However, more often than not, cells are seeded onto the ECM scaffolds and their survival rate and/proliferation are quantified after 24, 48 and 72h using viability/cytotoxicity staining kits as a measure for biocompatibility (87–89).

Limitations of current decellularization techniques

Decellularization techniques have greatly evolved in recent years, however, the available protocols still have significant limitations. Most of

the currently used decellularization methods require prolonged timeframes, taking anywhere from 6-7 hours (90) to several days (73,91). Many times, this is a consequence of the complexity of these procedures which in turn makes them inaccessible to many research labs and applications. Additionally, current procedures are suited for either complete organs, tissue blocks or thick tissue sections. However, these protocols would not suit many experimental conditions, like clinical biopsies. In fact, these types of samples are scarce and cannot be decellularized by assessing the tissues vasculature. Furthermore, decellularizing the complete sample is often not an option since a single biopsy is needed for many histopathological analyses. However, there still isn't a developed decellularization method that allows for the simultaneous study of native and decellularized consecutive tissue slices, since available methods are not suitable for the decellularization of attached thin tissue slices (< 30µm). This method would be particularly advantageous for studies where cells are required to identify certain phenomena, like inflammation or tumors, especially in the early stages of disease progression where changes in the ECM might not be pronounced.

Independently of the method used, most current decellularization protocols do not entirely preserve the ECM composition, particularly growth factors and GAGs. For instance, significant decreases in collagen (78,92), elastin (78,93), laminins (73,92), GAGs (83,94) and proteoglycans (92,95) are frequently reported. Even though complete ECM preservation will likely never be achieved, it is important to develop gentler procedures than the ones available today, and potentially new techniques that can preserve even the soluble factors in the ECM.

Mechanobiology

The mechanical behaviour of soft biological materials has become increasingly important in recent years with the rise of mechanobiology. Mechanobiology focuses on how mechanical forces and mechanical properties influence cells and tissues. Cells can generate mechanical forces and sense both internal and external mechanical stimuli through their lifecycle. Mechanical cues from the extracellular space are crucial in many cellular processes, such as proliferation, adhesion, migration, apoptosis, phenotype and many others (96). Stem cells, for instance, are able to sense the stiffness of their microenvironment and will differentiate into different phenotypes accordingly (97). Shear stress caused by fluid flow is also linked to inflammatory response regulation in endothelial cells of the human umbilical vein (98).

These cells and tissues respond to biomechanical signals (e.g., stiffness, stress and strain) of the extracellular environment by means of mechanotransduction, which transforms mechanical stimuli into biological responses. This complex dynamic is regulated at an intracellular level by the cytoskeleton, more specifically by actin and integrin-mediated focal adhesions that sense external mechanical stimuli and trigger intracellular responses (99,100). However, many of the pathways responsible for transforming mechanical cues into biochemical cellular signals are still to be elucidated.

Since cells receive mechanical signals from cell-cell interactions and cell-ECM interactions, it is important to study the mechanical properties of each tissue component in health and disease. The mechanical properties of a biological sample refer to the sample's response when subjected to mechanical forces. There are many types of mechanical testing available to assess a material's mechanical properties, like tension, compression, and shear rheometry, but in this section we will focus on (nano)indentation.

Nanoindentation of biological tissues

Nanoindentation techniques consist of applying classical indentation principles but to the nanoscale. In the last few decades, this technique has grown in popularity due to a few important advantages (101):

(1) – Low sample preparation requirements, where the samples do not need to be adapted to a certain conformation, like in uniaxial testing.
(2) – There is no need to 'grip' the sample.
(3) – It's a non-destructive method, so the samples might be used for further testing.
(4) – Intra sample variability can be mapped and measured, while other techniques only allow for one single value for the entire sample.
(5) – It can be coupled with other techniques, like confocal microscopy.
(6) – Sample hydration is easily maintained.

In nanoindentation, a probe is lowered to make contact with the sample surface, pushed against the sample, and then retracted until it's out of contact again. During this process, two main parameters are recorded over time (t): the load (P) and the displacement (h) to produce the main output of an indentation, a load/force-displacement curve, or force curves for simplification. A typical load-displacement curve can be seen in Figure 10. These curves can be split into two periods: a loading and an unloading phase. During the loading phase, as

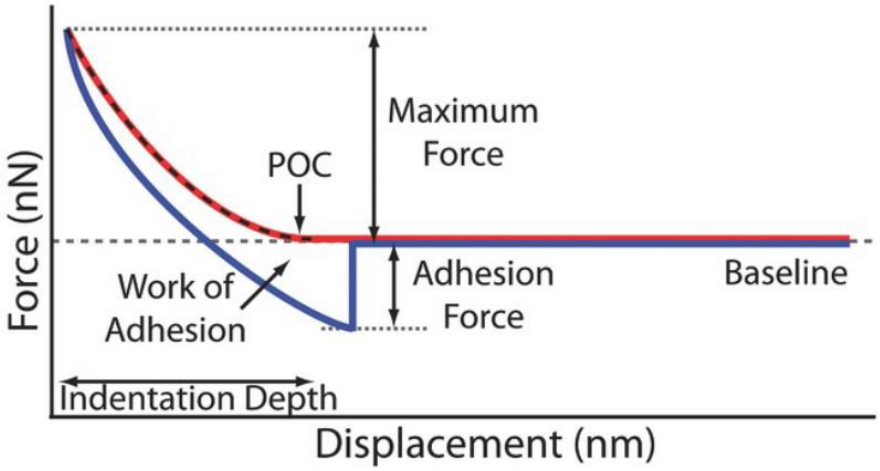

Figure 10 – *Representation of a load-indentation curve with the presence of adhesion forces. The red line represents the loading phase, and the blue line is the unloading phase. Indentation depth increases from the right to the left. Source: (101).*

the probe is lowered towards the sample, the recorded force is zero until the probe reaches the contact point (CP). From this point on, the indenter is pressed against the sample until it reaches its maximum. After that, the probe is retracted during the unloading phase and the load gradually decreases until it returns to zero.

If the loading and unloading curves are equal, the material is purely elastic, if not, a hysteresis loop is formed which indicates that energy dissipation has taken place. This energy dissipation is usually caused by at least one of three phenomena: (1) adhesion between the probe and the sample surface, which may even cause the unloading curve to reach negative load values, (2) poroelastic behaviour, caused by the fluid flow through a porous material which is relevant in hydrated materials like hydrogels and most biological tissues, and lastly, (3) time-dependent behaviour, like viscoelasticity.

Typically, two types of instruments are used to collect force-displacement curves at the nano- and microscale: dedicated nanoindentation instruments (commercial nanoindenters) and AFMs. Historically, the major differences between the two instruments were that nanoindenters were not cantilever-based, like AFM and incapable of producing topographical sample information. However, recent developments in nanoindentation systems have incorporated both features, while some AFM systems are also solely focused on mechanical characterization, making the two techniques similar in methodology and application. In this section, however, we will focus on the AFM instrument.

Atomic Force Microscopy (AFM)

The AFM is a type of microscopy which typically scans the surface of a sample with a small tip at the end of a highly sensitive cantilever (Figure 10). It can be used to scan the topography of a sample and produce corresponding topographical maps by analysing the interaction between a sharp probe and the sample's surface. It can also be used to conduct micromechanical measurements, since the tip is attached to a cantilever that acts as a Hookean spring with a known spring constant (k_c).

During standard testing of cell and tissue samples, the AFM is positioned on top of an inverted microscope to properly position the tip and probe the region of interest. AFM measures the bending of the cantilever, or deflection (d), by detecting the reflection of a laser light of the top of the cantilever onto a four-quadrant photodiode, producing a voltage (V). The tip is moved vertically towards the sample surface by a piezomotor until it touches the sample (CP), at which point the cantilever deflects, and the tip produces a force (F) on the sample resulting in an indentation (δ). The amount of cantilever deflection will strongly depend on sample and cantilever stiffness. The relationship between voltage and displacement can be calibrated by indenting an extremely stiff substrate, like glass, where indentation is equal to zero, so the vertical displacement of the piezo is equal to the deflection of the cantilever. As such, the slope of the $V - d$ curve, or deflection sensitivity s, can be described as:

$$s = \frac{\Delta V}{\Delta d}$$

Which allows the user to convert voltage to cantilever deflection. Thus, the force acting on the cantilever can be computed as $F = k_c \Delta d$.

After calibration, sample indentation can be computed as:

$$\delta = z - z_c - \Delta d$$

Where z is the piezo displacement and z_c is the relative piezo altitude of the contact point.

Hertzian Contact Model

After collecting the force curves $(P - h - t)$, the **hertzian contact model** is the most common model used to retrieve the elastic modulus of indentation curves. It uses only the loading phase of the force-displacement curves, and it models the probe and the sample as equivalent to the contact of a sphere and a semi-infinite half-space, respectively. In theory, it is only considered valid under three conditions; (1) the contact area as well as the sample deformations should be

small, (2) it can only be applied to model the behaviour of isotropic and homogeneous materials and (3) the surface of these materials should be frictionless and adhesionless. In practice, biological materials are typically not isotropic, homogeneous or adhesionless, however, this model has still become the standard for the mechanical characterization of soft materials. Assuming the tip geometry is spherical, the elastic modulus can be defined as:

$$E = \frac{3(1-\vartheta^2)P}{4R^{\frac{1}{2}}h^{\frac{3}{2}}}$$

where E represents the elastic modulus, ϑ the Poisson's ratio of the sample (typically assumed to be 0.5), R is the radius of the spherical probe and h represents the penetration depth.

Many biological materials will have a non-linear stress-strain behaviour, where the stiffness increases with increased strain. However, at small deformations, stress can be considered proportional to strain and the material can be compared to an elastic material with a constant elastic modulus. The limit between linear and non-linear behaviour is difficult to establish and could potentially be measured on a case-to-cases basis, but it is generally considered acceptable a maximum of 10% strain (102), depending also on the tip radius.

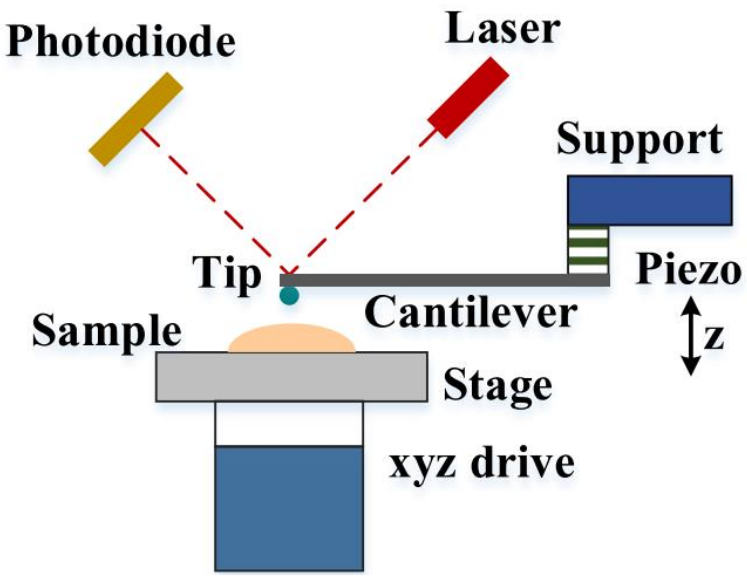

Figure 11 - *Schematic representation of the AFM device. A laser is used to read on a photodiode the deflection of a soft cantilever equipped with a tip of a known geometry. The sample is moved in the three directions (xyz) using a stage. A piezo is used to move the cantilever in contact with the surface. Adapted from (101).*

Maximum indentation considerations should also take into consideration factors like sample thickness to avoid phenomena such as substrate effect influencing the elastic modulus measurements.

Microrheology

The most common approach to study cell and tissue biomechanics is by determining their stiffness or elastic modulus. However, most biological tissues are not merely purely elastic materials and present both solid and fluid-like behaviours – they are thus viscoelastic. This means that cells and tissues' response to mechanical stimuli is dependent on the rate of said stimulus. Nanoindentation instruments are also capable of assessing the materials' viscoelastic properties by measuring the tissue's response to deformation at different rates. Specifically, the frequency-dependent elastic modulus can be determined by applying small-amplitude oscillations at a small indentation, over a range of frequencies.

A common approach to characterize tissue viscoelasticity is to compute the frequency-dependent complex shear modulus ($G^*(w)$), which is defined as the ratio in the frequency domain between the applied stress and the subsequent strain. The shear modulus can be described as a function of its real and imaginary parts:

$$G^*(f) = G'(f) + iG''(f)$$

Where $G'(f)$ accounts for the elastic energy stored, or the storage modulus, while $G''(f)$ represents the energy dissipated, or the loss modulus. The ratio between storage and loss modulus is an indicative of the level of solid- or liquid-like mechanical behaviour of the sample (103).

Cancer biomechanics

For many centuries, we have known that tumors are a lot stiffer than their surrounding environment. For that reason, palpation is still used today as an

early-stage detection tool for malignancies, such as breast cancer. However, it is unclear if this increased rigidity is due to the solely interstitial tumor pressure, altered cell mechanics or ECM stiffening. In fact, when analysing the mechanics at the micro- and nanoscale, an interesting contradiction has been reported in many cancer tissues: isolated malignant cells are almost always softer than benign cells (104–106) but tumor tissues, which are composed of cells and ECM, are typically stiffer and overall, more heterogeneous than healthy tissues (106–108).

The mechanical properties of the microenvironment have a profound impact on malignancy, and vice-versa. For example, LOX is an enzyme that is overexpressed in many cancer tissues, like gastric, colorectal and breast cancer (35,109) as a result of cancer cell death and, since it crosslinks collagen and elastin in the ECM, it leads to an increase in ECM stiffness that promotes cancer invasion and progression (61). Additionally, Ulbricht et al. indicated that the stiffness of the matrix determined the levels of autophagy in smooth muscle cells, where stiffer substrates led to higher levels of autophagy (110). This autophagic mechanism is often associated with cancer cells and influences their resistance to treatment (22,111); several studies have shown that the mechanical properties of the ECM influence EMT, more specifically, that soft substrates inhibit EMT in several cell types (112,113). This transformation causes enhanced cell motility and invasive properties and, when the original cell has undergone malignancy, these new features lead to an increased likelihood of metastasis and overall invasive behaviour, among other characteristics (16).

In the lung, the expansion of the tumor exerts compressive forces on surrounding parenchyma and the ECM, leading to a constriction of the blood and lympathic system as well as the alveoli. Lung tissue reportedly has a stiffness ranging from 0.5 to 10kPa, which is on the lower end of the stiffness scale for biological tissues (from 0.1 to 20000 kPa, approximately). For this reason, the compression caused by the growing tumor easily damages the lung parenchyma and allows for tumor invasion. In fact, Voutouri and colleagues estimated that the tumor must be at least 50% stiffer than the surrounding tissue to exert enough force to escape confinement by healthy tissue (114).

Unfortunately, biomechanical studies of the lung tumor are scarce. However, Plodinec and colleagues mapped the stiffness of breast metastases to the lungs and found the stiffness distribution of the secondary lesion closely resembles the signature of the primary site. In addition, their work linked the softening of the metastatic cancer cells with their invasive potential.

Therapeutic and diagnostic applications of cancer mechanobiology

Understanding and visualizing the mechanical and structural environment in tumorigenesis is of significant importance for clinical applications. By knowing its characteristics, mechanical measurements of the tumor can have applications in diagnostics by distinguishing healthy from malignant tissue or by determining the invasive potential of a tumour. As previously mentioned, Plodinec et al (2012) mapped the stiffness of human breast cancer biopsies using AFM. The study concluded that the mechanical properties of the tissue can be used as a distinct mechanical fingerprint of cancer-related changes, differentiating between healthy tissue and benign or invasive tumours (106). If these findings can be applied to other types of cancers at different stages, nanomechanical signatures can have a high diagnostic potential. Moreover, the mechanical properties of a tumour may also determine the best course of treatment for a particular rigidity (113). For instance, photodynamic therapy (PDT) is a promising treatment option for tumour suppression where ECM remodelling substances can be used to improve its efficacy. By decreasing the amount of collagen-I and hyaluronic acid there is a decrease in intratumoral solid stress, and the tumour vessels are decompressed, allowing for a better oxygenation of the tumorous cells (115). Nonetheless, understanding the mechanobiology of tumorigenesis is paramount in revealing its role in cancer development and metastasis.

Chapter II.

HYPOTHESES AND OBJECTIVES

Hypotheses

1. Tumor extracellular matrix will vary according to the tumor primary site.

2. Lung tumor extracellular matrix has different mechanical properties than healthy lung extracellular matrix.

3. Tumor extracellular matrix mechanical and biochemical properties are different in early and late-stage lung metastases.

4. Treatment with the anti-fibrotic drug Nintedanib will lead to a softening of the tumor extracellular matrix.

Objectives

General objective

The general objective of this thesis is to study the compositional and micromechanical changes of the tumor extracellular matrix in lung metastases.

Specific objectives

1. To develop a method to decellularize tumor slices while preserving biochemical and biophysical extracellular matrix characteristics.
2. To design a novel image-based method to better quantify the decellularization process in tissue and tumor sections.
3. To correlate mechanical properties, molecular composition and structure of extracellular matrix of normal and cancer lung tissues of different origins and throughout different stages of tumor progression.
4. To assess the changes in the lung tumor extracellular matrix in response to nintedanib treatment.

Chapter III.

MATERIALS AND METHODS AND RESULTS

Scientific Article I:

“Novel Decellularization Method for Tissue Slices”

This article was published in March 2022 to fulfil the specific objective (1): “To develop a method to decellularize tumor slices while preserving biochemical and biophysical extracellular matrix characteristics”. In this work, we focused on establishing a universal decellularization method for a variety of tissue origins, like kidney, heart, bladder and lung.

frontiers in Bioengineering and Biotechnology

ORIGINAL RESEARCH
published: 09 March 2022
doi: 10.3389/fbioe.2022.832178

Novel Decellularization Method for Tissue Slices

Maria Narciso[1,2], *Anna Ulldemolins*[1], *Constança Júnior*[1,2], *Jorge Otero*[1,2,3], *Daniel Navajas*[1,2,3], *Ramon Farré*[1,3,4], *Núria Gavara*[1,2] *and Isaac Almendros*[1,3,4]*

[1]Unitat de Biofísica i Bioenginyeria, Facultat de Medicina i Ciències de la Salut, Universitat de Barcelona, Barcelona, Spain, [2]The Institute for Bioengineering of Catalonia (IBEC), The Barcelona Institute of Science and Technology, Barcelona, Spain, [3]CIBER de Enfermedades Respiratorias, Madrid, Spain, [4]Institut d'Investigacions Biomèdiques August Pi i Sunyer, Barcelona, Spain

Decellularization procedures have been developed and optimized for the entire organ or tissue blocks, by either perfusion of decellularizing agents through the tissue's vasculature or submerging large sections in decellularizing solutions. However, some research aims require the analysis of native as well as decellularized tissue slices side by side, but an optimal protocol has not yet been established to address this need. Thus, the main goal of this work was to develop a fast and efficient decellularization method for tissue slices—with an emphasis on lung—while attached to a glass slide. To this end, different decellularizing agents were compared for their effectiveness in cellular removal while preserving the extracellular matrix. The intensity of DNA staining was taken as an indicator of remaining cells and compared to untreated sections. The presence of collagen, elastin and laminin were quantified using immunostaining and signal quantification. Scaffolds resulting from the optimized protocol were mechanically characterized using atomic force microscopy. Lung scaffolds were recellularized with mesenchymal stromal cells to assess their biocompatibility. Some decellularization agents (CHAPS, triton, and ammonia hydroxide) did not achieve sufficient cell removal. Sodium dodecyl sulfate (SDS) was effective in cell removal (1% remaining DNA signal), but its sharp reduction of elastin signal (only 6% remained) plus lower attachment ratio (32%) singled out sodium deoxycholate (SD) as the optimal treatment for this application (6.5% remaining DNA signal), due to its higher elastin retention (34%) and higher attachment ratio (60%). Laminin and collagen were fully preserved in all treatments. The SD decellularization protocol was also successful for porcine and murine (mice and rat) lungs as well as for other tissues such as the heart, kidney, and bladder. No significant mechanical differences were found before and after sample decellularization. The resulting acellular lung scaffolds were shown to be biocompatible (98% cell survival after 72 h of culture). This novel method to decellularize tissue slices opens up new methodological possibilities to better understand the role of the extracellular matrix in the context of several diseases as well as tissue engineering research and can be easily adapted for scarce samples like clinical biopsies.

Keywords: decellularization, bioscaffold recellularization, biocompatibility, extracellular matrix, tissue slices, lung

OPEN ACCESS

Edited by:
Kamal Hany Hussein, Assiut University, Egypt

Reviewed by:
Anna Guller, Macquarie University, Australia
Bruce Alan Bunnell, University of North Texas Health Science Center, United States

***Correspondence:**
Isaac Almendros
isaac.almendros@ub.edu

Specialty section:
This article was submitted to Biomaterials, a section of the journal Frontiers in Bioengineering and Biotechnology

Received: *09 December 2021*
Accepted: *09 February 2022*
Published: *09 March 2022*

Citation:
Narciso M, Ulldemolins A, Júnior C, Otero J, Navajas D, Farré R, Gavara N and Almendros I (2022) Novel Decellularization Method for Tissue Slices. Front. Bioeng. Biotechnol. 10:832178. doi: 10.3389/fbioe.2022.832178

1 INTRODUCTION

The extracellular matrix (ECM) plays an important role by regulating cell behavior through structural and biochemical stimulation. The ECM is composed of more than 300 core structural components (Burgstaller et al., 2017) that provide physical and chemical cues that regulate essential cellular mechanisms (Gattazzo et al., 2014), including proliferation, migration and differentiation. Overall, the ECM is divided into two major compartments: the interstitial ECM and the basement membrane. The interstitial ECM is in the intercellular spaces and is composed mostly of fibrous proteins and polysaccharides, most predominantly collagen type I and III, elastin, and fibronectin. The basement membrane is made up of sheets of deposition of ECM components—mainly collagen type IV and laminins—that are located under epithelial and endothelial cells (Pompili et al., 2021). These two layers make up the "core matrisome." However, the ECM has other components such as ECM-affiliated proteins and secreted factors that are typically removed during decellularization and thus less frequently characterized (Hynes and Naba 2012). The study of the ECM and its characteristics yields an important understanding of the complex interactions between cells and their microenvironment, which plays a pivotal role in various diseases including cancer and fibrosis (Rendin et al., 2019; Wishart et al., 2020; Júnior et al., 2021). Accordingly, decellularized ECM scaffolds have great potential for tissue engineering and regenerative medicine. In fact, decellularized tissues can be used for the generation of ECM hydrogels (Falcones et al., 2021), for the recellularization of whole acellular organs (Ohata and Ott 2020), as well as applications in tissue regeneration (Zhu et al., 2019). Thus, it is unsurprising the growing interest to work on physiomimetic tissue scaffolds by decellularizing different types of tissues (Mendibil et al., 2020).

To remove cells from their ECM, several strategies can be employed (Mendibil et al., 2020) by using physical, chemical, enzymatic or a combination of approaches. Physical strategies include freeze/thawing cycles, which induce crystals in the matrix disrupting the cell membrane, as well as agitation, which is commonly used in conjunction with another/s decellularizing agent/s facilitating cell lysis. Chemical strategies include detergents, such as Sodium Dodecyl Sulfate (SDS) or Sodium Deoxycholate (SD), that solubilize the cell membrane and hypertonic or hypotonic solutions, that will cause cell disruption by osmotic shock. Finally, enzymatic approaches can target the adhesion of cells to the ECM, such as the combination of trypsin with EDTA (ethylenediaminetetraacetic acid) or target the nuclear material of the cell, such as with deoxyribonuclease (DNAse). In this context, each decellularizing agent can affect differently each specific ECM components. In fact, to assess the quality of the resulting scaffold it is required to analyze the effects of the decellularizing agent on the ECM components. At times, only components of the interstitial ECM are analyzed, like collagen type I and elastin (O'Neill et al., 2013a; Balestrini et al., 2015; Alshaikh et al., 2020). However, the evaluation of the basement membrane is of paramount importance especially for tissue engineering and cell culture applications since these components heavily influence cell adhesion and differentiation (Rasmussen and Karsdal 2016). The most analyzed basement membrane components include collagen type IV and laminins (Maghsoudlou et al., 2013; Zhang et al., 2016).

The available decellularization protocols have important limitations. Most of them require prolonged periods, taking from 6–7 h (Rosmark et al., 2018) to several days (Wishart et al., 2020; Wüthrich et al., 2020). Additionally, most of the available methods fail in the preservation of some ECM components. For instance, significant decreases in elastin (Maghsoudlou et al., 2013; Alshaikh et al., 2020), collagen (Hill et al., 2015; Alshaikh et al., 2020), glycosaminoglycans (Mendoza-Novelo et al., 2011; Lü et al., 2014), laminins (Hill et al., 2015; Wüthrich et al., 2020) and proteoglycans (Hill et al., 2015; Calle et al., 2016) have been described. In addition to these limitations, the current protocols are still not particularly flexible or accessible. Most decellularization procedures are suited for

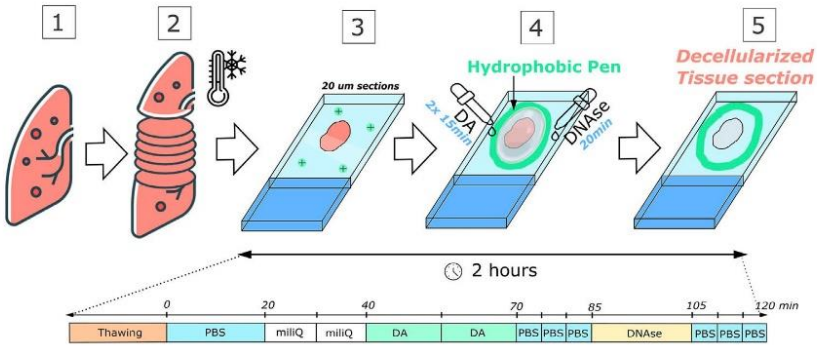

FIGURE 1 | Schematic of the novel decellularization method for a lung sample. (1) Organs are harvested and stored at −80°C and embedded in OCT; (2) then they are cryosectioned into 20 µm sections and (3) deposited onto positively charged glass slides; (4) Decellularization is performed through a series of washes and rinses, including the decellularizing agent (DA) and a Deoxyribonuclease I (DNAse) incubation. After carefully removing the reagents with PBS, a fully decellularized section is produced in 2 h (5). MilliQ is a form of ultrapurified water.

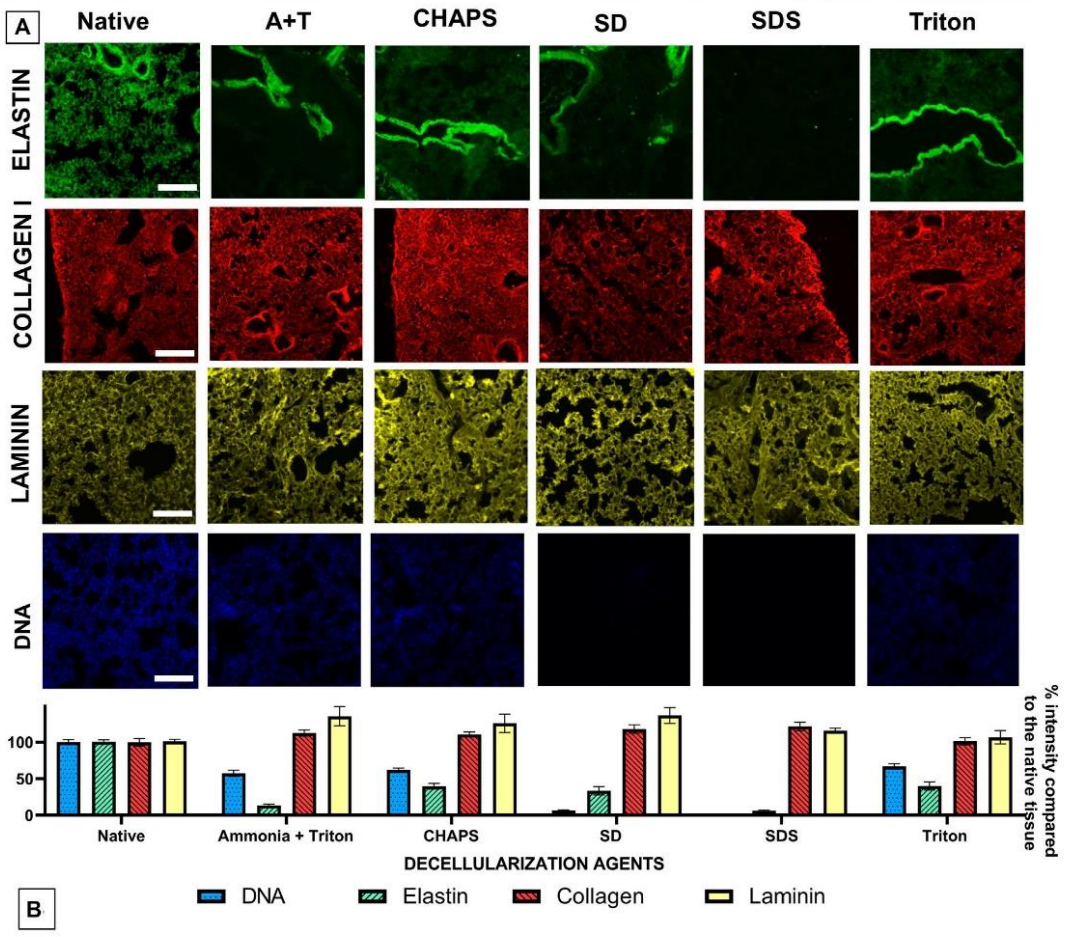

Decellularizing agent	Sample attachment, %	Native DNA signal, %
(None—native)	100±0	100±24
Ammonia + Triton	100±0	57±31
CHAPS	82±12	62±22
SD	60±23	6.5±5.8
SDS	32±22	1±0.5
Triton	100±0	67±28
Trypsin	0±0	-

Decellularizing agent	Tissue	Sample attachment, %
SD	Bladder	100±0
	Kidney	100±0
	Heart	100±0
	Lungs	60±23

FIGURE 2 | (A) Staining and signal quantification of 20 µm lung sections from mice for nuclei, elastin, type I collagen, and laminin. Lung sections had been previously subjected to five different decellularization treatments (Ammonia + Triton, CHAPS, SD, SDS, and Triton). Laminin and elastin fluorescent images were changed from the original red color to yellow and green respectively for easier image readability. Native tissue's signal was normalized to 100% Scale bar = 200 µm. **(B)** Table describing the attachment ratio of tissue slices from the glass slide for each decellularization treatment (left) and Table describing the attachment ratio of different tissues treated with SD (right). Data are mean ± SEM.

decellularizing a whole organ or thick sections of an organ (or blocks). However, this type of protocol would not be useful for many experimental conditions as is the case for small clinical biopsies. Indeed, this type of sample is scarce and cannot be decellularized by accessing the tissue's vasculature. Furthermore, the full biopsy cannot often be decellularized since it is also required for later histopathological testing. Other experimental setups might require consecutive native and acellular sections of the same individual. This is the case for studies on cancer samples where the tumor location and inner structures must be identified

prior to decellularization. For early-stage tumors especially, this is of paramount importance as the cancer cells are removed during decellularization and its location could not be pinpointed. As no current methods have explored the decellularization of glass-attached thin tissue sections (under 100 µm), a novel protocol that allows for the study of the exact location before and after decellularization is needed to fill this gap.

In this study, we set out to develop a novel decellularization method where a thin tissue section is kept attached to a glass slide allowing for "*in situ*" decellularization without removing the sample from a microscopic stage. This method is significantly faster and less wasteful than other available methods while maintaining the mechanical properties of the sample and being suited for cell culture applications. Our findings show that this method is highly versatile and applicable to tissues of different animal origins and from different organs, such as the bladder, heart, and kidney. Additionally, it provides the option to study the same tissue section before and after decellularization, which is invaluable for studies of certain pathologies and of scarce or valuable clinical samples.

2 MATERIALS AND METHODS

2.1 Organ Procurement and Sample Preparation

This work was approved by the Institutional Committee of Universitat de Barcelona and the Animal Experimentation Committee of regional authorities (Generalitat de Catalunya, OB 168/19 and 10972). The lungs were obtained from male C57BL/6J mice (10 weeks old; Charles River Laboratories, Saint Germain sur L'arbresle, France) and male Sprague-Dawley rats (body weight ~ 300 g Charles River Laboratories, Saint Germain sur L'arbresle, France). Bladders, hearts, and kidneys were harvested from the adult mice and embedded in Optimum Cutting Temperature compound, OCT (Tissue-Tek, Sakura, Torrance, CA, United States) and immediately stored at −80°C. Porcine lungs were obtained from the local butcher and a small portion was embedded in OCT. Mice lung samples were sectioned at 20 and 100 µm using a cryostat, with a working temperature of −24°C. All other samples were sectioned only at 20 µm thickness. Slices were deposited onto a positively charged glass slide (Superfrost Plus; Thermo Fischer Scientific) and air-dried for 15 min before being stored at −80°C until further use. Before decellularization, 20 µm thick sections were thawed are room temperature for 20 min and 100 µm thick sections were thawed for 40 min. It is important to thaw the sample completely for increased attachment. The freeze-thaw cycle already functions as an initial step of decellularization (Gilpin and Yang 2017).

2.2 Decellularization Protocol and Methods Comparison

Before decellularization, the area surrounding each sample was traced with a liquid repellent slide marker pen (or hydrophobic pen) to better control and reduce the volume of reagents needed (**Figure 1**). Acellular sections were produced by consecutive washes and rinses of the sliced section with different solutions while still firmly attached to the glass slide.

All decellularizing protocols studied in this work followed the same schedule. For 20 µm sections, an initial 20-min PBS wash to remove the OCT from the sample. To cause an osmotic shock and disrupt the cellular membrane, the next step was to apply two consecutive 10-min washes with ultrapure water. Subsequently, the decellularizing agent was incubated twice for 15 min intervals to dissolve the cellular membrane and detach the cells from the matrix. The following step was to remove the decellularizing agent with three 5-min washes of PBS. A 20-min incubation with DNAse I solution (0.3 mg/ml, 5 mM $MgCl_2$, 5 mM $CaCl_2$ in 1 mM Tris-HCl) was carried out to remove DNA fragments. Finally, 5-min washes (x3) of PBS were performed to remove the DNAse I solution. For 100 µm sections, DNAse I solution was incubated for 40 min at 37°C, for optimal enzymatic activity.

Six decellularizing agents (DAs) were tested and compared. The DAs and their concentrations were adapted from existing decellularization protocols, and were as follows:

Method 1: Ammonium Hydroxide 0.5% + Triton 0.1%, based on (Ng et al., 2019);
Method 2: CHAPS 0.5%, based on (Rosmark et al., 2018);
Method 3: Sodium Deoxycholate (SD) 2%, based on (Xiong et al., 2015);
Method 4: Sodium Dodecyl Sulfate (SDS) 1%, based on (Jorba et al., 2019);
Method 5: Triton X-100 1%, based on (Mendoza-Novelo et al., 2011);
Method 6: Trypsin 0.05% + EDTA 0.02%, based on (Schenke-Layland et al., 2003);

Detailed information about the existing decellularization protocols can be found in **Supplementary Table S1**.

2.3 Attachment to the Glass Slide

For this decellularization method, one key factor is the attachment of the sample to the glass slide throughout the decellularization protocol. Thus, we calculated the percentage of sample attachment (number of samples that remained attached after the treatment/total number of samples tested) × 100%. It is a visual observation as the sample is clearly detached and removed from the glass slide during decellularization. Five decellularization experiments were conducted and samples were counted before and after decellularization. For each experiment, 5, 6 sections were used per treatment.

2.4 Immunofluorescence, DNA and Histological Staining

Both cellular and acellular mice lung sections from Methods 1–5 were stained for laminin, type I collagen, elastin, and DNA to determine the effects of the decellularization protocol on the matrix proteins as well as the cellular material and DNA. These proteins were specifically chosen because they are three major components of the ECM: collagen and elastin can provide information on the interstitial ECM and laminin on the basement membrane. For native sections

where the decellularization protocol was not followed, immunofluorescent staining was performed after consecutive washes of PBS to remove the OCT. For decellularized sections, the staining protocol was performed immediately after the decellularization procedure described above. The tissue was fixed using 4% paraformaldehyde (PFA) for 10 min at room temperature (RT). Samples were then blocked using a buffer composed of 10% fetal bovine serum (FBS) and supplemented with 3% bovine serum albumin (BSA) for 1 h at RT. Primary antibodies against elastin (rabbit anti elastin, BioNova, 1:100), type I collagen (rabbit anti-collagen type I, Abcam, 1:100), and laminin (rabbit anti laminin, Thermo Fisher Scientific, Waltham, MA, 1:100) were incubated in the same formulation of the blocking buffer overnight at 4°C and constant agitation (80 rpm). Sections were then rinsed three times with the blocking buffer. The secondary antibody (goat anti-rabbit Cy3, Thermo Fischer, 1:200) was incubated at a 1:200 dilution in the blocking buffer for 2 h, at 37°C and constant agitation (80 rpm). Three 15 min rinses with PBS were performed to eliminate the unbound secondary antibodies. DNA of cellular and acellular samples was stained by incubation with Hoechst 33342 (Thermo Fisher Scientific)—for 20 min at 80 rpm in an orbital shaker followed by three 5-min PBS washes to remove excess staining with the same agitation settings. The Hoechst staining concentration was carried out following the manufacturer's instructions. Finally, samples were mounted in Fluoromount mounting media (Thermo Fisher Scientific) and stored at 4°C. For each experiment, laminin, type I collagen, and elastin staining was performed in consecutive lung sections. The color of the laminin and elastin fluorescent images was changed after image acquisition from red to yellow and green respectively, for easier figure readability. Brightness and contrast were improved for the same purpose. Both cellular and acellular mice lung sections from Methods 1–5 were stained using Picro-Sirius Red Stain Kit (ScyTek Laboratories, US) for collagen type I and III presence and Hematoxylin and Eosin (PanReac Applichem) to assess the presence of the nuclei.

2.5 Mechanical Testing by Atomic Force Microscopy

To assess mechanical changes in the tissue before and after decellularization, an Atomic Force Microscope (AFM) was used to measure the stiffness, viscosity and force adhesion of the samples. In a custom-built AFM system, the cantilever was displaced in 3D with nanometer resolution employing piezo actuators coupled to strain gauge sensors (Physik Instrumente, Germany) to measure the vertical displacement of the cantilever. The deflection of the cantilever was measured with a quadrant photodiode (S4349, Hamamatsu, Japan). The cantilevers employed had a nominal spring constant value of 0.03 N/m and a silicon oxide bead with a 4.5 µm diameter attached to its end (Novascan Technologies, IA).

The lung ECM was probed while submersed in PBS at RT. Three lung sections from different mice were measured using AFM before and after decellularization using the SD-based protocol. Before the measurements, a small region in the lung parenchyma was selected and marked with a pen. With the visual assistance of the optical microscope, the tip was positioned macroscopically over the region of interest of the lung sample. Up to 20 randomly selected locations were indented within the delineated region before decellularization and the same was performed after decellularization within the same region. Only alveolar structures were considered by excluding airways, blood vessels and the pleural region.

The deflection and displacement of the cantilever were recorded as the cantilever descended and contacted the sample surface at constant speed up to a maximum loading force, with a ramp amplitude of 15 µm and frequency of 1 Hz. To calculate the model's parameters, each curve was fitted through a custom MATLAB code (MATLAB, The MathWorks Inc. MA, United States). The Young's modulus fitting was performed using the approaching curve and fitting the appropriate tip-sample contact model to the force-indentation curve (Jorba et al., 2017). Viscosity measurements were computed by following the model described in (Rebelo et al., 2013) and force adhesion was obtained by computing the minimum of the retracting curves. All mechanical values were obtained by computing the mean values of the five curves recorded consecutively at each point.

2.6 Cell Culture

Primary human Bone Marrow-Derived Mesenchymal Stromal Cells (hBM-MSCs) (PCS-500-012, ATCC) were cultured in Mesenchymal Stromal Cell Basal Medium (PCS-500-030, ATCC) following manufacturer's instructions at 37°C in air with 5% CO_2 and 95% relative humidity. Cells from passages 3–6 were used for experiments.

2.7 Biocompatibility Assay

After decellularization, the 20 µm-thick and 100 µm-thick scaffolds were incubated for 2 h with a peracetic acid solution (269336, Sigma-Aldrich) 0, 1% (v/v) in 4% ethanol for sterilization. Subsequently, they were washed with PBS (11593377, Gibco) and $5{\cdot}10^4$ cells/cm^2 hBM-MSCs were seeded on top of the lung scaffolds. Control cultures were seeded on conventional culture plastic flasks and maintained in parallel with the same conditions. After 24, 48, and 72 h of recellularization, samples were stained using the LIVE/DEAD Viability/Cytotoxicity kit (L-3224, Invitrogen). Calcein-AM was used to indicate live cells (green), and ethidium homodimer-1 was used to indicate dead cells (red) as previously described (Bonenfant et al., 2013; O'Neill et al., 2013b; Syed et al., 2014). After 72 h, F-Actin was stained in the 100 µm scaffolds (phalloidin, Thermo Scientific, Waltham, MA, United States) and visualized by a confocal microscope. The results were obtained by counting the number of live cells from five independent biocompatibility assays.

2.8 Imaging and Decellularization Quantification

Epifluorescent images of the tissue sections were acquired with a Leica SP5 inverted microscope equipped with a CCD camera (C9100, Hamamatsu Photonics K.K. Hamamatsu, Japan) and using a ×10 and ×20 Plan Fluor objective (Nikon). For 3D images

of the 100 µm scaffolds and cellular distribution, a Nikon D-Eclipse Ci confocal microscope was used in conjunction with a ×20 Plan Apo immersion oil objective (Nikon). For the imaging of the cytoskeleton of the cells ×20, ×60, and ×100 immersion oil objectives were used (Nikon). For the histological stains, a ×20 and a ×40 objective was used with an Olympus BX41TF upright microscope.

Decellularization quantification was performed as previously described (Narciso et al., 2021). Briefly, images belonging to a given treatment (decellularized slices) and corresponding control condition (native slices belonging to the same organ and animal) were acquired in a single imaging session. Exposure times for the phase contrast (PC) and the fluorescent channels were set based on the control (native) sections corresponding to each experiment. At least ten locations per condition were imaged except when less than ten locations were needed to cover the complete tissue area. Images were taken 1 mm apart from each other starting from the edge of a sample until covering the entirety of the sample length. The DNA signal intensity of the images from decellularized sections was compared to the DNA signal intensity of the corresponding native sections. The same method was used to quantify collagen, elastin, and laminin signals resulting from immunofluorescent staining. The signal corresponding to the ECM proteins of the untreated native sections was normalized to 100%.

2.9 Versatility of the Method for Different Species and Organs

To assess whether the SD decellularization method can be used for other types of tissues, 20 µm-thick sections of mice bladder, heart and kidney were subjected to the same decellularization protocol previously described in **Section 2.2**. Three independent decellularization experiments of each organ were performed. Additionally, three independent decellularization experiments were conducted using lung slices from pigs and rats, since these species are commonly used in animal models of respiratory diseases.

2.10 Statistical Analysis

For experiments with two groups (native and decellularized), statistical comparisons were performed by an unpaired two-tailed *t*-test. Unless mentioned, all data are mean ± SD. Differences were considered statistically significant for $p < 0.05$. Statistical analysis was performed using GraphPad Prism (GraphPad software 9.1.0, Inc. San Diego, CA, United States).

3 RESULTS

3.1 SD and SDS are the Most Effective Treatments for Cellular Removal

Even though trypsin + EDTA has been previously used in decellularization protocols, this method detached all tested samples and thus it is not suited for decellularization protocols on a glass slide. For that reason, no results on DNA staining and ECM proteins are presented here for trypsin decellularization, since no samples could be stained. All other decellularization methods resulted in scaffolds suited for further staining.

In **Figure 2**, representative UV images of Hoechst staining clearly show the removal of cell nuclei and DNA from all different methods studied. Cell nuclei are clearly present in native sections and noticeably absent (or reduced) after each decellularization treatment. To quantify the different decellularization levels resulting from different treatments, pixels corresponding to tissue were separated from background pixels, quantified, and compared to native tissue pixel intensities as previously described (Narciso et al., 2021). The DNA signal from native sections was normalized to 100% for easier comparison. All methods resulted in a significant reduction in DNA staining ($p < 0.05$) when compared to untreated native sections, as evidenced in **Figure 2**. SD and SDS treatments resulted in a marked DNA signal decrease (6.5 ± 5.8% and 1 ± 0.5% of native DNA signal, respectively) indicating that most cells and residual DNA was removed. On the other hand, CHAPS, Triton, and Ammonia/Triton mixture showed 62 ± 22%, 67 ± 28%, and 57 ± 31% of the native DNA signal, respectively, not reaching an acceptable decellularization level. A qualitative analysis of nuclei of lung sections stained with the hematoxylin and eosin (**Supplementary Figure S1**) validates the results obtained from the UV images of Hoechst33342-stained nuclei: only SDS and SD seemed to have efficiently removed cell nuclei from the sample, while the other methods did not reach sufficient cell removal rates.

3.2 All Treatments Preserved the ECM Proteins

As shown in **Figure 2**, all treatments resulted in a reduction of the elastin signal. SDS and the Ammonia and triton mixture in particular, showed a marked degradation of elastin signal where 6 ± 3% and 13 ± 8% of the native elastin signal remained, respectively. SD, CHAPS, and Triton, on the other hand, showed higher rates of elastin preservation, accounting for 34 ± 25%, 40 ± 19%, and 40 ± 24% of the pre-treatment elastin signal. This decrease is especially visible in the lung parenchyma, while blood vessels and airways seem to maintain elastin signal levels (**Figure 2**). Regarding laminin and collagen, none of the treatments used showed a decrease in laminin or collagen signal when compared to the corresponding native section. A quantitative analysis of samples stained with Picro-Sirius red (**Supplementary Figure S2**) showed a clear reduction in collagen type I and III stain in the SDS treated samples (81 ± 3%) when compared to the native samples (100% signal). Samples treated with the other decellularizing agents showed no marked differences when compared visually to the native sections: Ammonia + Triton, CHAPS, SD and Triton treatments showed 100 ± 4%, 108 ± 4%, 98 ± 3%, and 108 ± 3% when compared to the native image, respectively.

3.3 Samples Remained Attached to the Glass Slide

As observed in **Figure 2B**, treatments with higher rates of cellular removal were more likely to detach the sample from the glass

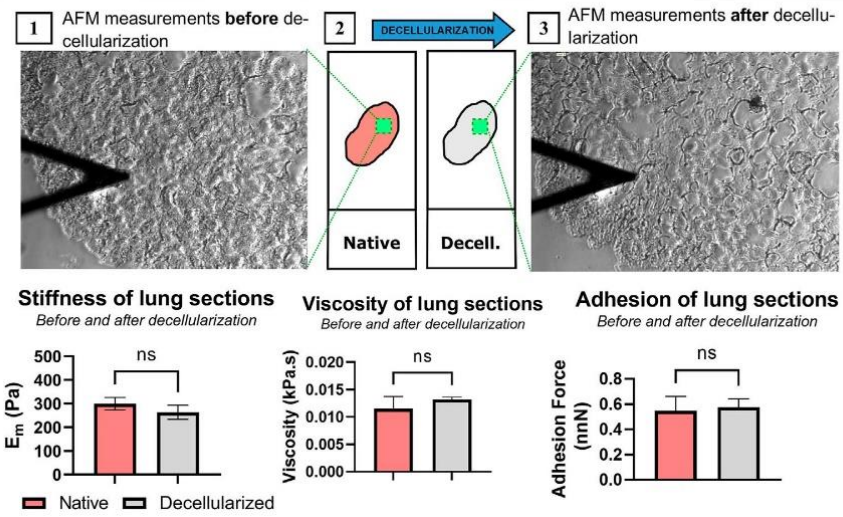

FIGURE 3 | Effect of the SD decellularization protocol on the mechanical properties of the lung scaffold. **(A)** Representative image of AFM measurements of the same tissue slice before (1) and after (3) decellularization ($n = 3$). Results of stiffness, viscosity, and adhesion force of the same sample before and after decellularization. Significance was $p < 0.05$.

slide; Ammonia + Triton, CHAPS and Triton treatments did not affect the attachment of the sample to the glass slide, for the most part, achieving 100 ± 00%, 82 ± 12%, and 100 ± 00% of sample attachment, respectively. For treatments that achieved higher cell removal—SDS and SD -, 32 ± 22% and 60 ± 23% of samples remained attached after decellularization treatments, respectively. By comparing all types of tissues, 60% of the lung sections remained attached while bladder, heart, and kidney sections never detached, achieving a sample attachment ratio of 100 ± 00% after using SD as the decellularizing agent. Taking into account the effectiveness in the removal of cellular material described in 3.1, the preservation of collagen, elastin, and laminin, and previous accounts of SDS's effects on the matrix, SD was considered to be the best treatment for on-slide decellularization. Thus, biomechanical, biocompatibility, and versatility analysis were performed on scaffolds resulting from the SD decellularization method.

3.4 SD Treatment did not Significantly Change the ECM Stiffness, Viscosity or Adhesion

The mean Young's modulus, viscosity, and force adhesion from each sample were computed from the same indentations and are shown in **Figure 3**. As expected, there was a slight, but not significant, decrease in the sample stiffness after decellularization. E_m for the native untreated samples was 299.6 ± 26.1 Pa while the E_m for the same sections but after decellularization was of 263.0 ± 29.9 Pa. Viscosity and force adhesion measurements were similar before and after decellularization (0.012 ± 0.002 vs. 0.013 ± 0.001 kPa·s and 0.48 ± 0.13 vs. 0.51 ± 0.01 nN, respectively). These results indicate that the decellularization protocol does not significantly change the mechanical properties of the lung sections.

3.5 SD Derived ECM Scaffolds are Biocompatible

The results of the biocompatibility assay were quantified and are detailed in **Figure 4.1**. Overall, cells survived similarly on both the 20 and 100 µm ECM scaffold thickness for 24, 48, and 72 h. More specifically, the viable cell ratio did not significantly differ after 24 h: at 72 h the cell viability ratio was 98.5 ± 2.0% and 97.9 ± 0.8% for 20 and 100 µm, respectively. After 72 h, the cell viability was similar to the cell count on the conventional culture flask (99.1 ± 0.8%). Accordingly, the distribution of the cells through the scaffold was assessed with a three-dimensional live/dead image and Z-distribution of the cells within the decellularized ECM structure can be seen in **Figure 4.2**. Alive cells were attached to the different parts of the matrix at different heights, which is an indicator of cell mobility and distribution within the lung scaffold. Previous topographical data indicates that lung scaffolds have gradual changes in height at the cellular level (around more or less 10 µm of variation), which is far below the variation in cell distribution seen in **Figure 4**. The cytoskeleton of the cells seeded on the matrix (**Figure 4.3**) shows a spread morphology indicative of their healthy attachment to the new scaffold.

3.6 The SD Method is Successful in Decellularizing Tissues From Different Animals and Organs

The quantification of the decellularization level of the mice's bladder, heart, and kidney is displayed in **Figure 5**, showing that

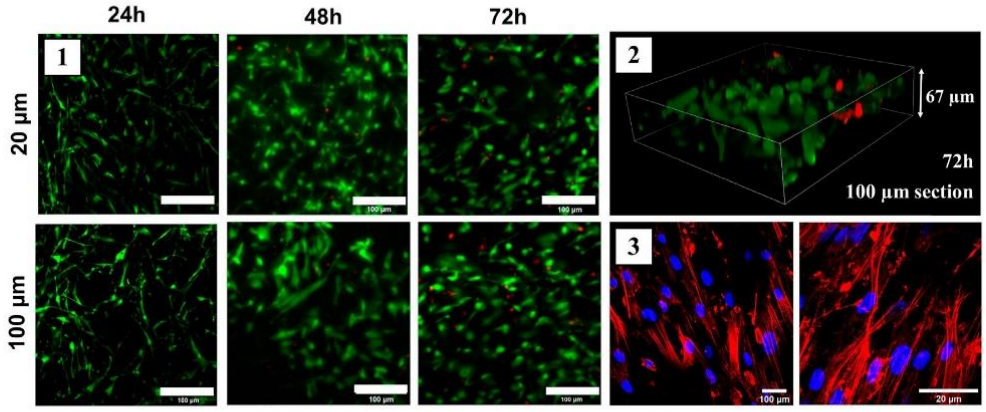

FIGURE 4 | Biocompatibility of the lung scaffold. Representative images of biocompatibility assay of 20 and 100 µm scaffolds for 24, 48, and 72 h. Live cells are seen in green while dead cells are red (1); 3D image of a 100 µm scaffold seeded with MSCs after 72 h. Stack showed covers 67 µm of the scaffold (2); Phalloidin staining of actin fibers (red) of cells seeded in 100 µm lung scaffold after 72 h (3). Samples decellularized with SD.

all organs were successfully decellularized. The decellularization level of the sections was quantified as described previously. Bladder decellularized sections had a mean value of 4% ± 1% of the native DNA signal intensity; kidney and heart decellularized sections both resulted in the same DNA intensity value of 1 ± 1% of the native DNA signal intensity value. It is important to note that, unlike lung samples, heart, kidney, and bladder samples remained attached for 100% of the decellularization trials. Porcine, rat, and mice lungs were decellularized and evaluated using the same protocol described previously. Lungs from the three different species were successfully decellularized (**Figure 5**). As expected, the decellularization of porcine and rat lung sections resulted in similar results to mice lung sections. Porcine lung sections averaged 5 ± 2% of the native DNA signal intensity while rat lung sections averaged 6 ± 2%. Mice lung decellularization with SD treatment was already described in **Figure 1**.

4 DISCUSSION

In this work, we present an easy, reliable, and versatile method to decellularize tissue sections attached to a glass slide with the main advantage that it allows for the identification and comparison of biophysical and biochemical conditions before and after decellularization from small samples. A summary of the comparison between the different decellularization treatments can be found in **Table 1**. After comparing common strategies for tissue decellularization, SD resulted in the most efficient treatment to remove cells and maintain the ECM components. This method has been successfully tested for other tissues including the heart, bladder, and kidneys, and in different species such as porcine, murine (mice and rat) lung samples. The resulting scaffolds showed no mechanical differences to the corresponding native sections, and could be repopulated with MSCs with high viability rates for at least 72 h. Therefore, this novel decellularization method provides a reliable alternative to current decellularization protocols due to its simplicity, lower sample mass requirements, and most importantly, it opens up new research opportunities to understand the role of the ECM in some physiologic and pathological conditions as well as for tissue repair and engineering.

Most of the available protocols for tissue decellularization are designed to decellularize whole organs or individual pieces of tissues not attached to a surface (da Palma et al., 2015; Urbano et al., 2017). Also, these protocols have been optimized for each organ and tissue type considering their structure and composition. To obtain a novel method capable to decellularize tissue samples attached to a glass slide, we compared and simplified the most common available protocols involving different techniques including perfusion, orbital agitation, and tissue immersion. The concentration employed for each decellularizing agent was the one previously optimized for lung tissues (see **Section 2.2** and **Supplementary Materials**). From all decellularizing agents included in this study, only SD and SDS were able to remove efficiently the cells. Although SDS is the most effective treatment (1 ± 0.5% remaining native DNA), it was also very aggressive resulting in a marked ECM degradation, particularly in elastin. In contrast to SDS, treatment with SD preserved much better the ECM structure and composition maintaining a high level of cell removal (6.5 ± 5.8% of native DNA). In addition, collagen I and III staining using Picro-Sirius red indicated a reduction in these proteins in samples treated with SDS (81%) but not with other treatments. Since immunostaining of collagen type I did not show such decrease, this reduction suggests a removal of collagen type III specifically in SDS treatment. Furthermore, samples treated with SDS remained attached to the glass slide only 32 ± 22% compared to the 60 ± 23% of sample attachment after SD treatment. Thus, the selected decellularization process achieved an optimal balance between cell removal, ECM integrity and sample attachment.

The degradation/preservation of each ECM component depends on the decellularizing strategy employed. The more aggressive behavior of SDS shown here is in agreement with

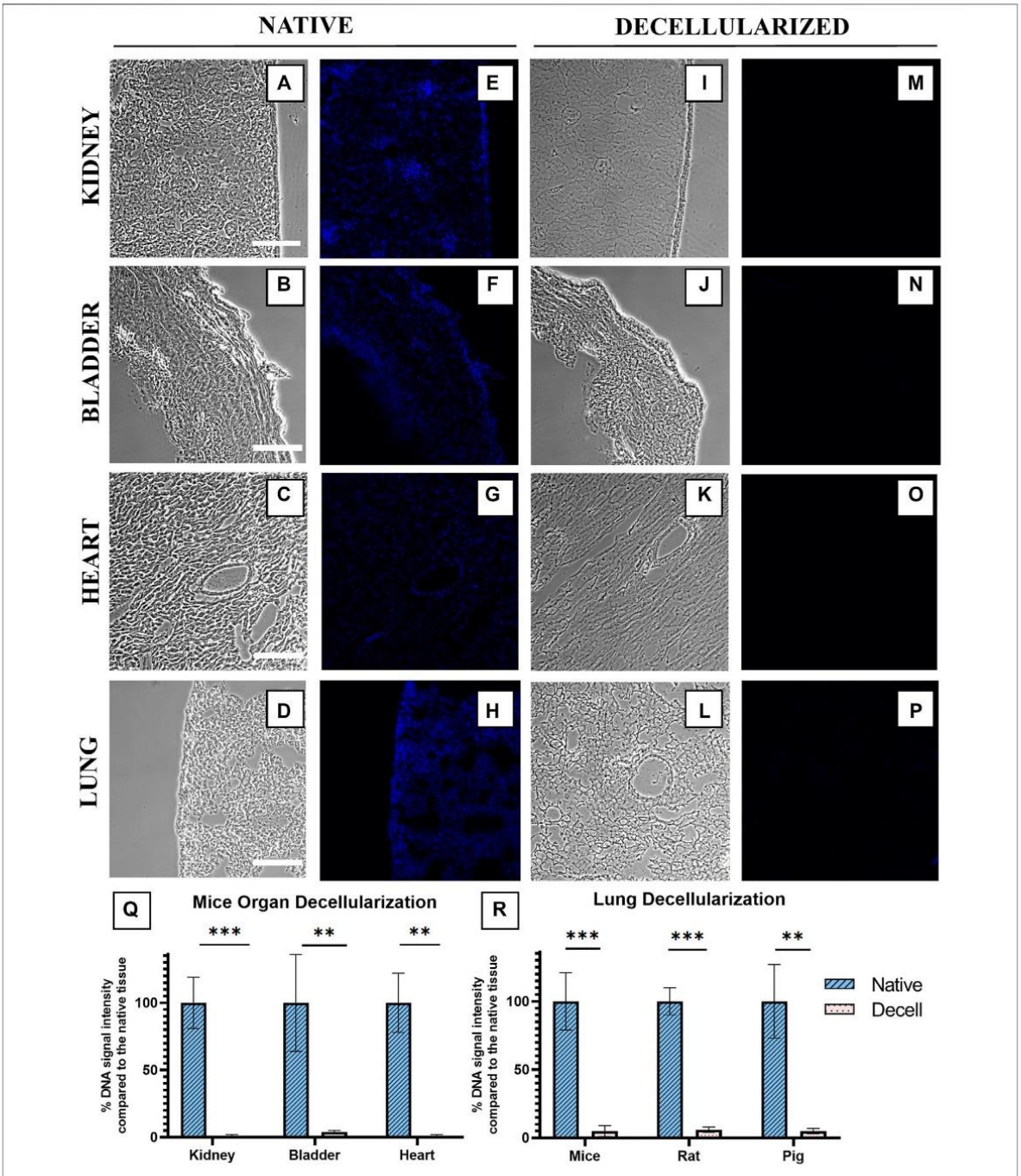

FIGURE 5 | Effect of the decellularization treatment with SD on the DNA signal of tissues of different animal origins and organs. Phase contrast **(A–D,I–L)** and Hoechst 33342 nuclei stained images **(E–H,M–P)** of native **(A–H)** and decellularized **(I–P)** sections of kidney, bladder, heart, and lung. Quantification of different organ DNA content percentage (%) **(Q)** and different animal lung tissue DNA content percentage (%) **(R)** after decellularization treatment with SD. Native tissue's DNA signal is normalized to 100%.

TABLE 1 | Summary of results (%DNA retention, % sample attachment, %collagen, elastin and laminin retention) for the different decellularization methods.

Decellularization method	DNA retention, %	Sample attachment, %	Elastin retention, %	Collagen I retention, %	Laminin retention, %
Ammonium hydroxide 0.5% + Triton 0.1%	57.4	100.0	13.2	112.5	135.5
CHAPS 0.5%	61.8	82.1	39.7	110.6	125.8
Sodium Deoxycholate (SD) 2%	6.5	60.0	33.4	118.0	136.6
Sodium Dodecyl Sulfate (SDS) 1%	0.95	32.1	6.2	121.5	115.8
Triton X-100 1%	66.8	100.0	40.0	101.3	106.8
Trypsin 0.05% + EDTA 0.02%	—	0	—	—	—

previous works. For instance, SDS promotes the denaturalization of the triple-helical collagen molecule while CHAPS and SD do not (Hwang et al., 2017) and reduce drastically the content of glycosaminoglycans (GAGs) (Ren et al., 2013). Additionally, White et al. found that SDS treatments lead to atypical phenotype, lower viability, and a reduced confluence of urothelial cells on decellularized scaffolds in contrast to SDS, Triton, and CHAPS treatments (White et al., 2017). Regarding ECM composition, none of the protocols tested in this work decreased the among of type I collagen or laminin. Elastin, which is known to be sensitive to the decellularization process (Maghsoudlou et al., 2013; O'Neill et al., 2013b; Alshaikh et al., 2020), was reduced for all decellularization methods tested. SDS and Ammonia + Triton, reduced the native elastin signal to 6%–13% while the other methods were able to preserve it better (30–40%). The sharp reduction in elastin signal was not hand in hand with levels of cellular removal; SDS was able to remove virtually all cellular material while the Ammonia + Triton mixture did not achieve sufficient decellularization levels (67 ± 28% of native DNA remained). This evidence suggests that the elastin decrease is influenced by the specific chemical interactions between decellularizing agents and the ECM network and not simply by the decellularization procedure. Additionally, by comparing the effect of the procedure on different organs, the elastin of bladder samples was highly preserved using the same SD based protocol, where 95 ± 36% of the native elastin signal was measured after decellularization (**Supplementary Figure S3**). Thus, elastin degradation seems to be organ-dependent and implicitly depend on the structure and organization of the ECM. Considering all these observations, although SDS is also extremely efficient in the removal of cellular material, we selected SD as the best option in terms of ECM preservation.

When comparing the effects of the decellularization procedure on the interstitial and basement membrane of the ECM, only a component of the interstitial ECM was significantly affected throughout procedures (elastin) while the component analyzed from the basement membrane (laminin) was not reduced in any of the treatments. This difference might be explained by the different locations of these layers: the interstitial ECM surrounds the cells and provides structural support to the tissue while the basement membrane is more compact (Cox and Erler 2011). This denser feature of the basement membrane might protect it from being removed during decellularization, while components from the interstitial ECM that are intertwined with the cells might be more vulnerable and disrupted when these are removed. Additionally, more components from both components of the ECM, like collagen type IV and fibronectin, could be analyzed for a more in-depth study on the effect of the decellularization procedure on the different layers of the ECM.

The key point in this novel method is to maintain the sample attached to the glass slide while applying the different decellularization solutions. Among all tissues employed, lungs have some unique features that could complicate their attachment. Specifically, lung scaffolds have large areas of empty spaces corresponding to the multiple alveoli and airways. These structures reduce the effective contact area between the scaffold and the glass slide in comparison to other more homogeneous tissues. While the lungs are being decellularized, the contact area with the glass slide can be further reduced by cellular removal leading to sample detachment during the different washes. For this reason, we selected lungs as the most difficult sample type to optimize the protocol. In fact, among all four organs tested in this work, the lungs were the only tissue where some samples would detach (40% for SD treatment) from the glass slide. Bladder, heart, and kidney samples remained attached to the glass slide for 100% of all experiments whilst reaching the same decellularization success using the same SD treatment. On the other hand, when testing solely lung samples, different detergents had dissimilar effects on the attachment of the slides. This could be explained by the effective contact area hypothesis just mentioned above, where the higher amount of cells removed, the smaller the contact area remaining with the glass slide and thus a higher chance of detachment. This is consistent with the results of this work, since the most effective decellularizing agents (SD and SDS) were less likely to preserve attachment when compared to less effective treatments, like triton and CHAPS. However, it is also worthy of note that ionic surfactants (SD and SDS) caused lower attachment levels when compared to non-ionic and zwitterionic surfactants (triton and CHAPS, respectively). Although the nature of this disruption is unclear, it is possible that the ionic nature of these reagents reacts with the ionic coating of the glass slides, disrupting it. We hypothesize that if this coating is replaced by a non-ionic treatment, attachment rates for treatments with SD and SDS might significantly improve.

Since this method maintains the sample attached to the glass slide, we were able to measure the mechanical properties of the same lung section before and after lung decellularization, unlike other protocols where mechanical properties are measured in different samples (Mendoza-Novelo et al., 2011; Maghsoudlou et al., 2013). In fact, it is possible to perform the decellularization *in situ* on the AFM stage, substantially reducing sources of variability. It is of the utmost importance that the scaffold

maintains the mechanical properties of the native tissue, especially for cell culture and tissue engineering applications. As expected, tissue stiffness, viscosity and adhesion were maintained after decellularization in agreement with previous works that indicate that elastin does not play a significant role in the mechanics of the static lung (Guimarães et al., 2020).

One of the potential limitations of this method is the diffusion of the decellularizing agents through thicker samples as well as the increased chance of detachment, since with increased thickness the electrostatic bonds that secure the sample to the glass slide are not strong enough to retain the increased sample mass. To demonstrate the effectiveness in thicker sections, we tested the same protocol in 100 µm sections reaching similar decellularization levels by employing a longer incubation period of DNAse of 40 min at 37°C. It should be noted however, that incubation at higher temperatures may result in increased sample detachment (Eckhard et al., 2019). Thus, we would advise the use of additional adhesion treatments that form stronger bonds between the sample and the glass slide, such as transglutaminase or cellTAK. Both these compounds have been used in the past to secure tissues to surfaces for AFM measurements (Sahai et al., 2016). Notwithstanding the potential applications of this method to thicker tissue sections, one of the main advantages of the method described here is the fact that the decellularization of tissue slice by slice requires a minimal amount of tissue and effort. One of the main problems with the decellularization of organs from humans and large animals like the pig is the complex procedure to decellularize the whole organ that can weight more than 1 kg. This process usually requires organ-specific decellularizing reagents which also are applied by different approaches (vascular/airways perfusion, site injections, among others) (Balestrini et al., 2015; Pouliot et al., 2016). Here, we tested the decellularization method for lung slices with samples from mice, rats, and pigs obtaining similar results. Thus, this will open the opportunity to decellularize tissue slices from small clinical biopsies where the whole or a large section of an organ is not available.

In conclusion, the decellularization method presented here will provide a useful tool for many research aims, but mainly in 1) studies that require the identification of anatomical structures which can only be detected in native samples. For instance, the location of small metastasis in decellularized tissue samples may present a challenge since cancer cells have been removed. Since this novel approach provides access to the sample before and after decellularization in the same or consecutive slices, the native structure can be located before decellularization. The low mass requirements make this protocol an important tool for 2) studies of scarce and valuable samples, since sections as low as 10 µm could be decellularized with this protocol, unlike full organ or tissue submergence decellularization protocols. This is the case for clinical biopsies or smaller structures like the cornea. And 3) to use the decellularized ECM as a cell culture substrate. To this end, the biocompatibility of the scaffolds was also assessed after 72 h. The decellularized lung scaffolds showed the capability of supporting cell attachment and growth similar to the conventional culture conditions, as further evidenced by actin staining showing the spread morphology of the cells within the scaffold. In addition, we observed that cells seeded on this lung scaffold did not form a monolayer in the surface but reached different depths within the decellularized ECM opening new options for tissue repair and engineering.

DATA AVAILABILITY STATEMENT

The raw data supporting the conclusion of this article will be made available by the authors, without undue reservation.

ETHICS STATEMENT

This work was approved by the Institutional Committee of Universitat de Barcelona and the Animal Experimentation Committee of regional authorities (Generalitat de Catalunya, OB 168/19 and 10972).

AUTHOR CONTRIBUTIONS

MN and IA participated in the conceptual framework of the project, analysed data, and drafted components of the manuscript. MN, AU, and CJ performed experiments. JO, RF, DN, and NG provided critical insights and participated in the drafting of the manuscript. MN and IA drafted the previous versions of the manuscript. IA, RF, and DN are responsible for the financial support of the project. All authors have reviewed and approved the final version of the manuscript.

FUNDING

IA is funded by Ministerio de Ciencia e Innovación (PID2019-108958RB-I00) and SEPAR (900-2019). MN and CJ were funded by the H2020 European Research and Innovation Programme under the Marie Skłodowska-Curie grant agreement "Phys2BioMed" contract no. 812772. RF, JO, and NG were funded by the Spanish Ministry of Sciences, Innovation and Universities, PID2020-113910RB-I00-AEI/10.13039/501100011033, PGC2018-097323-A-I00, and PID2020-116808RB-I00 AEI-Retos, respectively.

ACKNOWLEDGMENTS

The authors wish to thank Miguel Ángel Rodríguez from the Unit of Biophysics and Bioengineering (University of Barcelona) for his technical assistance.

SUPPLEMENTARY MATERIAL

The Supplementary Material for this article can be found online at: https://www.frontiersin.org/articles/10.3389/fbioe.2022.832178/full#supplementary-material

REFERENCES

Alshaikh, A. B., Padma, A. M., Dehlin, M., Akouri, R., Song, M. J., Brännström, M., et al. (2020). Decellularization and Recellularization of the Ovary for Bioengineering Applications; Studies in the Mouse. *Reprod. Biol. Endocrinol.* 18 (1), 75. doi:10.1186/s12958-020-00630-y

Balestrini, J. L., Gard, A. L., Liu, A., Leiby, K. L., Schwan, J., Kunkemoeller, B., et al. (2015). Production of Decellularized Porcine Lung Scaffolds for Use in Tissue Engineering. *Integr. Biol.* 7 (12), 1598–1610. doi:10.1039/c5ib00063g

Bonenfant, N. R., Sokocevic, D., Wagner, D. E., Borg, Z. D., Lathrop, M. J., Lam, Y. W., et al. (2013). The Effects of Storage and Sterilization on De-cellularized and Re-cellularized Whole Lung. *Biomaterials* 34 (13), 3231–3245. doi:10.1016/j.biomaterials.2013.01.031

Burgstaller, G., Oehrle, B., Gerckens, M., White, E. S., Schiller, H. B., and Eickelberg, O. (2017). The Instructive Extracellular Matrix of the Lung: Basic Composition and Alterations in Chronic Lung Disease. *Eur. Respir. J.* 50 (1), 1601805. doi:10.1183/13993003.01805-2016

Calle, E. A., Hill, R. C., Leiby, K. L., Le, A. V., Gard, A. L., Madri, J. A., et al. (2016). Targeted Proteomics Effectively Quantifies Differences between Native Lung and Detergent-Decellularized Lung Extracellular Matrices. *Acta Biomater.* 46 (December), 91–100. doi:10.1016/j.actbio.2016.09.043

Cox, T. R., and Erler, J. T. (2011). Remodeling and Homeostasis of the Extracellular Matrix: Implications for Fibrotic Diseases and Cancer. *Dis. Models Mech.* 4 (2), 165–178. doi:10.1242/dmm.004077

da Palma, R. K., Campillo, N., Uriarte, J. J., Oliveira, L. V. F., Navajas, D., and Farré, R. (2015). Pressure- and Flow-Controlled Media Perfusion Differently Modify Vascular Mechanics in Lung Decellularization. *J. Mech. Behav. Biomed. Mater.* 49 (September), 69–79. doi:10.1016/j.jmbbm.2015.04.024

Eckhard, A. H., O'Malley, J. T., Nadol, J. B., and Adams, J. C. (2019). Mechanical Compression of Coverslipped Tissue Sections during Heat-Induced Antigen Retrieval Prevents Section Detachment and Preserves Tissue Morphology. *J. Histochem. Cytochem.* 67 (6), 441–452. doi:10.1369/0022155419826940

Falcones, B., Sanz-Fraile, H., Marhuenda, E., Mendizábal, I., Cabrera-Aguilera, I., Malandain, N., et al. (2021). Bioprintable Lung Extracellular Matrix Hydrogel Scaffolds for 3D Culture of Mesenchymal Stromal Cells. *Polymers* 13 (14), 2350. doi:10.3390/polym13142350

Gattazzo, F., Urciuolo, A., and Bonaldo, P. (2014). Extracellular Matrix: A Dynamic Microenvironment for Stem Cell Niche. *Biochim. Biophys. Acta (Bba) - Gen. Subjects* 1840 (8), 2506–2519. doi:10.1016/j.bbagen.2014.01.010

Gilpin, A., and Yang, Y. (20172017). Decellularization Strategies for Regenerative Medicine: From Processing Techniques to Applications. *Biomed. Res. Int.* 2017, 1–13. doi:10.1155/2017/9831534

Guimarães, C. F., Gasperini, L., Marques, A. P., and Reis, R. L. (2020). The Stiffness of Living Tissues and its Implications for Tissue Engineering. *Nat. Rev. Mater.* 5 (5), 351–370. doi:10.1038/s41578-019-0169-1

Hill, R. C., Calle, E. A., Dzieciatkowska, M., Niklason, L. E., and Hansen, K. C. (2015). Quantification of Extracellular Matrix Proteins from a Rat Lung Scaffold to Provide a Molecular Readout for Tissue Engineering. *Mol. Cell Proteomics* 14 (4), 961–973. doi:10.1074/mcp.M114.045260

Hwang, J., Boi Hoa, S., Neill, J. T., Lisa, J. W., Denver, M. F., Stephen, F., et al. (2017). Molecular Assessment of Collagen Denaturation in Decellularized Tissues Using a Collagen Hybridizing Peptide. *Acta Biomat.* 53 (April), 268–278. doi:10.1016/j.actbio.2017.01.079

Hynes, R. O., and Naba, A. (2012). Overview of the Matrisome--An Inventory of Extracellular Matrix Constituents and Functions. *Cold Spring Harbor Perspect. Biol.* 4 (1), a004903. doi:10.1101/cshperspect.a004903

Jorba, I., Beltrán, G., Falcones, B., Suki, B., Farré, R., García-Aznar, J. M., et al. (2019). Nonlinear Elasticity of the Lung Extracellular Microenvironment Is Regulated by Macroscale Tissue Strain. *Acta Biomater.* 92 (July), 265–276. doi:10.1016/j.actbio.2019.05.023

Jorba, I., Uriarte, J. J., Campillo, N., Farré, R., and Navajas, D. (2017). Probing Micromechanical Properties of the Extracellular Matrix of Soft Tissues by Atomic Force Microscopy. *J. Cel. Physiol* 232 (1), 19–26. doi:10.1002/jcp.25420

Júnior, C., Narciso, M., Marhuenda, E., Almendros, I., Farré, R., Navajas, D., et al. (2021). Baseline Stiffness Modulates the Non-linear Response to Stretch of the Extracellular Matrix in Pulmonary Fibrosis. *Ijms* 22 (23), 12928. doi:10.3390/ijms222312928

Lü, W.-D., Zhang, L., Wu, C.-L., Liu, Z.-G., Lei, G.-Y., Liu, J., et al. (2014). "Development of an Acellular Tumor Extracellular Matrix as a Three-Dimensional Scaffold for Tumor Engineering, *PLoS ONE* 9 (7), e103672. doi:10.1371/journal.ponc.0103672

Maghsoudlou, P., Georgiades, F., Tyraskis, A., Totonelli, G., Loukogeorgakis, S. P., Orlando, G., et al. (2013). Preservation of Micro-architecture and Angiogenic Potential in a Pulmonary Acellular Matrix Obtained Using Intermittent Intra-tracheal Flow of Detergent Enzymatic Treatment. *Biomaterials* 34 (28), 6638–6648. doi:10.1016/j.biomaterials.2013.05.015

Mendibil, U., Ruiz-Hernandez, R., Retegi-Carrion, S., Garcia-Urquia, N., Olalde-Graells, B., and Abarrategi, A. (2020). Tissue-Specific Decellularization Methods: Rationale and Strategies to Achieve Regenerative Compounds. *Ijms* 21 (15), 5447. doi:10.3390/ijms21155447

Mendoza-Novelo, B., Avila, E. E., Cauich-Rodríguez, J. V., Jorge-Herrero, E., Rojo, F. J., Guinea, G. V., et al. (2011). Decellularization of Pericardial Tissue and its Impact on Tensile Viscoelasticity and Glycosaminoglycan Content. *Acta Biomater.* 7 (3), 1241–1248. doi:10.1016/j.actbio.2010.11.017

Narciso, M., Otero, J., Navajas, D., Farré, R., Almendros, I., and Gavara, N. (2021). Image-Based Method to Quantify Decellularization of Tissue Sections. *Ijms* 22 (16), 8399. doi:10.3390/ijms22168399

Ng, W. H., Ramasamy, R., Yong, Y. K., Ngalim, S. H., Lim, V., Shaharuddin, B., et al. (2019). Extracellular Matrix from Decellularized Mesenchymal Stem Cells Improves Cardiac Gene Expressions and Oxidative Resistance in Cardiac C-Kit Cells. *Regenerative Ther.* 11 (December), 8–16. doi:10.1016/j.reth.2019.03.006

O'Neill, J. D., Anfang, R., Anandappa, A., Costa, J., Javidfar, J., Wobma, H. M., et al. (2013a). Decellularization of Human and Porcine Lung Tissues for Pulmonary Tissue Engineering. *Bone* 96 (3), 1046–1056. doi:10.1016/j.athoracsur.2013.04.022.Decellularization

O'Neill, J. D., Anfang, R., Anandappa, A., Costa, J., Javidfar, J., Wobma, H. M., et al. (2013b). Decellularization of Human and Porcine Lung Tissues for Pulmonary Tissue Engineering. *Ann. Thorac. Surg.* 96 (3), 1046–1056. doi:10.1016/j.athoracsur.2013.04.022

Ohata, K., and Ott, H. C. (2020). Human-Scale Lung Regeneration Based on Decellularized Matrix Scaffolds as a Biologic Platform. *Surg. Today* 50 (7), 633–643. doi:10.1007/s00595-020-02000-y

Pompili, S., Latella, G., Gaudio, E., Sferra, R., and Vetuschi, A. (2021). The Charming World of the Extracellular Matrix: A Dynamic and Protective Network of the Intestinal Wall. *Front. Med.* 8 (April), 610189. doi:10.3389/fmed.2021.610189

Pouliot, R. A., Link, P. A., Mikhaiel, N. S., Schneck, M. B., Valentine, M. S., Kamga Gninzeko, F. J., et al. (2016). Development and Characterization of a Naturally Derived Lung Extracellular Matrix Hydrogel. *J. Biomed. Mater. Res.* 104 (8), 1922–1935. doi:10.1002/jbm.a.35726

Rasmussen, D. G. K., and Karsdal, M. A. (2016). "Laminins," in *Biochemistry of Collagens, Laminins and Elastin* (Amsterdam, Netherlands: Elsevier), 163–196. doi:10.1016/B978-0-12-809847-9.00029-5

Rebelo, L. M., de Sousa, J. S., Mendes Filho, J., and Radmacher, M. (2013). Comparison of the Viscoelastic Properties of Cells from Different Kidney Cancer Phenotypes Measured with Atomic Force Microscopy. *Nanotechnology* 24 (5), 055102. doi:10.1088/0957-4484/24/5/055102

Rendin, L. E., LöfdahlLöfdahl, A., Åhrman, E., Müller, C., Notermans, T., Michaliková, B., et al. (2019). Matrisome Properties of Scaffolds Direct Fibroblasts in Idiopathic Pulmonary Fibrosis. *Ijms* 20 (16), 4013. doi:10.3390/ijms20164013

Ren, H., Xiaolei, S., Liang, T., Jiangqiang, X., Bing, H., Yue, Z., et al. (2013). Evaluation of Two Decellularization Methods in the Development of a Whole-Organ Decellularized Rat Liver Scaffold. *Liver Int.* 33 (3), 448–458. doi:10.1111/liv.12088

Rosmark, O., Åhrman, E., Müller, C., Rendin, L. E., Eriksson, L., Malmström, A., et al. (2018). Quantifying Extracellular Matrix Turnover in Human Lung Scaffold Cultures. *Sci. Rep.* 8 (1), 5409. doi:10.1038/s41598-018-23702-x

Sahai, S., Marysuna, W., Ana Maria, Z., Scott, D. O., Charles, S. C., and Fabio, T. (2016). A Cost-Effective Method to Immobilize Hydrated Soft-Tissue Samples for Atomic Force Microscopy. *BioTechniques* 61 (4), 206–209. doi:10.2144/000114461

Schenke-Layland, K., Vasilevski, O., Opitz, F., König, K., Riemann, I., Halbhuber, K. J., et al. (2003). Impact of Decellularization of Xenogeneic Tissue on

Extracellular Matrix Integrity for Tissue Engineering of Heart Valves. *J. Struct. Biol.* 143 (3), 201–208. doi:10.1016/j.jsb.2003.08.002

Syed, O., Walters, N. J., Day, R. M., Kim, H.-W., and Knowles, J. C. (2014). Evaluation of Decellularization Protocols for Production of Tubular Small Intestine Submucosa Scaffolds for Use in Oesophageal Tissue Engineering. *Acta Biomater.* 10 (12), 5043–5054. doi:10.1016/j.actbio.2014.08.024

Urbano, J. J., da Palma, R. K., de Lima, F. M., Fratini, P., Guimaraes, L. L., Uriarte, J. J., et al. (2017). Effects of Two Different Decellularization Routes on the Mechanical Properties of Decellularized Lungs. *PLOS ONE* 12 (6), e0178696. doi:10.1371/journal.pone.0178696

White, L. J., Adam, J. T., Denver, M. F., Timothy, J. K., Lindsey, T. S., Janet, E. R., et al. (2017). The Impact of Detergents on the Tissue Decellularization Process: A ToF-SIMS Study. *Acta Biomat.* 50 (March), 207–219. doi:10.1016/j.actbio.2016.12.033

Wishart, A. L., Conner, S. J., Guarin, J. R., Fatherree, J. P., Peng, Y., McGinn, R. A., et al. (2020). Decellularized Extracellular Matrix Scaffolds Identify Full-Length Collagen VI as a Driver of Breast Cancer Cell Invasion in Obesity and Metastasis. *Sci. Adv.* 6 (43), eabc3175. doi:10.1126/sciadv.abc3175

Wüthrich, T., Lese, I., Haberthür, D., Zubler, C., Hlushchuk, R., Hewer, E., et al. (2020). Development of Vascularized Nerve Scaffold Using Perfusion-Decellularization and Recellularization. *Mater. Sci. Eng. C* 117 (December), 111311. doi:10.1016/j.msec.2020.111311

Xiong, G., Flynn, T. J., Chen, J., Trinkle, C., and Xu, R. (2015). Development of Anex Vivobreast Cancer Lung Colonization Model Utilizing a Decellularized Lung Matrix. *Integr. Biol.* 7 (12), 1518–1525. doi:10.1039/c5ib00157a

Zhang, J., Hu, Z. Q., Turner, N. J., Teng, S. F., Cheng, W. Y., Zhou, H. Y., et al. (2016). Perfusion-Decellularized Skeletal Muscle as a Three-Dimensional Scaffold with a Vascular Network Template. *Biomaterials* 89 (May), 114–126. doi:10.1016/j.biomaterials.2016.02.040

Zhu, M., Li, W., Dong, X., Yuan, X., Midgley, A. C., Chang, H., et al. (2019). *In Vivo* Engineered Extracellular Matrix Scaffolds with Instructive Niches for Oriented Tissue Regeneration. *Nat. Commun.* 10 (1), 4620. doi:10.1038/s41467-019-12545-3

Conflict of Interest: The authors declare that the research was conducted in the absence of any commercial or financial relationships that could be construed as a potential conflict of interest.

Publisher's Note: All claims expressed in this article are solely those of the authors and do not necessarily represent those of their affiliated organizations, or those of the publisher, the editors and the reviewers. Any product that may be evaluated in this article, or claim that may be made by its manufacturer, is not guaranteed or endorsed by the publisher.

Scientific Article II:

“A Fast and Efficient Decellularization Method for Tissue Slices”

This article was published in November 2022 to fulfil the specific objective (1): “To develop a method to decellularize tumor slices while preserving biochemical and biophysical extracellular matrix characteristics”. After comparing different decellularizing agents and testing the biocompatibility, mechanics, ECM preservation and cellular removal of the optimized protocol in Scientific Article I, we were invited to publish this protocol in a step-by-step format. Besides detailed information on the decellularization protocol, this article includes the sample preparation procedure, the cryosectioning protocol, tissue staining and subsequent imaging, in order to allow the reader to accurately replicate the method previously described.

bio-protocol www.bio-protocol.org/exxxx Bio-protocol 12(xx): exxxx. DOI:10.21769/BioProtoc.xxxx

A Fast and Efficient Decellularization Method for Tissue Slices

Maria Narciso[1, 2], Anna Ulldemolins[1], Constança Júnior[1, 2], Jorge Otero[1, 2, 3], Daniel Navajas[1, 2, 3], Ramon Farré[1, 3, 4], Núria Gavara[1, 2,] and Isaac Almendros[1, 3, 4, *]

[1]Unitat de Biofísica i Bioenginyeria, Facultat de Medicina i Ciències de la Salut, Universitat de Barcelona, Barcelona, Spain

[2]The Institute for Bioengineering of Catalonia (IBEC), The Barcelona Institute of Science and Technology, Barcelona, Spain

[3]CIBER de Enfermedades Respiratorias, Madrid, Spain

[4]Institut d'Investigacions Biomèdiques August Pi i Sunyer, Barcelona, Spain

*For correspondence: isaac.almendros@ub.edu

[Abstract] The study and use of decellularized extracellular matrix (dECM) in tissue engineering, regenerative medicine, and pathophysiology have become more prevalent in recent years. To obtain dECM, numerous decellularization procedures have been developed for the entire organ or tissue blocks, employing either perfusion of decellularizing agents through the tissue's vessels or submersion of large sections in decellularizing solutions. However, none of these protocols are suitable for thin tissue slices (less than 100 µm) or allow side-by-side analysis of native and dECM consecutive tissue slices. Here, we present a detailed protocol to decellularize tissue sections while maintaining the sample attached to a glass slide. This protocol consists of consecutive washes and incubations of simple decellularizing agents: ultrapure water, sodium deoxycholate (SD) 2%, and deoxyribonuclease I solution 0.3 mg/ml (DNase I). This novel method has been optimized for a faster decellularization time (2–3 hours) and a better correlation between dECM properties and native tissue-specific biomarkers, and has been tested in different types of tissues and species, obtaining similar results. Furthermore, this method can be used for scarce and valuable samples such as clinical biopsies.

Keywords: Decellularization, Extracellular Matrix, Tissue slices, Glass slide, Mechanobiology, Sodium deoxycholate

[Background] The extracellular matrix (ECM) is composed of more than 300 core structural components (Burgstaller et al., 2017), whose physical and chemical features regulate crucial cellular mechanisms (Gattazzo et al., 2014) including differentiation, migration, and proliferation. Thus, the study of the ECM is essential for understanding some pathological conditions and diseases including cancer and fibrosis (Elowsson Rendin et al., 2019, Wishart et al., 2020, Júnior et al., 2021). Also, decellularized extracellular matrix (dECM) scaffolds have many potential applications in tissue engineering and regenerative medicine. In fact, dECM has been used for the generation of ECM hydrogels (Marhuenda et al., 2022) and the recellularization of whole previously decellularized organs (Ohata and Ott, 2020), as well as several applications in the regeneration of tissues (Zhu et al., 2019). Therefore, it is not surprising the increased interest in physiomimetic tissue scaffolds by producing decellularized tissue samples (Mendibil et al., 2020).

Bio-protocol 12(xx): exxxx.
DOI:10.21769/BioProtoc.xxxx

The elimination of cells from tissue to obtain the ECM is possible by using physical, chemical, enzymatic, or a combination of these approaches (Mendibil et al., 2020). Physical strategies include freeze/thawing cycles, which induce ice crystals in the matrix, disrupting the cell membrane. Chemical strategies include detergents that solubilize the cell membrane and hypertonic or hypotonic solutions causing cell disruption by osmotic shock. Finally, enzymatic approaches can target the cell's nuclear material, such as with deoxyribonuclease (DNase), or the cell-ECM adhesion, such as with trypsin. However, the available decellularization protocols have important limitations. Many of them can take up to several days (Wishart et al., 2020, Wüthrich et al., 2020) and are still not particularly flexible or accessible since they are designed for the decellularization of full organs or thick sections (tissue blocks). This type of protocol would not suit the decellularization of many tissue samples, as is the case for clinical biopsies. In fact, clinical biopsies are scarce and cannot be decellularized by accessing the tissue's vasculature. Since no current protocols have explored the decellularization of glass-attached tissue sections, a method that allows for the study of the exact location before and after decellularization is needed to fill this gap.

The method presented here is significantly faster and less wasteful (i.e., can produce a single acellular tissue slice, instead of requiring a large sample portion) than other available methods, while maintaining the sample's mechanical properties and being suited for cell culture applications (Narciso et al., 2022). Additionally, it provides the option for studying the same tissue section before and after decellularization, which is invaluable for studies of certain pathologies and of scarce or valuable clinical samples. Patient biopsies, for example, are tested for several markers and histopathological features; hence, the entire sample cannot be decellularized. This method allows for studies of both native tissue and dECM to be carried out in the same sample. For early-stage tumors especially, this is of paramount importance as cancer cells are removed during decellularization and their location cannot be pinpointed. Furthermore, the tissue's architecture is preserved throughout decellularization by pre-attaching the samples to a glass slide. For tissues like bladder and lung, where organ inflation is required to emulate different conditions, this inflation can be performed on the native tissue, guaranteeing a more physiological result.

Materials and Reagents

1. Nail polish
2. Coverslips (Labbox, catalog number: COVN-050-100)
3. Blades (Ted Pella, Inc. St/Steel, Single Edge, 38 mm, catalog number: 121.4)
4. Slide tray (Histoline, Tray Slide Staining System, catalog number: M920-1)
5. 250 mL glass beaker (VWR, catalog number: 213-1124)
6. Pasteur pipettes 3 mL (Deltalab, catalog number: 200006.C.)
7. Hydrophobic pen (Sigma-Aldrich, catalog number: Z377821-1EA), storage: room temperature (RT)
8. SuperFrost Plus glass slides (ThermoFisher, Epredia™ SuperFrost Plus™ Adhesion slides, catalog number: 10149870), storage: RT
9. SuperFrost Gold glass slides (ThermoFisher, Epredia™ SuperFrost Ultra Plus™ GOLD Adhesion

Slides, catalog number: 11976299), storage: RT

10. Deoxyribonuclease I from bovine pancreas (Sigma-Aldrich, catalog number: DN25-1G), storage: -20 °C
11. $MgCl_2$ (Sigma-Aldrich, catalog number: M8266-1KG), storage: RT
12. $CaCl_2$ (Sigma-Aldrich, catalog number: C1016-500G), storage: RT
13. 1 M Tris-HCL, pH 7.5 (ThermoFisher, Invitrogen, Catalog number: 15567027), storage: 2–8 °C
14. Sodium deoxycholate (Sigma-Aldrich, Catalog number: D6750-500G), storage: RT
15. Ultrapure water/Milli-Q water (obtained via Equipment n° 5), storage: RT
16. PBS 10× (ThermoFisher, catalog number: 70011-036), storage: RT
17. Optimum cutting temperature (OCT) compound (Sakura, Tissue-Tek®, catalog number: 4583), storage: RT
18. Cryomolds (Sakura, Tissue-Tek® Cryomold® Standard 25 × 20 × 5 mm, catalog number: 4557)
19. Paraformaldehyde, 4% in PBS (ThermoFisher, catalog number: J61899.AK), storage: 2–8 °C
20. Corning® 50 mL centrifuge tubes (Sigma-Aldrich, catalog number: CLS430290-500EA), storage: RT
21. Hoechst 33342 staining (ThermoFisher, Invitrogen, Nucblue™ Live Cell Stain ReadyProbes™ reagent, catalog number: R37605), storage: 2–30 °C
22. Fluoromount (Southern Biotech, catalog number: 0100-01), storage: RT
23. Lint-free paper (KIMTECH Science Precision, catalog number: 7551), storage: RT
24. Fresh tissue sample (protocol tested on heart, lungs, bladder, and kidneys. Origins tested: murine and porcine)
25. DNAse solution (see Recipes)
26. SD 2% solution (see Recipes)

Equipment

1. Tweezers (rubisTech, catalog number: 1-SA)
2. Scale (Sartorius Lab Instruments, ENTRIS124I-1S, catalog number: 31603742)
3. Cryostat (Leica, Model CM3050S)
4. Vortex (Scientific Industries Inc., Vortex Genie 2, Model: G-560E)
5. Orbital shaker (IKA, Model: KS 130 basic, catalog number: 0002980000)
6. Milli-Q Gradient (Millipore, catalog number: ZMQ55V001)
7. Inverted microscope (Leica, SP5) equipped with a CCD camera (Hamamatsu Photonics C9100) and using a 10× Plan Fluor objective (Nikon, Tokyo, Japan)
8. Incubator (Nuaire, model: NU-4750)

Software

1. ImageJ (National Institutes of Health, LOCI, University of Wisconsin, https://imagej.nih.gov/ij/)

Bio-protocol 12(xx): exxxx.
DOI:10.21769/BioProtoc.xxxx

Procedure

A. Sample preparation and OCT embedding

Tip: Work near a -80 °C freezer.

1. After tissue retrieval from the animal/patient, place the sample in an appropriate container and keep refrigerated on ice for up to 2 h. For longer periods of time, freeze the sample at -80 °C and remove it from the freezer before OCT embedding until the sample is completely thawed.
2. Choose the appropriate size of cryomold for your sample so that the sample has at least 0.5 cm between the sample and the walls of the cryomold.
3. Place a single drop of OCT compound in the center of the cryomold.
4. With the help of tweezers, position your fresh tissue sample in the center.
   Note: For some applications, the tissue can also be positioned in a specific orientation in relation to the blade.
5. Cover the whole tissue sample with OCT, without overflowing the cryomold.
   Tip: Pour the OCT compound without squeezing the tube to avoid air bubbles, which can interfere with cryosectioning. Make sure there is a thick layer of OCT on top of the sample in a way that the surface of the OCT is as smooth as possible. If any bubbles have formed, gently remove them by slowly aspirating with a pipette.
   Place the cryomold with the sample in the freezer on a flat surface.
   Tip: Depending on the type of tissue used, the sample will tend to float on the OCT, so it is important to freeze as soon as possible.
   Note: Other freezing procedures, such as snap freezing with liquid nitrogen, dry ice, liquid nitrogen vapors, or freezing at -20 °C, are also compatible with this protocol.
6. Let the samples freeze overnight.

B. Tissue sectioning

1. Set the appropriate cryostat temperature for the tissue sample to be sliced.
   Note: The cryostat temperature will have to be optimized depending on the device used and the tissue to be sliced. In the setup described, the temperature that produces the best tissue sections for lungs and heart is -18 °C to -20 °C, for bladder is -20 °C to -22 °C, and for liver is -15 °C to -18 °C.
2. Place the blade inside the cryostat at least 20 min before use.
3. Withdraw the sample from the freezer and place it inside the cryostat for 30 min before sectioning.
4. Trim the beginning of the cryoblock until reaching the sample.
5. Select the desired thickness.
   Note: For mechanical testing we suggest 20–30 µm sections, while for tissue staining and imaging we suggest 10 µm.

6. Section the samples.
7. Carefully make contact between the positive area of the glass slide and the tissue section (depending on the size of your sample, you can place 1–3 consecutive tissue sections in one glass slide).
   Note: For thicker sections (50 µm and higher) consider using a more adhesive glass slide, like Superfrost Gold.
8. Allow the samples to dry at RT for 10–20 min.
9. Store the samples at -80 °C.

C. Tissue section decellularization (10–70 µm sample thickness)
1. Withdraw samples from the freezer and place them on the slide tray (sample side up).
2. Allow samples to thaw at room temperature for 20 min.
3. Trace the edges of the sample with a hydrophobic pen and allow the ink to completely dry for 1 min.
4. Using a Pasteur pipette, cover the sample in PBS 1× for 20 min (RT) to remove the OCT compound. Please note that depending on the tissue size, the volume required to cover the sample could vary from 100 µL to up to 1 mL.
   Tip: When pouring liquid during decellularization, never pour it directly on top of the sample to avoid damaging or detaching the tissue. Also avoid adding the liquid as droplets, as that might also create too much turbulence. Instead, approach the tip of the pipette to a nearby bare glass region of the sample and slowly deposit the liquid in a continuous flow.
5. Remove the PBS (and all other incubations throughout the decellularization) by inverting the glass slide over the glass beaker.
   Warning: Be quick in between washes so as to never let the sample completely dry.
6. Cover the sample in Milli-Q water for 10 min to provoke cell lysis.
7. Remove the Milli-Q water by inversion and repeat step C6.
8. Remove the Milli-Q water by inversion.
9. Cover the sample in SD 2% solution for 15 min.
10. Remove the SD 2% solution by inversion.
11. Cover the sample again in SD 2% solution for 15 min.
12. Remove the SD 2% solution by inversion.
    Tip: In the following steps, be careful when inverting the glass slide over the glass beaker, as the SD solution with cell remnants is extremely viscous and could damage the sample if done too quickly.
13. Incubate with PBS 1× for 5 min and remove it by inverting the sample.
14. Repeat step C13 three times.
15. With the Pasteur pipette, aspirate and release the solution of DNase to ensure it is homogeneous (and that the DNase does not sink to the bottom).
16. Cover the sample in DNase solution and incubate at RT for 20 min.

Bio-protocol 12(xx): exxxx.
DOI:10.21769/BioProtoc.xxxx

17. Remove the DNase by inversion and repeat step C13 three times.
18. Leave the sample in PBS until further staining or testing. Do not allow to dry.

D. Tissue section decellularization (70–100 µm sample thickness)

For the decellularization of thicker tissue sections, follow section C with these alterations to the following steps:

(Instead of step C2)—Allow samples to thaw at RT for 40 min.

(Instead of step C4)—To remove the OCT compound from the sample, cover the sample in PBS 1× and incubate for 30 min.

(Instead of step C16)—Cover the sample in the DNase solution and incubate at 37 °C for 40 min.

For short-term storage (<24 h), non-fixed decellularized samples can be left in PBS at 4 °C. For long-term storage (1–10 days), we advise fixing samples in PFA for 15 min, removing the PFA with PBS, and leaving the samples in 50 mL PBS-filled tubes at 4 °C. Do not freeze thin decellularized samples to avoid ice crystal formation and structural damage to the samples.

E. Nuclear staining and mounting

Note: Any nuclear stain like DAPI or Hoechst 33342 would work for decellularization quantification.

1. Thaw consecutive tissue sections for 20 min at RT.
2. Trace the edges of the sample with a hydrophobic pen and allow the ink to completely dry for 1 min.
3. Remove the OCT compound from the native sample by covering it in PBS 1× for 20 min.
4. Prepare the Nucblue Hoechst 33342 staining solution according to the manufacturer's instructions (2 drops per mL of PBS).
5. Cover both the native and decellularized sample in Nucblue solution and protect the slide tray from light.
6. Incubate for 20 min at 80 rpm using an orbital shaker at RT.
7. Remove the Nucblue solution by inversion and wash the samples three times with PBS for 5 min each wash.

   Note: Keep your samples protected from light as much as possible in between washes. If no opaque slide tray lid is available, aluminum foil paper will suffice.
8. Remove the excess PBS from the glass slide by inversion.
9. Add a drop of fluoromount from the container and place it on top of your samples so as not to touch it directly.

   Tip: Do this step by using a yellow pipette tip to avoid bubble formation.
10. With the tweezers, remove the coverslip from the container and very carefully place one edge of the coverslip on one of the sides of the sample. Slowly lower the other edge until it covers the sample. Avoid dropping the coverslip on top of the sample as this will create bubbles on the sample.

Bio-protocol 12(xx): exxxx.
DOI:10.21769/BioProtoc.xxxx

11. With nail polish, trace the edges of your coverslip and secure the coverslip to the glass slide.
12. Wait for it to dry and store at 4 °C protected from light.

F. Image acquisition and decellularization quantification

Tip: Use a low magnification objective to image as much tissue area as possible (5×–20×)

1. Place the samples at room temperature 30 min before imaging.
2. Clean the glass slides with lint-free paper and ethanol 70%.
3. Image the native tissue sample and set the UV (420 nm) exposure as high as possible without causing pixel saturation (Figure 1B).
4. Acquire 5–10 image sets of phase contrast and UV fluorescence (Figure 1A and 1B).
5. Image decellularized samples using the same exposure settings (Figure 1C, and 1D).

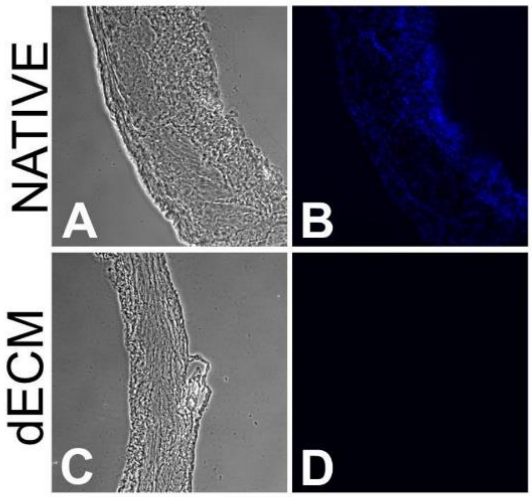

Figure 1. Representative images of the decellularization of mice bladder (20 µm)

Phase contrast images of a native (A) and decellularized (C) 20 µm mice bladder tissue section and corresponding UV images (B and D, respectively). Contrast was increased in phase contrast images for the sake of readability.

Data analysis

1. Open ImageJ.
2. Drag the phase contrast image and its corresponding UV image to ImageJ.
3. Using the *Freehand selections* tool, trace the edges of the sample in the phase-contrast photo.
4. Edit > Selections > Create mask, to obtain Figure 2B.
5. Edit > Selections > Create selection.
6. On the UV image: Shift+E to apply the selection (Figure 2C).

Bio-protocol 12(xx): exxxx.
DOI:10.21769/BioProtoc.xxxx

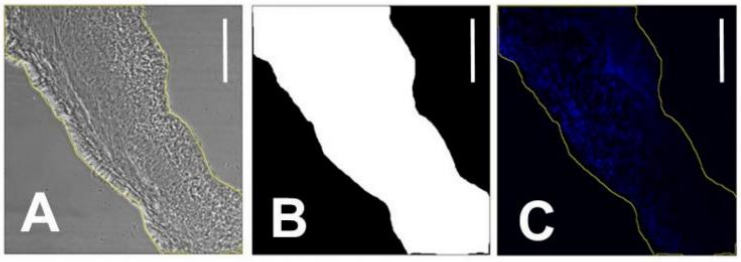

Figure 2. Decellularization quantification

A. Phase contrast image of a 20 µm mice bladder tissue section with the freehand outline in yellow; B. Mask of the outline of A; C. Area of interest selection of the corresponding UV image. Scale bar = 200 µm

7. Analyze > Set Measurements > Mean gray value > OK.
8. Analyze > Measure.
9. Repeat this procedure for all native and decellularized images to obtain the mean signal intensity of the nuclear staining for both groups (Figure 3).

Tip: The approach described in this protocol is manual. For an automatic approach, you can use the previously described algorithm for decellularization quantification (Narciso et al., 2021).

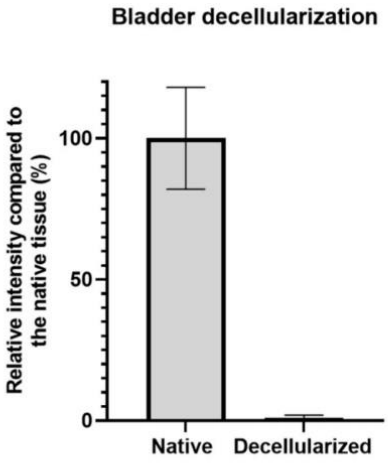

Figure 3. Representative signal quantification results of bladder decellularization

The left bar represents the mean UV intensity signal (± SD) for native bladder samples stained with Hoechst 33342 that was normalized to 100%, while the right bar represents the mean intensity signal of the decellularized bladder sections.

Recipes

1. DNase solution

Reagent	Final concentration	Amount
Deoxyribonuclease I from bovine pancreas	0.3 mg/mL	3 mg
Tris-HCl (1 M, pH 8.0)	10%	100 µL
$MgCl_2$	10 mM	9.5 mg
$CaCl_2$	10 mM	11 mg
H_2O (ultrapure)	n/a	9.9 mL
Total	n/a	10 mL

2. SD 2% solution

Reagent	Final concentration	Amount
Sodium deoxycholate	2%	0.2g
H_2O (Ultrapure)	n/a	(until reaching a total of 10 mL)
Total	n/a	10 mL

Acknowledgments

This protocol was derived from the previously published work "Novel Decellularization Method for Tissue Slices" in *Frontiers in Bioengineering and Biotechnology* in March 2022 (Narciso et al., 2022).

The authors acknowledge the funding received: IA is funded by Ministerio de Ciencia e Innovación (PID2019-108958RB-I00 / AEI/ 10.13039/501100011033) and SEPAR (900-2019). MN and CJ were funded by the H2020 European Research and Innovation Programme under the Marie Skłodowska-Curie grant agreement "Phys2BioMed" contract no. 812772. The Spanish Ministry of Sciences funded RF, JO, and NG, Innovation and Universities, PID2020-113910RB-I00-AEI/10.13039/501100011033, PGC2018-097323-A-I00, and PID2020-116808RB-I00 AEI-Retos, respectively.

Competing interests

There are no conflicts of interest or competing interests.

Ethics

All animal procedures were approved by the Institutional Committee of Universitat de Barcelona and the Animal Experimentation Committee of regional authorities (Generalitat de Catalunya, OB 168/19 and 10972).

References

1. Burgstaller, G., Oehrle, B., Gerckens, M., White, E. S., Schiller, H. B. and Eickelberg, O. (2017). The instructive extracellular matrix of the lung: basic composition and alterations in chronic lung disease. *Eur Respir J* 50(1).
2. Elowsson Rendin, L., Lofdahl, A., Ahrman, E., Muller, C., Notermans, T., Michalikova, B., Rosmark, O., Zhou, X. H., Dellgren, G., Silverborn, M., et al. (2019). Matrisome Properties of Scaffolds Direct Fibroblasts in Idiopathic Pulmonary Fibrosis. *Int J Mol Sci* 20(16).
3. Gattazzo, F., Urciuolo, A. and Bonaldo, P. (2014). Extracellular matrix: a dynamic microenvironment for stem cell niche. *Biochim Biophys Acta* 1840(8): 2506-2519.
4. Junior, C., Narciso, M., Marhuenda, E., Almendros, I., Farre, R., Navajas, D., Otero, J. and Gavara, N. (2021). Baseline Stiffness Modulates the Non-Linear Response to Stretch of the Extracellular Matrix in Pulmonary Fibrosis. *Int J Mol Sci* 22(23).
5. Marhuenda, E., Villarino, A., Narciso, M. L., Camprubi-Rimblas, M., Farre, R., Gavara, N., Artigas, A., Almendros, I. and Otero, J. (2022). Lung Extracellular Matrix Hydrogels Enhance Preservation of Type II Phenotype in Primary Alveolar Epithelial Cells. *Int J Mol Sci* 23(9).
6. Mendibil, U., Ruiz-Hernandez, R., Retegi-Carrion, S., Garcia-Urquia, N., Olalde-Graells, B. and Abarrategi, A. (2020). Tissue-Specific Decellularization Methods: Rationale and Strategies to Achieve Regenerative Compounds. *Int J Mol Sci* 21(15).
7. Narciso, M., Otero, J., Navajas, D., Farre, R., Almendros, I. and Gavara, N. (2021). Image-Based Method to Quantify Decellularization of Tissue Sections. *Int J Mol Sci* 22(16).
8. Narciso, M., Ulldemolins, A., Junior, C., Otero, J., Navajas, D., Farre, R., Gavara, N. and Almendros, I. (2022). Novel Decellularization Method for Tissue Slices. *Front Bioeng Biotechnol* 10: 832178.
9. Ohata, K. and Ott, H. C. (2020). Human-scale lung regeneration based on decellularized matrix scaffolds as a biologic platform. *Surg Today* 50(7): 633-643.
10. Wishart, A. L., Conner, S. J., Guarin, J. R., Fatherree, J. P., Peng, Y., McGinn, R. A., Crews, R., Naber, S. P., Hunter, M., Greenberg, A. S., et al. (2020). Decellularized extracellular matrix scaffolds identify full-length collagen VI as a driver of breast cancer cell invasion in obesity and metastasis. *Sci Adv* 6(43).
11. Wüthrich, T., Lese, I., Haberthur, D., Zubler, C., Hlushchuk, R., Hewer, E., Maistriaux, L., Gianello, P., Lengele, B., Rieben, R., et al. (2020). Development of vascularized nerve scaffold using perfusion-decellularization and recellularization. *Mater Sci Eng C Mater Biol Appl* 117: 111311.
12. Zhu, M., Li, W., Dong, X., Yuan, X., Midgley, A. C., Chang, H., Wang, Y., Wang, H., Wang, K., Ma, P. X., et al. (2019). In vivo engineered extracellular matrix scaffolds with instructive niches for oriented tissue regeneration. *Nat Commun* 10(1): 4620.

Scientific Article III:

“Image-Based Method to Quantify Decellularization of Tissue Sections”

This article was published in August 2021 to fulfil the specific objective (2): “To design a novel image-based method to better quantify the decellularization process in tissue and tumor sections”.

International Journal of
Molecular Sciences

MDPI

Article

Image-Based Method to Quantify Decellularization of Tissue Sections

Maria Narciso [1,2], Jorge Otero [1,2,3], Daniel Navajas [1,2,3], Ramon Farré [1,3,4], Isaac Almendros [1,3,4] and Núria Gavara [1,2,*]

1 Unitat de Biofísica i Bioenginyeria, Facultat de Medicina i Ciències de la Salut, Universitat de Barcelona, 08036 Barcelona, Spain; mnarciso@ibecbarcelona.eu (M.N.); jorge.otero@ub.edu (J.O.); dnavajas@ub.edu (D.N.); rfarre@ub.edu (R.F.); isaac.almendros@ub.edu (I.A.)
2 The Institute for Bioengineering of Catalonia (IBEC), The Barcelona Institute of Science and Technology (BIST), 08028 Barcelona, Spain
3 CIBER de Enfermedades Respiratorias, 28029 Madrid, Spain
4 Institut d'Investigacions Biomèdiques August Pi i Sunyer, 08036 Barcelona, Spain
* Correspondence: ngavara@ub.edu

Abstract: Tissue decellularization is typically assessed through absorbance-based DNA quantification after tissue digestion. This method has several disadvantages, namely its destructive nature and inadequacy in experimental situations where tissue is scarce. Here, we present an image processing algorithm for quantitative analysis of DNA content in (de)cellularized tissues as a faster, simpler and more comprehensive alternative. Our method uses local entropy measurements of a phase contrast image to create a mask, which is then applied to corresponding nuclei labelled (UV) images to extract average fluorescence intensities as an estimate of DNA content. The method can be used on native or decellularized tissue to quantify DNA content, thus allowing quantitative assessment of decellularization procedures. We confirm that our new method yields results in line with those obtained using the standard DNA quantification method and that it is successful for both lung and heart tissues. We are also able to accurately obtain a timeline of decreasing DNA content with increased incubation time with a decellularizing agent. Finally, the identified masks can also be applied to additional fluorescence images of immunostained proteins such as collagen or elastin, thus allowing further image-based tissue characterization.

Keywords: segmentation; decellularization; microscopic image; fluorescence image; image processing

Citation: Narciso, M.; Otero, J.; Navajas, D.; Farré, R.; Almendros, I.; Gavara, N. Image-Based Method to Quantify Decellularization of Tissue Sections. *Int. J. Mol. Sci.* **2021**, *22*, 8399. https://doi.org/10.3390/ijms22168399

Academic Editor: Alexandre Mironov

Received: 1 June 2021
Accepted: 2 August 2021
Published: 5 August 2021

1. Introduction

Tissue decellularization has become a very relevant method in recent years. On the one hand, the production of acellular scaffolds has applications in cell culture, tissue repair and regenerative medicine, while on the other hand, the study of the extracellular matrix (ECM) and its interactions with their homing cells can yield further understanding of multiple diseases and pathologies [1]. The ECM which remains after decellularization is composed of different proteins that provide structural support as well as physical and chemical signals to the cells that were embedded in it [2]. As such, it is important to guarantee that the ECM is preserved as much as possible while also assuring full cellular removal. Among other methods, the removal of cells from the ECM is often performed by a detergent, an enzymatic treatment, or a mix of both, followed by a DNA degradation step, usually benzonase or deoxyribonuclease (DNAse) [3].

To assess the decellularization of the tissue, the standard approach is to use absorbance-based DNA quantification [4–7]. This step can be performed with commercially available kits that typically work by digesting a piece of the decellularized tissue, isolating and purifying its DNA and using a spectrophotometer to measure the amount of DNA content per mg of dry tissue. While this method provides an initial quantitative estimate of DNA

content, the tissue is conventionally classified as either successfully decellularized or not, depending on whether it passes the gold standard set by Crapo et al. in 2011 [8]: tissues are considered decellularized if their DNA content is below 50 ng per mg of dry tissue. In addition, cell nuclei can be visualized with a histological stain such as Hematoxylin and Eosin (H&E) [9–11] or by staining the DNA using 4',6-Diamidino-2-Phenylindole, Dihydrochloride (DAPI) or Hoechst 33342 [10,12–14]. Optical microscopy images are then used to confirm the lack of visible nuclei when compared to the native tissue. The absence of or reduction in cell nuclei is usually measured in a qualitative manner, but some image processing tools such as 'HisTOOLogy' [15] have used the number of nuclei from H&E staining to quantitatively determine the decellularization of liver samples when compared to native tissue. Other decellularization assessment methods include the actual presentation of the organ, e.g., organ discoloration (from pink/red to white/transparent), as sufficient evidence of cellular removal [16]. Crapo et al. also suggested that the DNA fragment length should be below 200 bp; however, this metric is rarely assessed.

Even though these decellularization assessment methods are suitable for certain applications, they are not without drawbacks. 'HisTOOLogy', for instance, only takes into consideration the number of cell nuclei as a parameter for decellularization and cannot account for the DNA that has been released from the nucleus but is still present in the matrix. This measurement is extremely important especially for cell culture and tissue engineering applications, where DNA presence can be detrimental. DNA quantification kits, on the other hand, are time consuming and are preferentially suitable for full organ decellularization methods that provide large amounts of sample tissue. In the cases where decellularization is performed slice by slice, or biological material is scarce, such as in human biopsies, acquiring the minimum amount of tissue required to achieve a reliable readout may be prohibitive. In addition, DNA quantification kits require the digestion and consequent destruction of the probed tissue sample, an issue that further complicates matters in scarce samples. Finally, these kits are typically performed on a batch-by-batch basis to confirm the success of the decellularization protocol and assume the tissue is uniformly decellularized, disregarding inter- and intrasample variability considerations.

In this regard, it should be mentioned that biological tissue is heterogeneous. Taking the lung as an example, the alveoli and the pleura region have different cell and matrix distributions as well as different micromechanical properties [17,18]. These locations also have different components and structural organization of their ECM, which may cause the decellularization process to display heterogeneity across the tissue. This likely occurs when the aim of the decellularization process is to preserve and later visualize the 3D structure, composition, or mechanical properties of the ECM, and thus a milder agent is used. Therefore, there is a need for a minimally wasteful quantitative method that can reliably assess tissue decellularization via DNA quantification in a fast and simple manner. Accordingly, we propose an image-based approach that can quantify DNA content based on the combination of the DNA staining fluorescence image of cell nuclei and the phase contrast (PC) image of the (de)cellularized tissue.

Nuclear staining is extensively used for cell segmentation techniques [19,20], where the aim is to pinpoint nuclei or individual cells rather than to obtain quantitative measurements of their DNA content. However, in the decellularization protocol the nuclei are disrupted, causing the remaining DNA to diffuse throughout the tissue attaching itself to the remaining ECM. Additionally, DNA fluorescence intensity is expected to decrease and lose any distinct organization that can be easily segmented in decellularized (or partially decellularized) samples. Consequently, this fluorescence channel becomes unreliable for image segmentation strategies, raising the need for alternatives. As a solution, our novel method proposes the use of phase contrast images for tissue segmentation purposes only. Our protocol simply adds an extra step that can be readily incorporated in the standard acquisition of images of the UV fluorescence channel and any other immunohistochemistry fluorophores of interest. As such, the phase contrast image is used to segment a mask of the tissue of interest with respect to the naked glass substrate, whereas the fluorescence

images are used for fluorescence intensity quantification purposes. We thus propose a novel method that offers quantitative information on the decellularization level of the sample and potentially also on the presence and organization of matrix proteins such as collagen or elastin, whilst using a minimal amount of biological tissue.

2. Results

The schematic layout of the image processing algorithm employed is illustrated in Figure 1. This algorithm segments PC images based on the entropy (or heterogeneity) of the tissue. Areas corresponding to tissue are expected to have high heterogeneity while areas corresponding to glass are expected to have low heterogeneity (represented in Figure 2A). Accordingly, an entropy filter is first run over the sample, and the resulting image is then thresholded to achieve a mask. Pixels from highly entropic areas (tissue) are included in a mask while pixels corresponding to the background are not. This mask is then applied to the UV fluorescence image, so that DNA signal intensity is measured only in the pixels that have been previously identified as belonging to tissue. Further details of each step can be found in the Materials and Methods section.

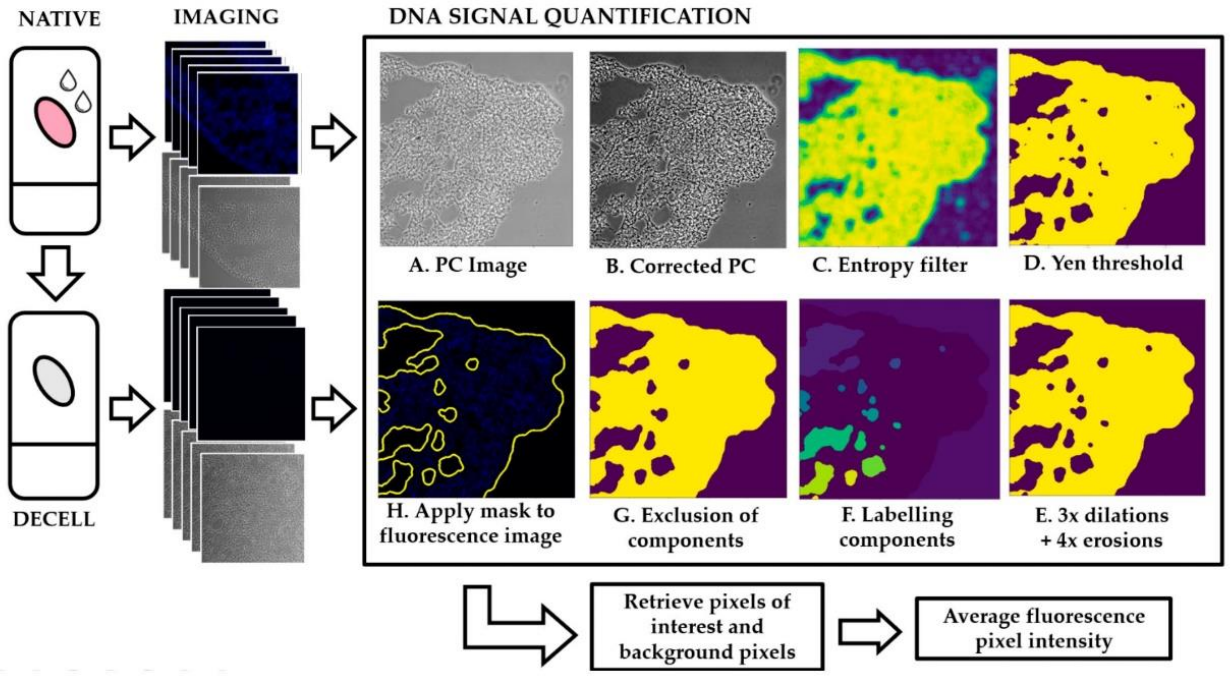

Figure 1. Schematic layout of the image processing pipeline. Native and decellularized samples are imaged and sets of image pairs (PC + UV) are taken. UV signal quantification: (**A**) the PC image is selected and (**B**) normalized for increased contrast. (**C**,**D**) An entropy filter is applied where high entropy regions correspond to high intensity regions and low entropy regions correspond to low intensity regions. (**E**) Three dilations followed by three erosions are applied to create smaller pixels aggregates and (**F**) these components are labelled. (**G**) Components are excluded/included in the mask depending on number of pixels. (**H**) The mask is applied to the UV image to identify pixels of interest corresponding to tissue vs. the background.

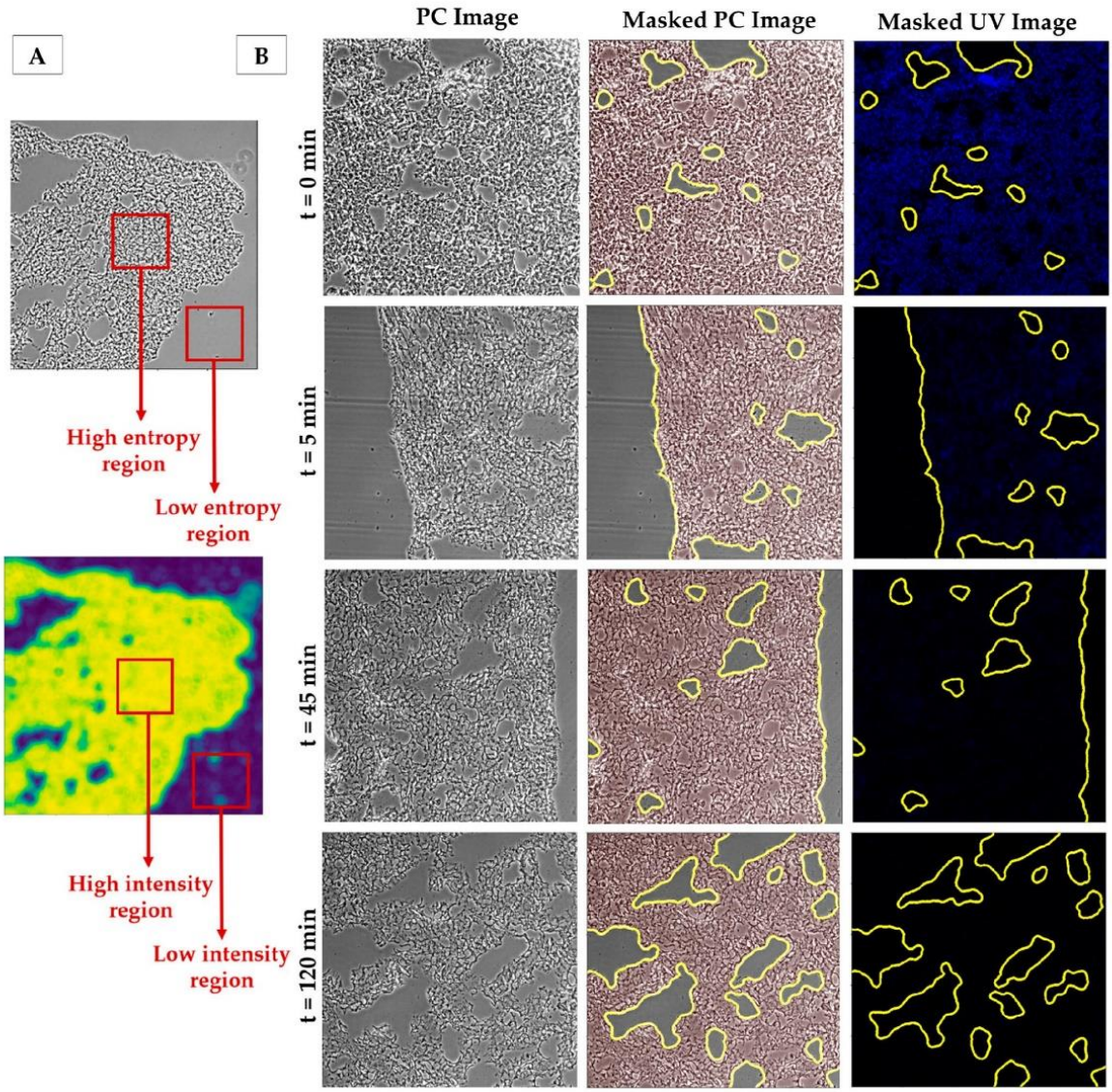

Figure 2. (**A**) Representation of the entropy-based segmentation: high entropy regions in the phase contrast image correspond to high intensity regions output image of the entropy filter. Low entropy regions corresponding to the background will result in low intensity regions in output of the entropy filter. (**B**) Examples of PC images (**left**), masks obtained using our algorithm superimposed on the corresponding PC image (**centre**) and their corresponding UV fluorescent images with the superimposed mask (**right**). Contrast of PC images has been increased here for the sake of readability. Images taken with a 10× objective.

Lung section decellularization with the standard decellularization protocol (SDC 2%) resulted in a clear DNA fluorescence signal reduction when compared to native sections (Figure 3). Images of decellularized samples showed no signs of visible cells in the tissue, while native sections showed distinct nuclei (Figure 3). Different levels of decellularization caused not only obvious differences in the DNA stained images of the tissues, but also changes in the morphology of the tissue resulting in clear changes in the PC images. In particular, with increased cellular removal, the average intensity of the PC images decreased noticeably. However, the algorithm was able to accurately perform segmentation

on samples with different levels of decellularization (Figure 2B). The method was also able to correctly reject areas corresponding to tissue damage (Figure 2B), either caused by the cryosectioning process or the decellularization, as well as to correctly segment images with a reduced number of background pixels (Figure 2B (t = 0 min)).

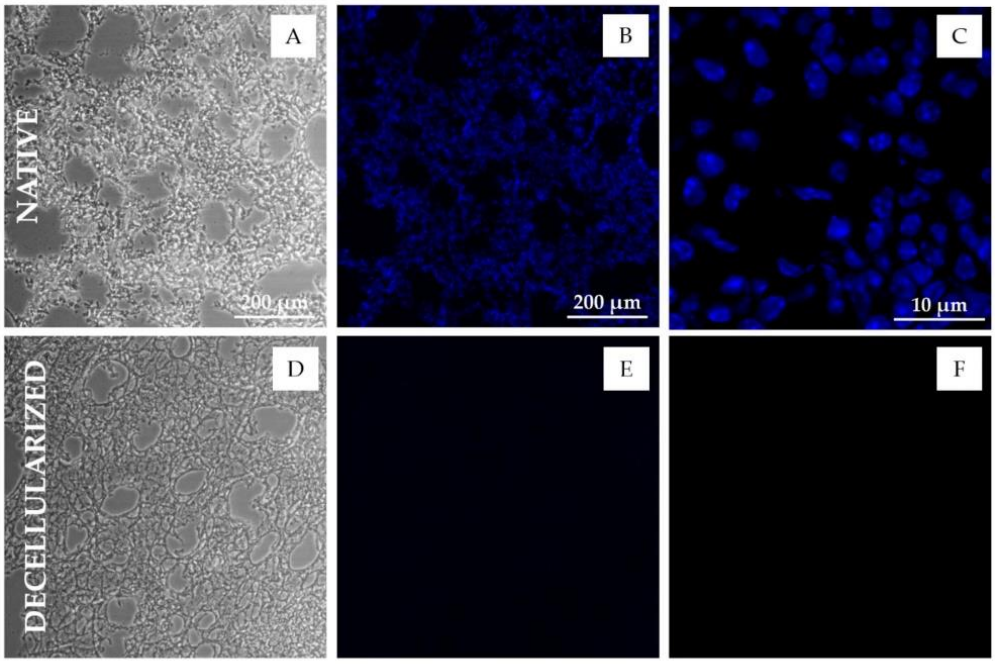

Figure 3. Microscopic images of lung tissue sections before and after decellularization. (**A**–**C**) PC image (**A**), DNA-stained fluorescent image (**B**) and confocal image (**C**) of native mice lung tissue sections (20 µm); (**D**–**F**) PC image (**D**), DNA-stained fluorescent image (**E**) and confocal image (**F**) of decellularized mice lung tissue sections (20 µm). Epifluorescent images were taken using a 10× objective. Confocal images were taken using a 60× oil immersion objective. DNA was stained by Hoechst 33342. Absence of nuclei and DNA is apparent in the decellularized sections (**E**,**F**).

As expected, decellularized lung sections had a significant reduction in DNA fluorescence intensity, displaying mean pixel fluorescence intensity values corresponding to only 5% of those displayed by native tissue. To validate the applicability of our method to tissues with a different ECM organization, we quantified samples of decellularized heart.

Of note, the same algorithm was used to segment heart section PC images without alterations and was able to produce consistent results. Similarly to lung, Median Set Fluorescence intensity (MSFI) from decellularized heart sections was only 2% of the native heart tissue MSFI (Figure 4C).

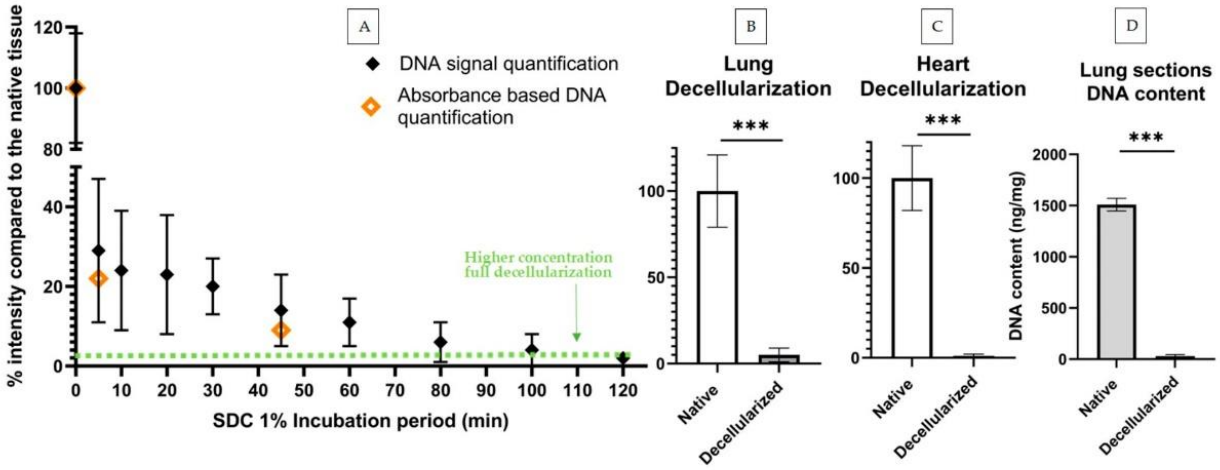

Figure 4. Lung and heart decellularization assessment via DNA signal quantification and DNA content quantification. (**A**) DNA signal quantification (n = 5, min of 8 sections per datapoint) and DNA content quantification (n = 1, a min. of 12 sections per datapoint) of decellularization protocols with increasing decellularization periods: results shown in % in comparison to the average DNA signal of the native tissue (100% intensity). Green dotted line corresponds to signal % of lung sections decellularized with standard concentration protocol (SDC 2%) (**B**) DNA signal comparison of native and decellularized lung sections (min. of 4 sections per datapoint) (**C**) and heart sections (min. 4 sections per datapoint). (**D**) DNA content of native and decellularized lung sections obtained by UV-absorbance DNA quantification (min. 12 sections per datapoint). Statistical significance between native and decellularized groups was verified using unpaired t-tests, *** indicates $p < 0.001$. DNA signal quantification of decellularization protocols with increasing decellularization periods: Results shown in % in comparison to the average DNA signal of the native tissue (100% intensity). All timepoints showed significant statistical differences ($p < 0.05$) versus native tissue (here shown as t = 0 min). A minimum of 10 image sets were taken for each lung section.

We compared the previous lung decellularization results to standard methods to quantify DNA content, in particular a DNA quantification UV absorbance kit. For this, we used 30 consecutive lung tissue sections, amounting to approximately 8 mg. Half of these sections were decellularized with the standard procedure and half were used as native controls. Following the decellularization step, tissue sections were scraped off from their substrates and pooled together in two groups (decellularized vs. native) and the DNA quantification was carried out according to the manufacturer's instructions. We found that DNA present in decellularized slices was 2% of the total DNA present in native sections, showing good agreement with our results based on image quantification (Figure 4B).

The previous results were based on leaving the decellularization agent for 30 min, as is standard protocol in our laboratory for this sample type and thickness to achieve full decellularization. Nevertheless, we hypothesized that the level of decellularization and cell removal is time-dependant and thus aimed to obtain its timeline in order to further verify our method. By decreasing the concentration of the decellularizing agent by half (from SDC 2% to 1%) and incubating the samples for different timepoints with this agent, we were able to quantify a broader range of DNA content instead of full decellularization only. Samples were incubated with SDC 1% for different time periods: 5, 10, 20, 30, 45, 60, 80, 100 and 120 min. Control samples were solely washed with phosphate-buffered saline (PBS) to remove OCT compound. To decrease biological variability, all sections for each experimental repeat had been consecutively cryosectioned from the same lung. Two consecutive sections were placed side by side in a glass slide to further decrease variability. All time points were imaged and the DNA signal quantified following our fluorescence quantification method. For validation, a reduced number of experiments was carried out using the standard UV-absorbance based method. In particular, DNA content was assessed for the decellularization protocols corresponding to timepoints t = 0, 5 and

45 min. Of note, UV-absorbance required processing together a minimum of 12–20 lung slices, depending on lung section area, (~20–30% of a mouse lung) to measure a single datapoint with minimally adequate signal-to-noise levels. We thus limited our validation to three timepoints to reduce the number of murine lungs that would have been otherwise required. As expected, the MSFI decreased with increasing SDC incubation time until it reached a plateau of 1% native intensity after the 80 min mark. The samples with the shortest incubation time already showed a significant decrease in MSFI when compared to native MSFI (Figure 4). All incubation periods produced statistically significant differences ($p < 0.05$) when compared to the untreated native samples. Standard deviation also sharply decreased with increasing SDC incubation periods, likely reflecting the homogenization of tissue as cells were increasingly eliminated from the tissue. Regarding DNA content assessed through UV-absorbance, the results from the tissues decellularized with the 5- and 45 min protocols were in line with the ones produced via signal quantification. As expected, both these protocols did not fall below the gold standard of 50 ng per mg dry weight: the 5 min protocol produced a concentration of 358 ng/mg and the 45 min protocol resulted in a concentration of 148 ng/mg.

To assess the precision and repeatability of the assays, we calculated the intra- and intersample variability of the native tissue's MSFI by computing the coefficient of variation (CoV). Native measurements were chosen for this analysis over decellularized ones because the CoV would be artifactually large in decellularized samples since their MSFI is close to zero. Consecutive lung slices (2 slices per condition) were imaged from 5 independent experiments ($n = 5$) experiments—10 total samples. DNA was quantified with the above-described algorithm. Intrasample variability was obtained by averaging the CoV's of each sample. Intersample variability was obtained by computing the CoV of the means of each sample. The results for intra- and intersample variability were very similar; 16.4% $\pm$ 9.0% and 17.9%, respectively. The similarity of these results suggests that the observed variability is mostly due to the naturally occurring biological variability of the tissue and not due to measurement or experimental error.

In a decellularization protocol, cellular removal should be performed whilst also preserving the ECM proteins and structure as much as possible. Thus, the previously described algorithm was adapted to quantify the fluorescence signal from different channels corresponding to different matrix proteins: in this case, collagen type I and elastin (Figure 5). As expected, collagen and elastin signal in the decellularized samples showed no significant differences when compared to native sections. As expected, samples that were only incubated with the secondary antibody showed low levels of signal intensity: 2% and 10% for the channels corresponding to collagen and elastin, respectively. In line with the previous results shown, DNA signal decreased significantly in decellularized samples when compared to native sections. The intrasample variability of this analysis was performed as described before. Intrasample variability of the collagen and elastin experiments were very similar to the ones obtained for the DNA signal quantification: for the elastin channel, intrasample variability was 12.0% $\pm$ 5.0% and 15.6% $\pm$ 5.0% for the collagen channel.

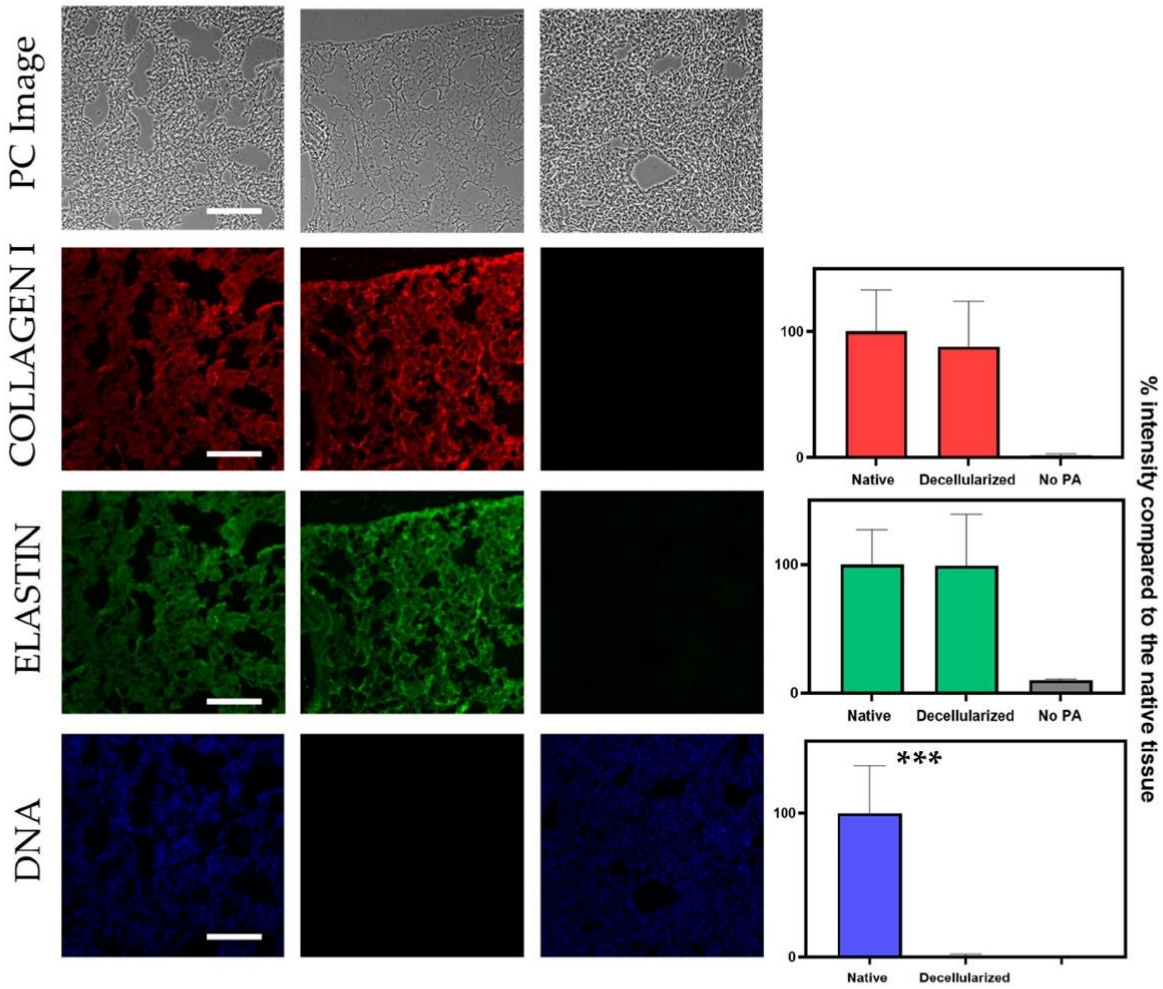

Figure 5. Simultaneous signal quantification of DNA, collagen and elastin signal based on segmentation of the corresponding PC image. The left column corresponds to a native lung section, the middle column corresponds to a decellularized lung section and the right column corresponds to a native section that was not treated with PA. Scale bar corresponds to 200 µm. The contrast of PC images has been increased for the sake of readability. Unpaired *t*-test for significance between native and decellularized groups with *p*-value *** $p < 0.001$. A minimum of 8 sections were used per datapoint.

3. Discussion

Overall, our image-based method was able to effectively mask tissue sections based on the PC images, in order to then extract the pixels of interest from the corresponding DNA stained images. The entropy-based segmentation was successful for both lung and heart decellularized tissue sections. Furthermore, the results achieved with the image-based approach were comparable to the UV-absorbance based results. As further proof of concept, we were able to track the decrease in DNA content with increasing tissue incubation periods with a decellularizing agent.

We have primarily focused our study on lung tissue and have thus taken into consideration its particular structure for some steps of the code. In particular, the lungs have different structures that need to be accounted for when performing image segmentation: alveoli, blood vessels and airways. Our code was written to include alveoli as part of the tissue and exclude the lumen of large blood vessels and airways. The reasoning for

this decision is that the alveoli's presence and size is consistent throughout lung tissue, but large blood vessels and airways are not and can influence significantly average pixel intensity.

In the future, this method could be expanded to provide additional information on the decellularization process. For example, to assess the structural integrity of the ECM, the same sample (or consecutive sections) could be imaged before and after decellularization and the free space area could be computed as a measure of tissue integrity. Additionally, by using higher resolution objectives paired with fluorescent staining, information about fibre density for native and decellularized tissue could also be obtained. Other applications include the study of ECM protein distribution, which can be especially relevant for conditions which involve the reorganization of the ECM, such as lung fibrosis [21] and lung cancer [22]. However, these additional studies were beyond the scope of this work.

Our method can also be applied to other decellularized tissues besides lung, since it is based on the natural morphological heterogeneity of the tissue, as shown by the heart decellularization dataset results. Other cell or tissue image segmentation methods are based on pixel intensity [23] but this technique could pose a challenge for thin sections such as the ones used in this work. Cryosectioning, or sectioning in general, can cause thickness variations across tissue slices that translate into different pixel intensities. Additionally, cellular removal naturally leads to a decrease in tissue density as can be seen in Figures 2, 3 and 5, which in turn leads to a decrease in intensity of the decellularized PC images. For this application, intensity-based segmentation would potentially require manual thresholding, fine tuning the upper- and lower-pixel intensity bounds for each experimental condition. By using tissue heterogeneity measured with an entropy filter, tissue thickness variation does not influence the segmentation step, allowing us to automate the thresholding steps and thus significantly decreasing the user input in the image analysis process. In addition, since this method is based on image entropy and not on directly thresholding intensity values, uneven illumination and other similar artifacts should not affect the accuracy of image segmentation. Tools such as the ones described in [15] rely on coloured images of non-fluorescent staining such as H&E. These tools offer a wide range of applications for quantitative analysis of histological sections; however, when applied to the problem of decellularization quantification, this method cannot solve the full problem since it only quantifies the number of nuclei present and not the DNA that may have been left behind by cellular lysis. Additionally, this method relies on a much more time consuming staining protocol, taking upwards of 24 h compared to the 40 min length of the nuclei-labelling protocol described previously.

The algorithm's first steps leading to image thresholding are designed to be particularly stringent, initially rejecting some pixels of interest that may be later included in the mask. The following step then groups connected pixels into aggregates so they can be labelled and sorted according to their aggregate size (i.e., number of pixels per pixel aggregate). These pixel aggregates are then filtered in or out of the mask depending on size, allowing us to select biologically relevant structures. For example, in our imaging conditions of the lung, blood vessels correspond to components of >2000 pixels while alveoli are approximately 500 pixels. For other biological tissues, or when using other magnifications, these parameters can be tuned to include or exclude from the mask certain features that are considered biologically relevant. While we used a 10× magnification objective in our imaged samples, our protocol is also suitable for higher resolution objectives equipped with phase contrast rings. However, when using higher magnifications, we would recommend a larger dataset per sample (i.e., larger number of images per slice), with a minimum of 50% of the total sample area imaged.

When comparing both DNA quantification methods, the results were similar. The DNA levels in the decellularized samples were significantly reduced in comparison to native samples and well below the 50 ng dsDNA (double stranded DNA) per mg threshold established by Crapo et al. (2011) [8]. However, not only is DNA quantification from DNA extraction more costly and requires larger amounts of tissue, but it is also more

time-consuming and typically destroys a large amount of the sample to yield only one metric. In this connection, our method is particularly convenient for samples where the full organ is not decellularized or the decellularization is carried out in thin tissue slices. For the specific decellularization protocol used in this work, we had to scrape off around 30 tissue sections from glass slides to obtain the minimal mass of dry tissue required for the DNA kit. While this approach was carried out here with the aim of validating our proposed method against an accepted gold standard, it would be difficult and time-consuming to obtain this amount of material in our experiments as routine, thus making the standard protocol for DNA quantification impractical and suboptimal. Similarly, our approach would be also best suited for clinical applications since it requires a minimal amount of biological tissue (two thin sections). For example, biopsies and other similar patient samples are typically scarce and should not be destroyed due to their uniqueness and the potential need for further characterization and testing. This new approach would thus enable easy and low-cost diagnostic applications in a clinical setting since it allows the decellularization of samples and quantitative confirmation of the procedure, followed by ECM characterization and any additional tests deemed necessary with the retained tissue.

Another major advantage of this method is that the potential multichannel image analysis allows for more than DNA content and nuclei presence assessment. In particular, it also allows researchers to gather information on the structural integrity of the matrix post decellularization, as well as its organization and composition. Other works have performed a semi-quantitative assessment of matrix proteins: for example, ECM proteins in different stages of osteogenic differentiation after decellularization were quantified using image analysis software (ImageJ and Adobe Photoshop) [14]. However, this quantification was performed with manual segmentation of areas of interest which does not allow for the analysis of large datasets or a great number of different experimental conditions, which would provide a more comprehensive understanding of the effects of the decellularization process on the ECM. For our work, we tested collagen and elastin as common ECM proteins but other matrix proteins, such as laminin and proteoglycans, could also be used. In addition, further characterization techniques could have been used such as second harmonic imaging microscopy or AFM-based mechanical testing.

Finally, most current fluorescence microscopes incorporate high degrees of automation, motorization and autofocus, thus allowing the seamless acquisition of hundreds of phase contrast + fluorescence image pairs covering the entire surface of a tissue of interest in a matter of minutes and with little human intervention. As such, our method is built into an image analysis pipeline, which allows for the accurate and unbiased analysis of dozens of stored images in minutes, even from different experimental conditions or samples. Accordingly, the combination of automated image acquisition and image quantification analysis constitutes a timely and promising new avenue for approaches that have traditionally relied on absorbance-based methods such as DNA quantification.

4. Materials and Methods

4.1. Sample Preparation and Decellularization

Lungs and hearts were harvested from adult mice, embedded in Optimum Cutting Temperature compound, OCT (Tissue-Tek, Sakura, Torrance, CA, USA) and stored at −80 °C. Samples were sectioned at 20 µm using a cryostat, with a working temperature of approximately −24 °C. Sections were deposited onto a positively charged glass slide (Superfrost; Thermo Fischer Scientific, Waltham, MA, USA) and dried for 15 min before being stored at −80 °C until further use.

Before decellularization, the edges of each slide were traced with a liquid repellent slide marker pen to keep liquid from spilling. Acellular sections were produced by consecutive washes and rinses of the sliced section while still firmly attached to a glass slide. To lyse the cells, the steps were as follows: tissue sections were twice incubated for 10 min with deionized water. Slices were then immersed in sodium deoxycholate (SDC) for a total of 30 min (2 consecutive 15 min wash). After removing the SDC with three 5 min PBS

washes, tissue sections were incubated for 20 min in DNAse I. DNase was removed with the same washes described before. Sections were decellularized at a low agitation (80 rpm) in an orbital shaker to ensure even cellular content removal throughout the sections.

DNA of cellular and acellular samples was stained by incubation with NucBlue™ Live ReadyProbes™ Reagent (Hoechst 33342, Thermo Fisher Scientific, Waltham, MA, USA) for 20 min at 80 rpm in an orbital shaker followed by three 5 min PBS washes to remove excess staining with the same agitation settings. The Nucblue staining concentration was 1 drop per 500 µL of PBS, following the manufacturer's instructions. Finally, samples were mounted in Fluoromount mounting media (Thermo Fisher Scientific) and stored at 4 °C.

4.2. Immunofluorescent and DNA Staining

For native sections, immunofluorescent staining was performed after removing OCT with consecutive washes of PBS. The tissue was fixed using 4% paraformaldehyde (PFA) for 30 min at room temperature. Samples were then blocked with 10% foetal bovine serum (FBS), and 1% bovine serum albumin (BSA) for 45 min at room temperature. Primary antibodies against elastin (goat anti-elastin, 1:50, Santa Cruz, Dallas, TX, USA) and against collagen I (rabbit anti-collagen I, 1:300, Abcam, Cambridge, MA, USA) were incubated in a solution of 10% FBS, and 1% bovine serum albumin (BSA) overnight at 4 °C at constant agitation (80 rpm). Slices were allowed to warm up at room temperature for 15 min and rinsed three times with the same type of solution. Secondary antibodies (goat anti-rabbit Alexa Fluor 647, 1:200 Thermo Fischer and donkey anti-goat, Alexa Fluor 488, 1:200, Thermo Fischer) were incubated at a 1:200 dilution in 10% FBS, and 1% BSA for 2 h, at 37 °C and constant agitation (80 rpm). Three 15 min rinses with PBS were applied to eliminate the unbound secondary antibodies. DNA of cellular and acellular samples was stained by incubation with NucBlue™ Live ReadyProbes™ Reagent with the same procedure described before. A few sections were subjected to the same protocol solely incubated with secondary antibodies to check for unspecific binding.

4.3. Experimental Setup and Protocol

Before imaging, glass slides were thoroughly cleaned with 70% ethanol and lint free tissue or lens tissue, to avoid artifacts in background detection. Epifluorescence images of the tissue sections were acquired with a Leica SP5 inverted microscope equipped with a CCD camera (C9100, Hamamatsu Photonics K.K., Hamamatsu, Japan) and using a 10× Plan Fluor objective (Nikon, Tokyo, Japan). For higher resolution images of the cell nuclei (or their absence), a Nikon D-Eclipse Ci confocal microscope was used in conjunction with a 60× Plan Apo immersion oil objective (Nikon).

Images belonging to a given treatment (decellularized slices) and corresponding control condition (native slices belonging to the same organ and animal) were acquired in a single imaging session. Exposure times for the PC and the fluorescent channels were set based on the control (native) sections corresponding to each experiment. These parameters were set by nearing pixel saturation as much as possible. In each location, PC and fluorescent images were acquired sequentially forming an image set and were saved as a single file with the file format.nd2. These image sets were 14bit 1000 × 1000 px images with 0.80 µm/px spatial resolution. Each channel was converted to 8 bit RGB .tif images by using the software NIS-Elements (Version 5.21.00, Nikon). Twenty locations per condition were chosen except when less than twenty locations were required to cover the complete slice. Slice locations that were visibly damaged were not imaged.

4.4. DNA Quantification from the PC and Fluorescence Image Pair

A custom Python image processing algorithm was developed to use PC images in order to quantify DNA presence in lung sections. This algorithm was implemented using mainly two Python libraries: skimage [24] and OpenCV [25]. In brief, the main goal was to use the PC image to identify the pixels that corresponded to tissue, thus creating masks for tissue and background. Subsequently, the masks were used to determine the fluorescence

intensity of the DNA signal images corresponding to samples treated with decellularizing agents and comparing this value with the corresponding, untreated, native tissue.

The algorithm is based on three independent steps: (1) image pre-processing, (2) image segmentation and (3) mask refinement. In the image pre-processing stage, the input dataset is separated into image sets (PC image + fluorescent images). These images are transformed from RGB to greyscale. To improve image quality and contrast, the algorithm performs a contrast stretching, or normalization (Figure 1B. This step "stretches" the range of pixel intensity values to span the full range of pixel values allowed. Additionally, the tail ends of the picture histogram (below 2% and above 98%) were clipped to further improve image contrast.

For image segmentation, corrected PC images are subjected to an entropy filter (Figure 1C). The entropy filter returns the minimum number of bits needed to encode the local pixel intensity distribution and is computed using a base 2 logarithm. The structuring element used for this filter was a circle with radius of 5 pixels. The output of this step is an image where the higher entropy regions are brighter and low entropy regions are dimmer. Areas corresponding to matrix, either native or decellularized, have higher local variations in intensity throughout the tissue and therefore display larger entropy values. Areas corresponding to the background, which has constant intensity, will display lower values of entropy. The next step is to apply a threshold to this output based on Yen's thresholding method (Figure 1D) [26]. High intensity pixels are selected and included in the mask while low intensity pixels will be excluded and dimmed as background.

The last step is mask refinement. To select which components should be included or excluded from the mask, we applied three dilations followed by four erosions (Figure 1E). For this operation, to separate components previously connected without decreasing the quality of the mask, a circular structuring element of radius three was determined to be the best approach. The number of erosions is greater than the number of dilations to combat the slight overestimation caused by the entropy filter. Each component was labelled and selected by number of pixels (Figure 1F,G). This number was chosen based on the biology of the tissue: components corresponding to large blood vessels, airways or tissue ruptures were excluded from the mask. The mask was inverted, and the same technique was applied to the background: regions caused by illumination artifacts or residue on the glass slide were thus eliminated.

The final mask is applied to the DNA signal image to obtain the pixels of interest (Figure 1H). The mask is then inverted and applied to the image again to extract the background pixels.

After selecting the pixels of interest, the mean is computed by summing the intensity of these pixels and dividing it by the number of pixels of interest. To that value, the median value of the background pixels is subtracted, as such:

$$\text{MFI} = \frac{\sum \text{intensity pixels of interest}}{\text{number of pixels of interest}} - \text{MedFBI} \quad (1)$$

where MFI is the mean DNA intensity and MedFBI is the median fluorescent background intensity, determined from the background pixels obtained by inverting the mask and applying it to the UV image.

The algorithm was written into a pipeline to be able to analyse a dataset of images at a time. This dataset corresponds to a specific condition (i.e., native, treated with decellularizing agent A, or B, etc.). The output of this algorithm is the MFI of each numbered image set and the corresponding background intensity. The median of this set of values-Median Set Fluorescence Intensity, *MSFI*-represents the fluorescence intensity corresponding to a specific treatment or condition.

To assess the decellularization level of a sample, this value is then compared to the median intensity value of the native samples of that same experiment, resulting in a final value which is a fraction of the native DNA intensity, as such:

$$\text{native fluorescence signal } \% = \frac{\text{MSFI}_{\text{decellularized}} - \text{MSFI}_{\text{native}}}{\text{MSFI}_{\text{native}}} \times 100\% \quad (2)$$

where MSFI is the median fluorescence intensity of a specific image dataset.

4.5. Multichannel Analysis

The same algorithm was adapted to quantify collagen and elastin content based on PC image masking and fluorescence signal quantification.

The process to generate a mask based on PC imaged was conducted as described before. In addition to quantifying DNA signal, the method was adjusted to also obtain information on the collagen and elastin content of both native and decellularized samples, a tool useful to not only quantify decellularization but also to assess the matrix conservation of decellularized samples. Collagen and elastin images were acquired simultaneously with UV and PC images, all corresponding to the same location.

In this specific protocol, instead of forming image pairs, the algorithm grouped images in sets of 4. When transforming the image from RGB to greyscale, different channels were selected depending on the fluorescent image: for DNA-stained images, values were taken solely from the blue channel, collagen from the red channel and elastin from the green channel. We decided on the following formula to transform RGB images to greyscale:

$$\text{Greyscale} = 0.299\text{R} + 0.587\text{G} + 0.114\text{B} \quad (3)$$

The mask generated through the PC images was then applied to the 3 fluorescence images to obtain the pixels of interest for each one. Then, the mask is inverted and applied once again to the 3 fluorescence images to obtain the background pixels. MFI of each image was computed as described before.

4.6. DNA Quantification from DNA Extraction

The kit PureLink® Genomic DNA Mini Kit (Thermo Fisher Scientific) was used to extract and quantify DNA. Briefly, this procedure digests tissue by employing Proteinase K to produce lysates which are subjected to several purifying steps. The yield of purified DNA can be estimated by UV absorbance at 260 nm using a Colibri LB 915 Microvolume Spectrophotometer (Berthold Technologies, Bad Wildbad, Germany).

To achieve enough tissue mass for the DNA quantification, native and decellularized 20 µm sections were retrieved from the glass slides by using a cell scraper and transferring the tissue onto an Eppendorf.

To compute the tissue mass, lung sections were modelled after an elliptic cylinder. The height of the cylinder was 20 µm and the cross sections were modelled as ellipses. Thus, the area of the cross sections was computed as

$$\text{A}_{\text{ellipse}} = \pi \times \text{R}_1 \times \text{R}_2 \quad (4)$$

where R_1 and R_2 are the minor and the major radii, respectively. The volume was obtained by multiplying the area of the cross sections by the section thickness (or height, h):

$$\text{V}_{\text{lung sections}} \approx \text{V}_{\text{ellipse}} = \text{A}_{\text{ellipse}} \times \text{h} \quad (5)$$

To compute the mass of each section, we used the density formula:

$$\rho_{lung} = \frac{m}{V} \quad (6)$$

where ρ is the lung density, m is the mass and V is the volume. In accordance with the work of described in [27] we considered mice lung density to be 0.3 g/cm^3. A total of 30 sections were used for cellular and acellular DNA quantification testing (15 for each condition). The lung samples tested were consecutive cryosections from the same lung.

By quantifying the DNA of both cellular and acellular lung samples, we were able to compute an approximate absolute value for DNA per mg of tissue for decellularized samples and also a relative value by comparing acellular to native tissue, which follows the same method as the image-based approach.

4.7. Statistical Analysis

All data obtained from various experiments followed a normal distribution. For experiments with 2 groups (native and decellularized) statistical comparisons were performed by an unpaired two-tailed t test. One-way analysis ANOVA with Tukey's comparison test was used to determine statistical differences between the different groups subjected to different incubation periods compared to the untreated samples. All data are mean ± SD. Differences were considered statistically significant for $p < 0.05$. Statistical analysis was performed using GraphPad Prism (GraphPad software 9.1.0, Inc., San Diego, CA, USA).

Intra- and intersample variability were computed using the coefficient of variation (CoV), as follows:

$$CoV = \frac{\sigma}{\mu} \tag{7}$$

where σ is the standard deviation and μ is the mean.

Author Contributions: Conceptualization, M.N., I.A. and N.G.; Formal analysis, M.N. and N.G.; Funding acquisition, D.N. and R.F.; Investigation, M.N.; Methodology, M.N., J.O., I.A. and N.G.; Project administration, D.N., R.F., I.A. and N.G.; Resources, J.O., D.N., R.F. and I.A.; Software, M.N.; Supervision, I.A. and N.G.; Writing of original draft, M.N. and N.G. All authors have read and agreed to the published version of the manuscript.

Funding: This research was partially funded by Ministerio de Ciencia e Innovación (PID2019-108958RB-I00/AEI/10.13039/501100011033) and SEPAR (900-2019). M.N. was funded by the H2020 European Research and Innovation Programme under the Marie Skłodowska-Curie grant agreement "Phys2BioMed" contract no. 812772. R.F. and J.O. were funded by the Spanish Ministry of Sciences, Innovation and Universities, SAF2017-85574-R and PGC2018-097323-A-I00, respectively.

Institutional Review Board Statement: The study was conducted according to the guidelines of the Declaration of Helsinki, and approved by the Ethics Committee of the University of Barcelona (protocol code 10972, approved on 17 February 2020).

Informed Consent Statement: Not applicable.

Data Availability Statement: The code developed for segmentation of phase contrast images will be made available at Github.

Conflicts of Interest: The authors declare no conflict of interest.

References

1. Mendibil, U.; Ruiz-Hernandez, R.; Retegi-Carrion, S.; Garcia-Urquia, N.; Olalde-Graells, B.; Abarrategi, A. Tissue-Specific Decellularization Methods: Rationale and Strategies to Achieve Regenerative Compounds. *Int. J. Mol. Sci.* **2020**, *21*, 5447. [CrossRef] [PubMed]
2. Hoshiba, T.; Lu, H.; Kawazoe, N.; Chen, G. Decellularized Matrices for Tissue Engineering. *Expert Opin. Biol. Ther.* **2010**, *10*, 1717–1728. [CrossRef]
3. Gilpin, A.; Yang, Y. Decellularization Strategies for Regenerative Medicine: From Processing Techniques to Applications. *BioMed Res. Int.* **2017**, *2017*, 9831534. [CrossRef] [PubMed]
4. Lü, W.-D.; Zhang, L.; Wu, C.-L.; Liu, Z.-G.; Lei, G.-Y.; Liu, J.; Gao, W.; Hu, Y.-R. Development of an Acellular Tumor Extracellular Matrix as a Three-Dimensional Scaffold for Tumor Engineering. *PLoS ONE* **2014**, *9*, e103672. [CrossRef] [PubMed]
5. Xiong, G.; Flynn, T.J.; Chen, J.; Trinkle, C.; Xu, R. Development of an Ex Vivo Breast Cancer Lung Colonization Model Utilizing a Decellularized Lung Matrix. *Integr. Biol.* **2015**, *7*, 1518–1525. [CrossRef]

6. Shojaie, S.; Ermini, L.; Ackerley, C.; Wang, J.; Chin, S.; Yeganeh, B.; Bilodeau, M.; Sambi, M.; Rogers, I.; Rossant, J.; et al. Acellular Lung Scaffolds Direct Differentiation of Endoderm to Functional Airway Epithelial Cells: Requirement of Matrix-Bound HS Proteoglycans. *Stem Cell Rep.* **2015**, *4*, 419–430. [CrossRef]
7. O'Neill, J.D.; Anfang, R.; Anandappa, A.; Costa, J.; Javidfar, J.; Wobma, H.M.; Singh, G.; Freytes, D.O.; Bacchetta, M.D.; Sonett, J.R.; et al. Decellularization of Human and Porcine Lung Tissues for Pulmonary Tissue Engineering. *Ann. Thorac. Surg.* **2013**, *96*, 1046–1056. [CrossRef]
8. Crapo, P.M.; Gilbert, T.W.; Badylak, S.F. An Overview of Tissue and Whole Organ Decellularization Processes. *Biomaterials* **2011**, *32*, 3233–3243. [CrossRef]
9. Kang, H.-K.; Kim, K.-H.; Ahn, J.-S.; Kim, H.-B.; Yi, J.-H.; Kim, H.-S. A Simple Segmentation and Quantification Method for Numerical Quantitative Analysis of Cells and Tissues. *Technol. Health Care* **2020**, *28*, 401–410. [CrossRef]
10. Hsieh, D.-J.; Srinivasan, P.; Yen, K.-C.; Yeh, Y.-C.; Chen, Y.-J.; Wang, H.-C.; Tarng, Y.-W. Protocols for the Preparation and Characterization of Decellularized Tissue and Organ Scaffolds for Tissue Engineering. *BioTechniques* **2021**, *70*, 107–115. [CrossRef] [PubMed]
11. Alshaikh, A.B.; Padma, A.M.; Dehlin, M.; Akouri, R.; Song, M.J.; Brännström, M.; Hellström, M. Decellularization and Recellularization of the Ovary for Bioengineering Applications; Studies in the Mouse. *Reprod. Biol. Endocrinol.* **2020**, *18*, 75. [CrossRef] [PubMed]
12. Fischer, I.; Westphal, M.; Rossbach, B.; Bethke, N.; Hariharan, K.; Ullah, I.; Reinke, P.; Kurtz, A.; Stachelscheid, H. Comparative Characterization of Decellularized Renal Scaffolds for Tissue Engineering. *Biomed. Mater.* **2017**, *12*, 045005. [CrossRef]
13. Nonaka, P.N.; Campillo, N.; Uriarte, J.J.; Garreta, E.; Melo, E.; de Oliveira, L.V.F.; Navajas, D.; Farré, R. Effects of Freezing/Thawing on the Mechanical Properties of Decellularized Lungs: Decellularized Lung Mechanics after Freezing/Thawing. *J. Biomed. Mater. Res. A* **2014**, *102*, 413–419. [CrossRef]
14. Hoshiba, T.; Kawazoe, N.; Tateishi, T.; Chen, G. Development of Stepwise Osteogenesis-Mimicking Matrices for the Regulation of Mesenchymal Stem Cell Functions. *J. Biol. Chem.* **2009**, *284*, 31164–31173. [CrossRef]
15. Magliaro, C.; Tirella, A.; Mattei, G.; Pirone, A.; Ahluwalia, A. HisTOOLogy: An Open-Source Tool for Quantitative Analysis of Histological Sections. *J. Microsc.* **2015**, *260*, 260–267. [CrossRef]
16. Biltz, N.K.; Meyer, G.A. A Novel Method for the Quantification of Fatty Infiltration in Skeletal Muscle. *Skelet. Muscle* **2017**, *7*, 1–13. [CrossRef]
17. Cortiella, J.; Niles, J.; Cantu, A.; Brettler, A.; Pham, A.; Vargas, G.; Winston, S.; Wang, J.; Walls, S.; Nichols, J.E. Influence of Acellular Natural Lung Matrix on Murine Embryonic Stem Cell Differentiation and Tissue Formation. *Tissue Eng. Part A* **2010**, *16*, 2565–2580. [CrossRef]
18. Luque, T.; Melo, E.; Garreta, E.; Cortiella, J.; Nichols, J.; Farré, R.; Navajas, D. Local Micromechanical Properties of Decellularized Lung Scaffolds Measured with Atomic Force Microscopy. *Acta Biomater.* **2013**, *9*, 6852–6859. [CrossRef]
19. Salvi, M.; Morbiducci, U.; Amadeo, F.; Santoro, R.; Angelini, F.; Chimenti, I.; Massai, D.; Messina, E.; Giacomello, A.; Pesce, M.; et al. Automated Segmentation of Fluorescence Microscopy Images for 3D Cell Detection in Human-Derived Cardiospheres. *Sci. Rep.* **2019**, *9*, 6644. [CrossRef] [PubMed]
20. Paulik, R.; Micsik, T.; Kiszler, G.; Kaszál, P.; Székely, J.; Paulik, N.; Várhalmi, E.; Prémusz, V.; Krenács, T.; Molnár, B. An Optimized Image Analysis Algorithm for Detecting Nuclear Signals in Digital Whole Slides for Histopathology: Whole Slide Nucleus Detection Algorithm. *Cytometry A* **2017**, *91*, 595–608. [CrossRef] [PubMed]
21. Elowsson Rendin, L.; Löfdahl, A.; Åhrman, E.; Müller, C.; Notermans, T.; Michaliková, B.; Rosmark, O.; Zhou, X.-H.; Dellgren, G.; Silverborn, M.; et al. Matrisome Properties of Scaffolds Direct Fibroblasts in Idiopathic Pulmonary Fibrosis. *Int. J. Mol. Sci.* **2019**, *20*, 4013. [CrossRef] [PubMed]
22. Malandrino, A.; Mak, M.; Kamm, R.D.; Moeendarbary, E. Complex Mechanics of the Heterogeneous Extracellular Matrix in Cancer. *Extrem. Mech. Lett.* **2018**, *21*, 25–34. [CrossRef] [PubMed]
23. Dewan, M.A.A.; Ahmad, M.O.; Swamy, M.N.S. A Method for Automatic Segmentation of Nuclei in Phase-Contrast Images Based on Intensity, Convexity and Texture. *IEEE Trans. Biomed. Circuits Syst.* **2014**, *8*, 716–728. [CrossRef] [PubMed]
24. Van der Walt, S.; Schönberger, J.L.; Nunez-Iglesias, J.; Boulogne, F.; Warner, J.D.; Yager, N.; Gouillart, E.; Yu, T. Scikit-Image: Image Processing in Python. *PeerJ* **2014**, *2*, e453. [CrossRef]
25. Bradski, G.; Kaehler, A. The OpenCV Library. *Dr Dobb's J. Softw. Tools* **2000**, *25*, 120–125.
26. Chang, F.-J.; Yen, J.-C.; Chang, S. A New Criterion for Automatic Multilevel Thresholding. *IEEE Trans. Image Process.* **1995**, *4*, 370–378. [CrossRef]
27. Boutaleb, S.; Pouget, J.-P.; Hindorf, C.; Pelegrin, A.; Barbet, J.; Kotzki, P.-O.; Bardies, M. Impact of Mouse Model on Preclinical Dosimetry in Targeted Radionuclide Therapy. *Proc. IEEE* **2009**, *97*, 2076–2085. [CrossRef]

Scientific Article IV:

“Lung Micrometastases Display ECM Depletion and Softening While Macrometastases Are 30-Fold Stiffer and Enriched in Fibronectin”

This article is to be submitted for review in November 2022 to fulfil the specific objectives (3) and (4), “To correlate mechanical properties, molecular composition and structure of extracellular matrix of normal and cancer lung tissues of different origins and throughout different stages of tumor progression” and “To assess the changes in the lung tumor extracellular matrix in response to nintedanib treatment”, respectively. It is based on the methodology and findings previously described in Scientific Article I, II and III.

LUNG MICROMETASTASES DISPLAY ECM DEPLETION AND SOFTENING WHILE MACROMETASTASES ARE 30-FOLD STIFFER AND ENRICHED IN FIBRONECTIN

Maria Narciso, Africa Martinez, Constança Júnior, Massimiliano Berardi, Natalia Diaz-Valdivia, Anna Uldemolins, Kate Neal, Daniel Navajas, Ramon Farre, Jordi Alcaraz, Isaac Almendros* and Núria Gavara*

[1]Unitat de Biofísica i Bioenginyeria, Facultat de Medicina i Ciències de la Salut, Universitat de Barcelona, Barcelona, Spain;
[2]The Institute for Bioengineering of Catalonia (IBEC), The Barcelona Institute of Science and Technology, Barcelona, Spain
[3]CIBER de Enfermedades Respiratorias, Madrid Spain
[4]Institut d'Investigacions Biomèdiques August Pi i Sunyer, Barcelona, Spain

* Correspondence: isaac.almendros@ub.edu and ngavara@ub.edu

Abstract:

Mechanical changes in the tumor microenvironment (TME) have long been associated with an increase in malignancy, metastatic invasion, and therapy resistance. Within the TME lies extracellular matrix (ECM) which also plays an important role in tumor progression and invasion. Changes in cancer tissue mechanics have often been attributed to mechanical changes in the tumor ECM, but until now, no mechanical studies have been carried out in decellularized tumor tissue. Here, we aimed to study the biochemical and mechanical progression of the tumor ECM in two models of metastases to the lungs: an endogenous source (Lewis lung carcinoma, LLC1) and an exogeneous one (melanoma, B16F10). To achieve this, we decellularized the resulting lung cryosections with metastases and used Atomic Force Microscopy (AFM) to measure the micromechanics of the tumor ECM. Healthy and lung tumor sections were stained for collagen I and IV, laminin, fibronectin as well as proliferation and cell death markers, and their content was assessed by fluorescent image quantification. The same study was extended to a group of mice with melanoma metastasis in the lungs which were treated with the anti-fibrotic drug Nintedanib to study its effects on the tumor ECM. Both lung carcinoma (CAR) and melanoma (MEL) lung tumors produced a highly dense and stiff ECM, averaging 1.79±1.32 kPa for CAR and 6.39±3.37 kPa for MEL when compared to healthy lung ECM (~0.40 kPa). This study identified fibronectin as a key player in tumor ECM, being overexpressed from early invasion stages (~118% of fibronectin in healthy ECM) to fully developed macrometastases (~260% of fibronectin in healthy ECM) in both lung carcinoma and melanoma models. Surprisingly, nintedanib caused a 4-fold increase in ECM deposition (from 5.1±1.6% to 18.6±8.9% tumor area) and a 2-fold increase in ECM stiffness (from 6.39±3.37kPa to 12.35±5.74kPa). This increase in stiffness strongly and positively correlated with an increase in tumor necrosis, which reveals a link between tumor hypoxia and tumor ECM deposition and stiffness. Our findings thus highlight fibronectin and tumor ECM mechanics as attractive targets in lung cancer therapy.

Keywords: Lung Metastases, Melanoma, Lung Carcinoma, Extracellular Matrix, Decellularization, Atomic Force Microscopy, stiffness, fibronectin, collagen, basement membrane, microrheology, viscoelasticity, angiogenesis, Nintedanib

INTRODUCTION

The extracellular matrix (ECM) is the three-dimensional network of macromolecules that provides structural and biochemical support to the cells embedded in it. Cells continuously interact with the ECM and also rearrange, produce and break down ECM components during cellular physiological processes. During tumor development, the ECM suffers complex structural changes, influencing or even facilitating its progression, *e.g.* during invasion and metastasis formation (1–4). In solid tumors, the increased deposition of ECM components, a phenomenon known as desmoplasia, has been strongly linked to poor prognosis (5,6). This increased deposition has been commonly linked to collagen I (7–9) but can consist of other proteins such as elastin, hyaluronic acid, tenascin C, fibronectin, and laminin (10–12). The presence (or absence) of certain ECM components has associated differences in tumor development and progression. In fact, inhibition of fibronectin in human breast cancer cells led to a suppression of cancer growth in a metastatic mouse model (13). In addition to biochemical modifications, structural rearrangements of the tumour microenvironment can influence cancer cell behaviour as well, as seen in breast cancer matrices (14). In the tumor's stroma, cancer-associated fibroblasts (CAF's) remodel tumor ECM and reorient collagen fibres perpendicularly to the tumor boundary, facilitating breast cancer cell invasion into the neighbouring tissues (14–16). Clinical cases where this collagen realignment has been detected were linked to a poorer prognosis and reduced therapeutic success (16).

This influence between cells and ECM is exerted by more than just the microenvironment's components as changes in the mechanics of the ECM provide different physical stimuli to embedded cells that significantly impact their development. Studies have determined that the stiffness of the ECM drives cell's normal differentiation, migration, proliferation (17) but also that aberrant ECM stiffness is associated to disease, such in pulmonary fibrosis (18) and malignancy (19–21). For instance, it has been found that lysyl oxidase (LOX), which is an enzyme that crosslinks collagen and elastin, is overexpressed in many cancer tissues, like gastric, colorectal and breast cancer (22,23). This overexpression increases tissue stiffness and promotes cancer invasion and progression (24). Furthermore, stiffening of the cancer tissue, attributed to an increase in ECM stiffening, has been linked to therapy resistance in pancreatic and hepatic cancer (7). Additionally, several studies have shown that increasing matrix stiffness drives epithelial-to-mesenchymal transition (EMT) in breast and pancreatic cancer (7,25) which lead to an overall increase in invasive behaviour (26). Finally, the stiffness of the matrix determines the levels of autophagy in smooth muscle cells, where stiffer substrates led to higher levels of autophagy (27), a phenomenon often associated with resistance to treatment in cancer (28,29). It is thus clear that changes in ECM mechanics, namely its stiffening, lead to a variety of tumor cell responses linked to malignancy and drug resistance.

Previous studies on a variety of cancers highlight an interesting contradiction, which is that isolated cancer cells are softer than benign cells (30,31) but tumor samples (that is, the native tissue composed of cells and ECM) are found to be stiffer and more heterogeneous than healthy tissue (30,32,33). This disparity stresses the need to study ECM separately from cells, to assess its changes in the progression of malignancy. Indeed, the lack of studies on the mechanics of decellularized tumor has prevented the correlative assessment of tumor ECM stiffness with other tumor features, like size, the deposition of specific ECM components or the presence of necrosis. Furthermore, understanding ECM compositional and mechanical changes throughout each step of cancer progression will be useful to better understand this process and for the development of targeted treatments. Of note, there is evidence that different ECM components play different roles at various tumor developmental stages. For example, even though collagen is seemingly the primary component in the advanced tumor microenvironment, fibronectin is believed to play a

key role in the formation of the pre-metastatic niche in pancreatic cancer (34). There is a clear need to identify and study changes in ECM composition and mechanics at different stages of tumor progression, which ultimately influence tumor progression and treatment resistance.

Here, we focus on lung tumors, more specifically lung-seeking metastases since the lung is the second most common site for metastatic cancer (35). Furthermore, the mechanical features of the cell microenvironment are especially important since the pulmonary ECM is continuously subjected to cyclic stretching due to breathing. Our aim was to characterize ECM progression of metastases in the lung of mice, both from an endogenous source (Lewis lung carcinoma) and an exogeneous one (melanoma). Additionally, we treated a group of mice with melanoma metastasis in the lungs with an anti-fibrotic drug (nintedanib) to study its effects on the tumor ECM. The resulting tumors were decellularized and analysed mechanically and compositionally and these features were correlated with tumor size, the presence of necrosis and proliferation. We used this approach to show that the tumor is associated with a highly dense and stiff ECM, both in melanoma and lung carcinoma metastasis and identify fibronectin as the key player in the tumor ECM, from the early to the late stages of tumor development.

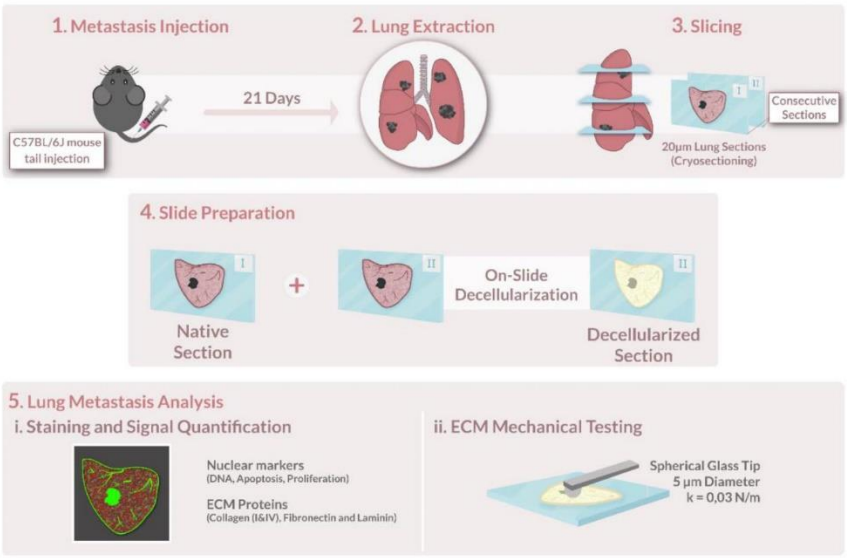

Figure 1 - Schematic representation of the methodology followed in this work.

RESULTS

To study how metastasis from different origins - endogenous (lung) and exogeneous (melanoma) - affect and remodel the lung ECM, we employed two well-established lung-seeking metastasis models (36,37) (lung carcinoma, LCC1 and melanoma, B16-F10) where metastatic mice cell lines are injected through the tail vein of mice and metastasize to the lungs. Twenty-one days after injection, the lungs were harvested, embedded in optimum cutting temperature compound (O.C.T) and stored at -80ºC for later cryosectioning at 20 µm. Lungs were not manipulated to remove metastasis from them, so each cryosection contained both healthy lung ECM and tumorous ECM. This method was chosen since it resembles clinical conditions where the control

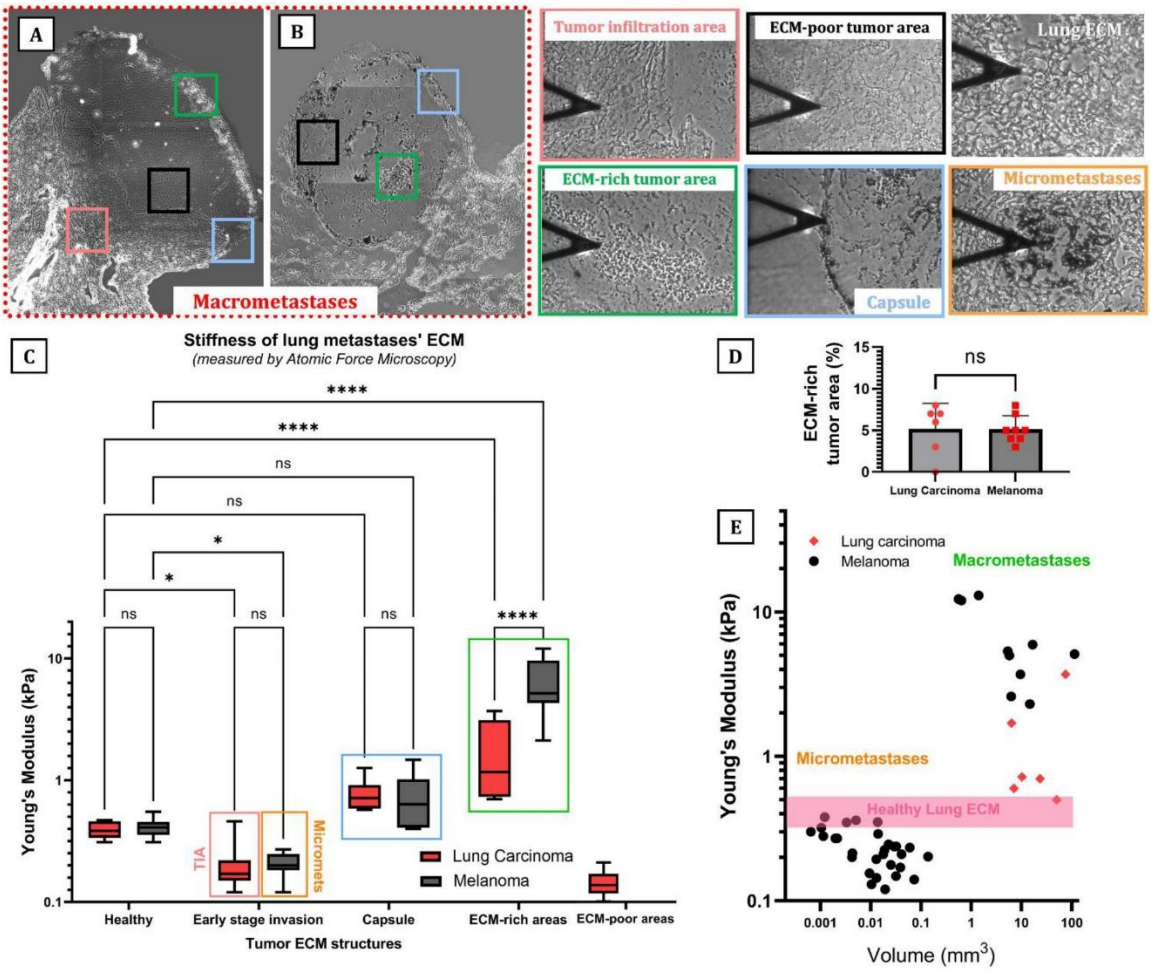

Figure 2 – Structure and mechanics of the decellularized ECM of lung carcinoma (LC) and melanoma (MEL) lung metastases. (A) Lung carcinoma decellularized metastases (B) Decellularized melanoma lung metastases. (C) Young's modulus (kPa) of each ECM structure of LC and MEL metastases, measured by atomic force microscopy. (D) ECM deposition measured by the area tumor area occupied by the ECM-rich areas, where the total tumor area was normalized to 100%. (E) Relationship between Young's modulus (kPa) and estimated volume (mm^3) of metastases. P-values obtained using a two-way analysis of variance (ANOVA) with a Tukey post-doc multiple comparisons. (*, p-value <0.05, **, p-value < 0.01, ***, p-value < 0.001, ****, p<0.0001).

tissue ("healthy tissue") is taken from the biopsy of an adjacent area of the lung. To assess the lung and tumor ECM after the metastatic process, samples were attached to a glass slide after cryosectioning and decellularized through consecutive washes and rinses of ultrapure water, sodium deoxycholate (SD), deoxyribonuclease I solution and PBS, without detaching from the glass slide, thus preserving the tumor's internal structure. A summary of the followed methodology can be found in Figure 1.

a. Distinct ECM structures are present throughout tumor development

The two tumor models produced macroscopically very distinct tumors: Lung carcinoma (CAR) metastases were rigid and colourless while lung melanoma (MEL) metastases were viscous and

black, due to the melanin produced by the cancer cells. After decellularization, several ECM structures were very clearly distinguishable microscopically (**Figure 2A-B)**. We subdivided metastases into two categories based on size and structure: micro- and macrometastasis. Most macrometastasis were surrounded by a thicker layer of ECM – which we will refer to as the capsule. In melanoma macrometastasis, the tumor was strictly confined within the borders of the capsules. In CAR metastasis, capsules were thinner and at times non-existent. For that reason, CAR tumors often infiltrated the surrounding healthy tissue, and the ECM slowly transitions from tumor ECM to "healthy" ECM - we call these transition regions, "tumor infiltration areas" (TIA) - with no clear separation of the two, a phenomenon that was not present in melanoma metastasis.

Within the tumor boundaries, tumor ECM had two distinct presentations: ECM-poor areas, where cancer cells had been previously predominantly located, and ECM-rich areas, which are areas of densely packed ECM, which displayed a grape-like structure. In CAR tumors the ECM-poor areas are composed of a low-density meshwork of ECM proteins that covers most of the tumor area, transitions into the "tumor infiltration areas" and finally to healthy lung ECM (Figure 2A). The ECM-rich regions of CAR tumors are located in the periphery and in the same location of the capsule (at times replacing it completely). This ECM distribution seen in lung carcinoma metastasis highly contrasts with the ECM of melanoma metastasis. Here, the ECM-poor areas within the capsule are mostly bare, with little to no ECM (Figure 2B) while the ECM-rich regions are more centrally located. Micrometastasis were only present in lungs of the melanoma metastases' model and its ECM consists of what appears to be disorganized lung ECM, while the alveoli and blood vessels of the pre-metastatic site can at times still be visible.

To assess the amount of ECM deposition within the tumor, we computed the percentage of ECM-rich areas as follows: in acellular tumors, the ECM-rich regions were traced and then compared to the total tumor area, which was normalized to 100%. Even though they were located in different areas of the tumor, the percentage of ECM-rich areas in both CAR and MEL macrometastases was nearly identical (**Figure 2**D, 5.2±3.1% and 5.2±1.6%, respectively) which suggests that ECM production of the tumor does not depend on the tumor primary site.

b. The tumor ECM is up to 15 times stiffer than healthy lung ECM

Given that the tumor ECM structures were so distinctly different at the microscale, we hypothesised that they would also have different micromechanical properties. To that effect, we next sought to measure their stiffness by means of Atomic Force Microscopy (AFM) which allows for microscale resolution when measuring the Young's modulus (E) of each structure. AFM measurements were performed immediately after decellularization, with the samples submerged in PBS, at room temperature (RT) while attached to a glass slide.

A two-way ANOVA revealed that there was a statistically significant interaction between the type of metastasis and the tumor ECM structure ($p<0.0001$). Also, both the type of metastasis and the type of ECM structure have a statistically significant effect on the ECM stiffness ($p = 0.0026$ and $p<0.0001$, respectively). As expected, the mean young's modulus (E_m) of the "healthy" lung ECM of mice injected with lung carcinoma and melanoma cells was nearly identical (0.39±0.06 and 0.41±0.07 kPa, respectively, $p>0.9999$). However, when compared with healthy ECM, the ECM of melanoma micrometastases showed a significant decrease in E_m (0.21±0.05kPa, $p=0.0176$) which correlates with their visual presentation of a degraded lung ECM. The TIA of lung carcinoma metastases showed an identical decrease in stiffness (0.21±0.11kPa, $p=0.0359$) when compared with melanoma micrometastasis ($p>0.9999$). Even though MEL metastatic cells travel to a new location while CAR invades the surrounding tissue, their identical ECM softening and similar visual presentations (i.e. overall lung ECM degradation) suggests that the early stages in

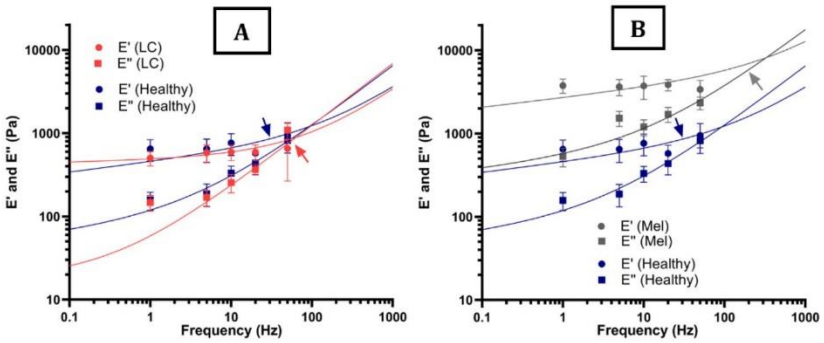

C

		A (kPa)	α	B(kPa)	f_t (Hz)
$\beta = 3/4$	*Healthy ECM*	452.4± 204.5	0.118± 0.127	38.3± 21.3	*49.7*
	Lung Carcinoma	475.2± 21.60	0.0267± 0.0305	41.7± 10.0	*29.0*
	Melanoma	2714 ± 759.3	0.114 ±0.0768	101 ±64.1	*176*

Figure 3 – Frequency dependent loss (E') and storage (E") modulus as measured by dynamic mechanical analysis (DMA) of the ECM of healthy lung and the ECM-rich regions of (A) - lung carcinoma (CAR) and (B) - melanoma (MEL) lung macrometastasis. Solid lines represent the fits of two-power law model. Arrows indicate the transition frequency. Fit parameters and transition frequency are detailed in table C.

tumor progression of both models have a common underlying mechanism for both endogenous and exogenous metastasis in the initial tumor invasion and progression stages.

Even though the ECM capsules of both models had different visual presentations, the structures in both tumor types had similar microscale stiffnesses and were significantly stiffer than healthy lung ECM (0.78±0.25 for CAR, p = 0.0763 and 0.75±0.41 for MEL, p = 0.3080). This similarity once again suggests a similar underlying mechanism when encapsulating the tumor, disregarding its cellular origin. Surprisingly, the ECM-rich regions of both models were more than 5- and 15- fold stiffer than healthy ECM (1.79±1.32kPa for CAR and 6.39±3.37kPa for MEL, both p<0.0001), a stark increase when compared to the softening measured in earlier tumor stages which, in addition to its visual appearance, suggest this ECM is being newly produced by the tumor. However, the different stiffnesses and locations of the ECM-rich regions in CAR and MEL also suggest different underlying mechanisms for ECM production within the tumor. Lastly, the ECM-poor regions of the CAR metastasis were significantly softer than the healthy lung (0.15±0.04kPa, student t-test, p=0.0140), while the same regions in MEL metastasis were not measured due to lack of ECM.

c. ECM stiffness decreases with tumor size in micro- and macrometastasis

Taking into consideration the visual presentation and stiffness of the ECM structures, we hypothesized that their appearance and mechanical properties likely reflect a timeline of tumor progression. With that in mind, we sought to correlate the stiffness of each tumor ECM to its volume (**Figure 2E**), using tumor volume as a surrogate of development time. To achieve this, tumor volume was estimated based on the formula: $Volume = \frac{1}{2}(length \cdot width^2)$. Measurements of the length and width were performed using ImageJ and using both photographs and microscopic images of the tumors.

Regarding MEL metastasis development, the stiffness of smaller micrometastasis is within the

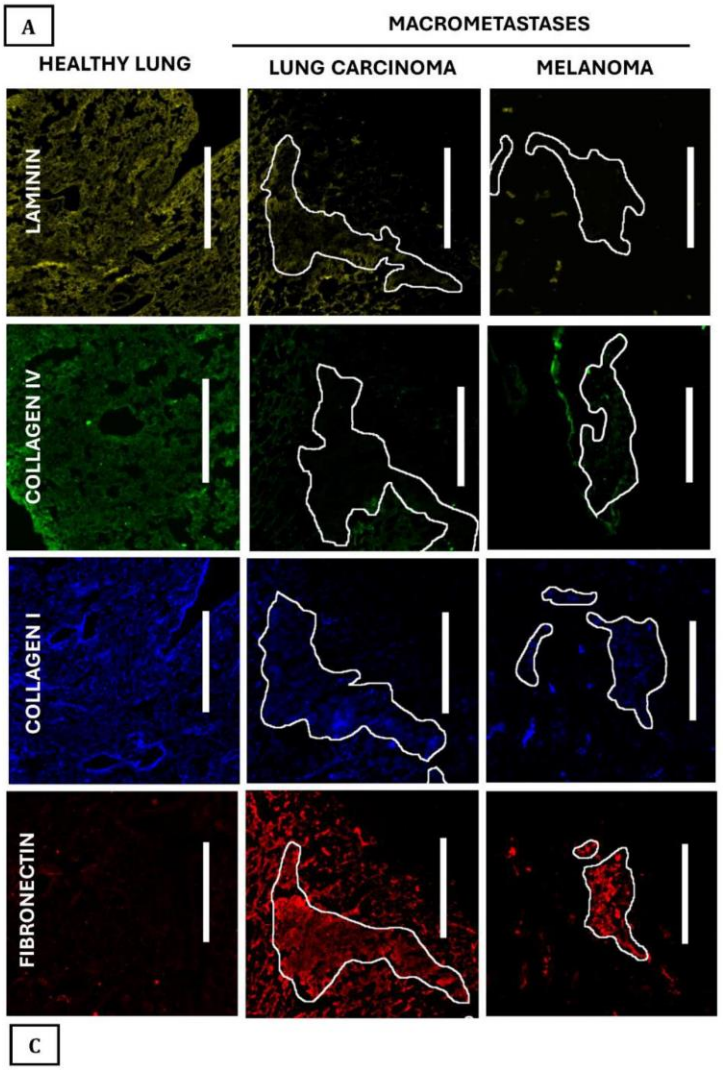

C

ECM proteins	Laminin		Collagen IV		Collagen I		Fibronectin	
	%tLAM	%rLAM	%tC4	%rC4	%tC1	%rC1	%tFIB	%rFIB
Lung carcinoma	52±5.9	47.6±19.0	64.1±11.7	46.3±11.8	69.6±9.0	92.4±44.0	152.9±34.3	267.8±55.3
Melanoma	23.3±10.3	27.1±16.0	36.5±14.4	49.2±13.8	60.0±18.5	115.2±30.4	88.0±23.9	249.2±85.0

Figure 4 – ECM protein staining and quantification of CAR and MEL macrometastases. (A) - Representative fluorescent images of acellular tumor sections (20µm) after immunostaining of laminin (yellow), collagen IV (green), collagen I (blue) and fibronectin (red). Healthy lung ECM is represented in the left column. ECM-rich areas (%r, white selections) were traced using a phase contrast image and then applied to the corresponding fluorescent image. (B, C) – ECM proteins' fluorescent signal quantification of the total tumor (%t) and tumor ECM-rich areas (%r). Healthy lung ECM signal was normalized to 100% (green line). Statistical analysis was performed using unpaired parametric student's t-tests (**, p-value < 0.01, ***, p-value < 0.001). If nothing else is indicated, the relationship between two variables was found to be insignificant (*p>0.05*). Scale bar = 500 µm.

healthy ECM range (approximately 0.3 to 0.5 kPa) and, as they grow, the ECM becomes progressively softer, indicating a degradation of the metastatic niche. At around 0.5 mm^3, micrometastasis become encapsulated, develop an ECM-rich region and become macrometastasis. Surprisingly, this ECM-rich region also progressively decreases in stiffness with increasing tumor volume. In CAR metastasis, there isn't a clear relationship between tumor volume and ECM stiffness.

d. Lung carcinoma has similar viscoelasticity to healthy ECM, while melanoma lung metastasis differs

Most soft tissues in the body are not purely elastic and also have viscoelastic features which are important for their function. For that reason, to further characterize the lung metastases' ECM, more specifically its ECM-rich regions, we next set out to assess their viscoelastic behaviour. Broadly, we used Dynamic Mechanical Analysis (DMA) to measure the ECM's response to different probing frequencies. Even though the CAR stiffness values had been considerably higher than healthy ECM, the values for storage modulus E' and loss modulus E'' were practically identical (Figure 3A), where the storage modulus accounts for the stored elastic energy, while the loss modulus accounts for the dissipated energy. However, E' and E'' of MEL metastasis were an order of magnitude higher than in healthy lung ECM (**Figure 3B**), suggesting a sharp stiffening of the ECM, consistent with the AFM results.

This data was then fitted to a two-power law model in accordance to previously published works (18,38). The coefficients A and B in this model can be interpreted as an index of stiffness at the low- and high- frequencies, respectively. Once again, these coefficients were similar in healthy lung ECM and ECM-rich regions of CAR metastasis.

The ECM transition frequency (f_t) is the frequency at which the ECM transitions from a behaviour closer to a solid to a more liquid behaviour. This transition frequency was also similar in healthy lung ECM and CAR metastasis' ECM (49.7 and 29.0Hz, respectively) but was 4 times higher in melanoma metastasis (176Hz). The α index of the power-law exponent is again related to the solid vs liquid behaviour of the sample, where a pure solid behavior is in the limit of a α = 0 and fluidlike features for a α=1. The α exponent is closer to 0 for the structures analysed (α=0.114and 0.118, for healthy and MEL ECM, respectively), with a slight decrease of CAR ECM-rich regions (α=0.027), indicating a more solid-like behaviour in CAR tumor ECM a and more fluid-like behaviour in MEL tumor ECM, which is consistent with the tumors macroscopic presentation as well.

Together, these DMA measurements and the young's modulus results measured by AFM suggest that most of the measured mechanical features of exogeneous metastasis (in this case, melanoma) greatly differ from its surrounding lung environment, while endogenous metastasis (lung carcinoma) have more compatible features with its initial metastatic niche.

e. Macrometastasis ECM is rich in densely packed fibronectin but has a depleted basement membrane

After establishing a mechanical stiffening of the ECM in both endogenous and exogenous metastasis, we assumed that the tumor was producing copious amounts of new ECM. To confirm this hypothesis, we decided to stain and quantify the presence of four ECM proteins that had established links to tumor development: two proteins from the interstitial ECM (collagen I and fibronectin) and two proteins from the basement membrane (collagen IV and laminin). To

quantify them, we used immunostaining to label each protein followed by fluorescence imaging (see representative images in Figure 4.B.1). To establish a baseline, the intensity of 5-10 random locations in the healthy ECM was measured and averaged, and this mean value was set to 100%. Tumor ECM proteins were quantified in two different areas: the total tumor area (%t_) and the ECM-rich areas (%r_). ECM-rich areas were quantified by tracing them in the phase contrast image, creating a mask and applying that mask to the corresponding fluorescence image of a given protein (see white selections in **Figure 4**A), while total tumor areas were quantified by tracing the entirety of the tumor. Overall, the basement membrane proteins, laminin and collagen IV, were significantly reduced in the CAR and MEL metastases and in both the total tumor but especially in the ECM-rich regions. However, the presence of these proteins in the tumor was doubled in CAR tumors (laminin, 52±5.9% and 23.3±10.3% and collagen IV, 64.1±11.7% and 36.5±14.4%, in total CAR and MEL tumors, respectively) which reflects the ECM network that comprised ECM-poor regions of CAR tumours but is absent in MEL tumors. In both tumor types, the levels of collagen I were similar: the total tumor levels were decreased (69.6±9.0% and 60.0±18.5%, for CAR and MEL) and the signal intensity in ECM-rich areas was roughly maintained (92.4±44.0% and 115.2±30.4%, for CAR and MEL) although slightly higher in melanoma metastases. Most importantly, fibronectin was significantly overexpressed in the ECM-rich regions of CAR and MEL metastases, reaching up to 3 times the baseline levels (267.8±55.3% and 249.2±85.0%, for CAR and MEL). For the total tumor levels of fibronectin, the MEL tumors levels

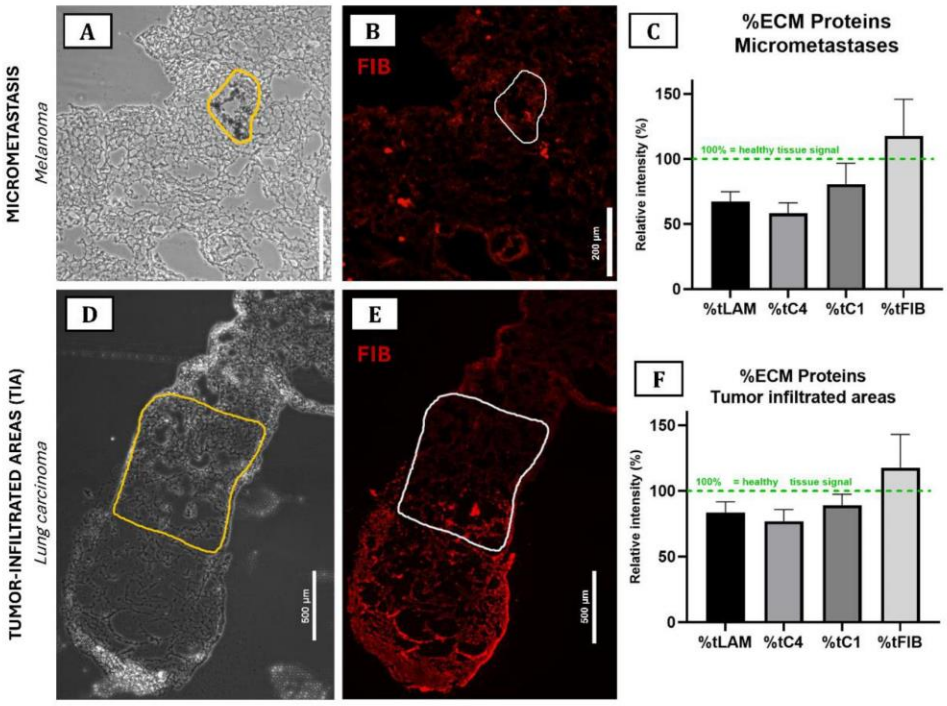

Figure 5 - ECM protein staining and quantification of early-stage invasion areas in CAR metastases (tumor-infiltrated areas, TIA - D-F) and MEL metastases (micrometastases – A-C). Representative phase contrast (A, D) and corresponding fluorescent images (B, E) of acellular tumor sections (20µm) after fibronectin immunostaining (red). The regions of interest were traced on the phase contrast images (yellow selection) and applied to the corresponding fluorescent image (white selection) and the signal was quantified. This quantification was performed for fibronectin, collagen I and IV and laminin in micrometastases ECM (C) and TIA (F). The intensity of healthy lung ECM was normalized to 100% (green line).

were decreased (88.0±23.9%) while the total fibronectin levels in CAR tumors were increased (152.9±34.3%).

f. ECM of tumor invasion shows the same biochemical signature in lung carcinoma and melanoma, despite different phenotype

The staining and quantification of these ECM proteins in micrometastasis' and TIA ECM was performed using the same method, but since these structures don't express ECM-rich regions, only the total ECM signals were computed. In micrometastases, all ECM proteins showed a decrease when compared to the healthy ECM baseline (67.3±7.5% for laminin, 77.0±8.9% for collagen IV and 89.3±8.3% for collagen I) except for fibronectin, that showed a slight increase in mean signal (117.8±28.2%). The same pattern was seen in TIA of lung carcinoma tumors, where there was a degradation of the overall ECM, although less prominent (83.4±8.1% for laminin, 58.3±8.1% for collagen IV and 80.7±16% for collagen I), except for fibronectin which was overexpressed (117.8±25.3%). Once again, this overall degradation of the ECM is consistent with our previous hypothesis: in initial stages of the metastatic development, the cancer cells degrade the prexisting ECM, which is consistent with the ECM softening shown in Figure 2 and suggests an underlying mechanism for tumor invasion of these two models.

Taking into account the presence of the ECM proteins in different locations and tumor stages, it is possible to establish a timeline for tumor ECM compositional dynamics. We hypothesize that when the MEL tumor initially metastasizes, it degrades in general the ECM, but especially the basement membrane (collagen IV and laminin) and stimulates the production of fibronectin, which is overexpressed already in micrometastasis. As the tumor grows, it continues to degrade the ECM while it expands. At around 0.5mm^3, the tumor starts producing an ECM-rich area composed mainly of collagen I and much fibronectin. The tumor progression in CAR metastasis is very similar, except the degradation of the total tumor ECM is much less prominent: although

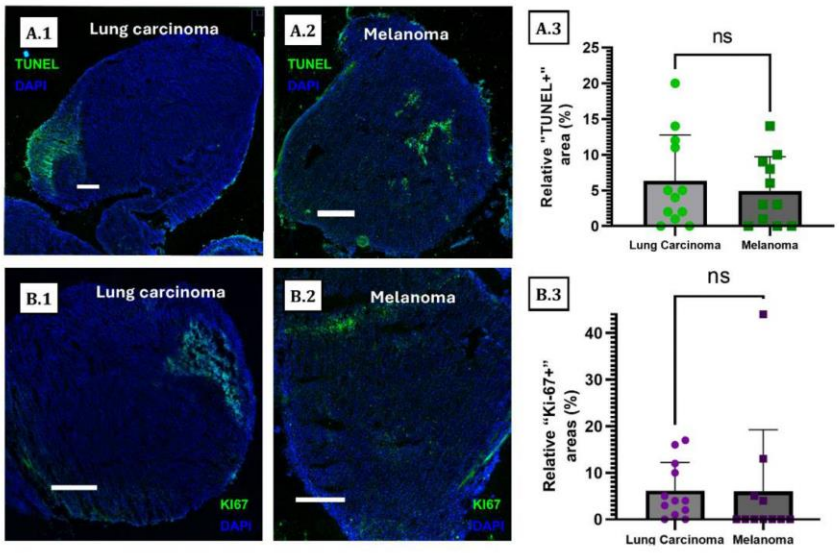

Figure 6 – (A.1-2) Tumor necrosis (TUNEL) and (B.1-2) proliferation (KI67) of CAR and MEL macrometastases. TUNEL+ and KI67+ areas were selected and quantified by normalizing the total tumor area to 100% (A.3 and B.3, respectively). Scale bar = 500μm.

there is a reduction, the tumor forms a soft network of ECM proteins that could potentially be facilitating tumor infiltration to the surrounding tissues, as suggested by the transition from this ECM network into TIA and then into healthy ECM. As the tumor infiltrates the healthy tissue, it again degrades the ECM in general but also gives rise to the deposition of fibronectin.

g. Proliferation and necrosis do not depend on metastasis origin

After establishing the differences in ECM composition between the two tumor models, our next step was to assess if other cellular tumor characteristics like proliferation and necrosis were dependent on the metastasis site or origin. For this purpose, consecutive native slices of the tumors were stained for necrotic (TUNEL) and cell proliferation (Ki-67) markers. The images were quantified by selecting the tumor regions that were positive for these stainings, computing their area and normalizing to a percentage, where 100% equals the total tumor area (**Figure 6** A.3 and B.3). As with the location of the ECM-rich areas, the location of the TUNEL+ areas in CAR and MEL tumors differed in the same way: in CAR tumors, TUNEL+ regions were located

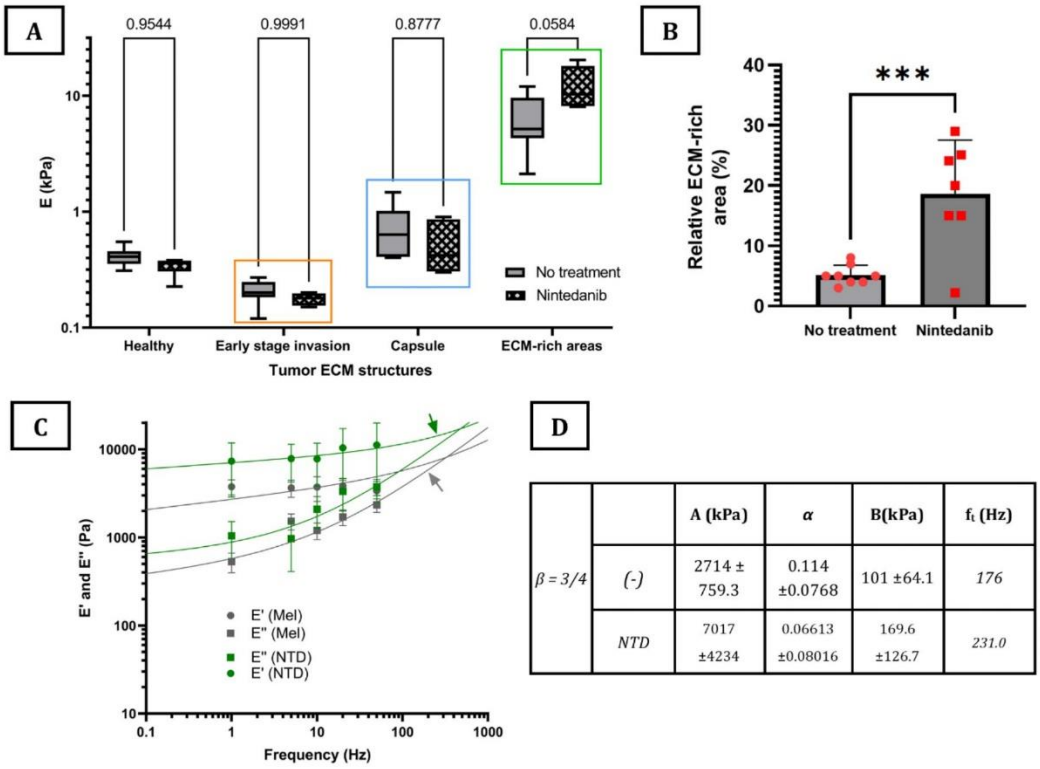

		A (kPa)	α	B(kPa)	f_t (Hz)
β = 3/4	(-)	2714 ± 759.3	0.114 ±0.0768	101 ±64.1	176
	NTD	7017 ±4234	0.06613 ±0.08016	169.6 ±126.7	231.0

Figure 7 – Nintedanib effects on structure and microscale mechanics of melanoma lung metastases. **(A)** Atomic force microscopy (AFM) measurements of the Young's modulus (kPa) of each ECM structure of MEL metastases that either received no treatment or treatment with NTD. P-values obtained using a two-way analysis of variance (ANOVA) with a Tukey post-doc multiple comparisons. **(B)** ECM deposition of ECM-rich regions of MEL macrometastases with and without NTD treatment. Measured by the tumor area occupied by the ECM-rich areas, where the total tumor area was normalized to 100%. Statistical analysis was performed using unpaired parametric student's t-tests (***, p-value < 0.001). **(C)** Frequency dependent loss (E') and storage (E'') modulus as measured by dynamic mechanical analysis (DMA) of the ECM of ECM-rich regions of MEL lung macrometastasis in NTD treated and non-treated mice. Solid lines represent the fits of two-power law model. Arrows indicate the transition frequency. Fit parameters and transition frequency are detailed in table **(D).**

peripherally while in MEL tumors TUNEL+ regions were more centrally located. However, the amount of TUNEL+ regions was similar in both types of metastases (**Figure 6** A.3, 6.3±6.4% and 4.9±4.8%, for CAR and MEL, respectively) although slightly higher for CAR tumors. Regarding Ki67 staining for cell proliferation (**Figure 6** A.4), not all tumors were positive for Ki67 markers, especially in MEL tumors. However, the mean "Ki67+" areas were virtually the same in both models (6.2±6.1% and 6.0±13.2%, for CAR and MEL, respectively). These findings suggest that tumor proliferation and necrosis are dependent on the metastatic niche's location and not on the origin of the metastasis. Furthermore, the similar location within the tumor of necrotic areas and the ECM-rich regions in **Figure 2** suggests a link between tumor angiogenesis and tumor ECM deposition.

After assessing the tumor size, composition, mechanics, necrosis, proliferation, and ECM content, we set out to find relevant correlations between these parameters. Since most data followed a gaussian distribution, we decided to produce a Pearson matrix correlation for each type of metastases, CAR and MEL (**Supplementary Figure 1.A-B**), where the statistically significant correlations are signalled in green. The relevant correlations can be seen in (**Supplementary Figure 1.C-I**). As expected, stiffer ECM-rich areas are (weakly) correlated with an overall increase in ECM-protein presence. However, this is not the case with collagen I in CAR macrometastases, where the relationship is the opposite. In MEL, the area occupied by ECM rich regions decreased with increased tumor diameter, a relationship absent in lung carcinoma. In MEL metastases, it was possible to track ECM protein presence throughout tumor progression (**Supplementary Figure 1.F**) since the tumor's diameter could be measured since the early invasion stages (micrometastases). This analysis clearly showed that basement membrane proteins (laminin and collagen IV) are continuously degraded, while fibronectin levels increase with tumor growth. Collagen I levels, however, are approximately maintained in the different tumor stages.

h. Nintedanib causes a 2x increase in ECM stiffness and 4x increase in ECM deposition

After describing the ECM of lung carcinoma and melanoma metastasis in the lungs, we hypothesised that tumor necrosis and ECM production were linked (due to similar locations within the tumor). Due to their well-established role in modulating the tumor microenvironment and in tumour ECM regulation, we also suspected that activated fibroblasts, i.e. cancer associated fibroblasts, were involved in the production of the tumor ECM. For these reasons, we chose to use Nintedanib (NTD) which was originally developed for oncological applications due to its anti-angiogenic features, but it is believed to also modulate fibroblast proliferation and activation. NTD is an oral medication used for the treatment of idiopathic pulmonary fibrosis and non-small cell lung cancer. We chose to use NTD alongside the melanoma lung metastasis model only, due to its more prominent mechanical changes, structure, and the presence of micrometastases. The same sample preparation, cryosectioning and decellularization protocols previously described were followed for this model.

NTD treatment did not change the previously described structures of the MEL ECM: in macrometastasis, the surrounding ECM capsule, the ECM-rich regions within the capsule, the ECM-poor regions (which were mostly bare) and the micrometastases were all present in NTD treated mice. Using the same protocol described above, we performed AFM and DMA on NTD treated tumors (**Figure 7**). As expected, NTD treatment softened many of the ECM structures. The "healthy" lung ECM was softened after treatment (0.34±0.05kPa and 0.41±0.07kPa, with and without NTD treatment, p=0.9544); the capsule (0.55±0.29kPa, p=0.8777) and the micrometastases (0.18±0.02, p=9991) were also softened with NTD treatment, but not

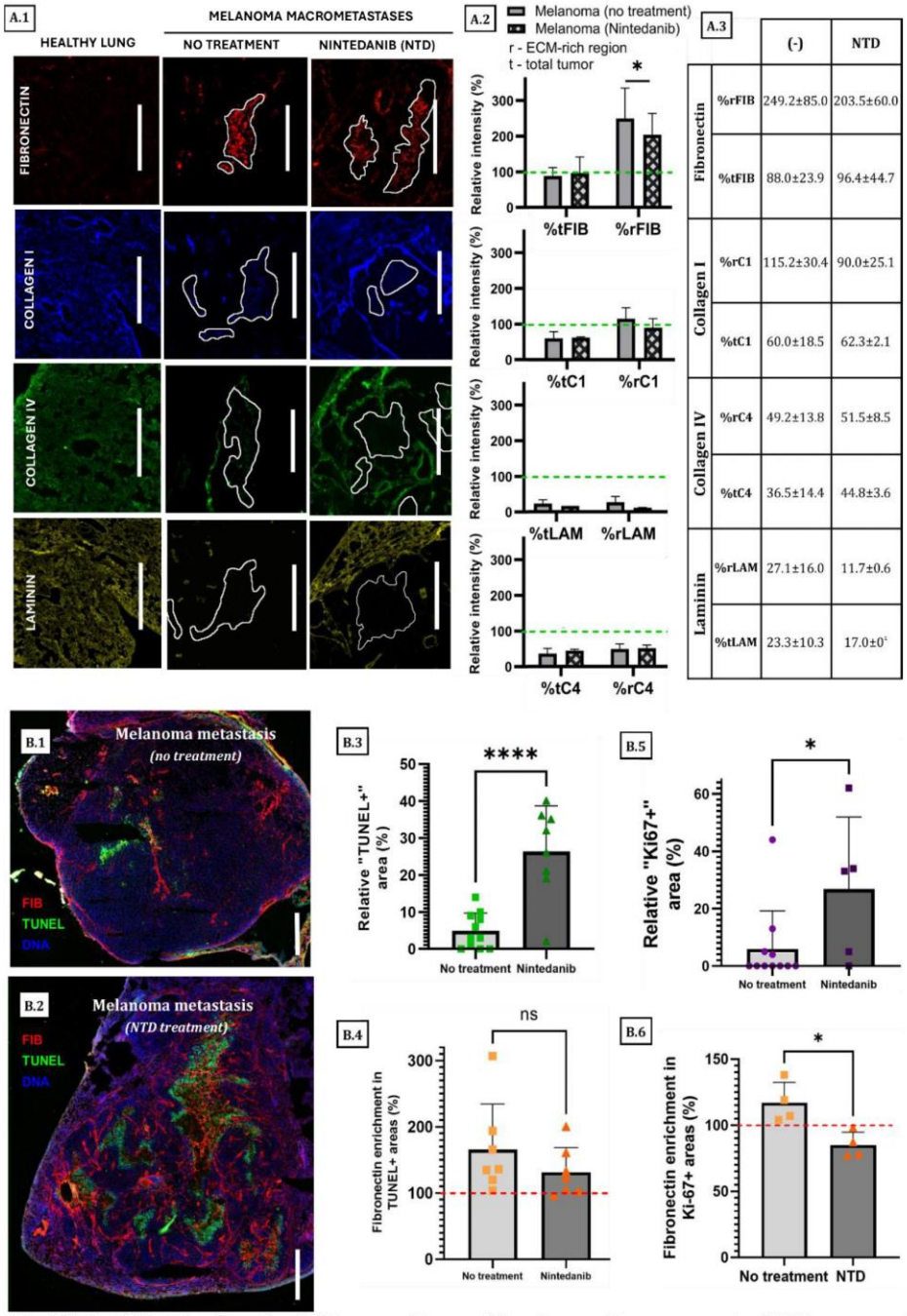

Figure 8 – Effects of Nintedanib on the ECM composition, proliferation, and tumor necrosis of MEL macrometastases, (A.1) - Representative fluorescent images of acellular tumor sections (20µm) after immunostaining of laminin (yellow), collagen IV (green), collagen I (blue) and fibronectin (red). Healthy lung ECM is represented in the left column. ECM-rich areas (%r, white selections) were traced using a phase contrast image and then applied to the corresponding fluorescent image. (A.2-3) – ECM proteins' fluorescent signal quantification of the total tumor (%t) and tumor ECM-rich areas (%r). Healthy lung ECM signal was normalized to 100% (green line). (B) Effect of Nintedanib treatment on tumor necrosis (TUNEL) and (B.1-4) proliferation (KI67) (B.3) TUNEL+ areas and (B.4.) Fibronectin enrichment in TUNEL+ areas. (B.5) KI67+ areas and (B.6) Fibronectin enrichment in KI67+ areas. 100% corresponds to the total tumor measurement. Statistical analysis was performed using unpaired parametric student's t-tests (**, p-value < 0.01, ***, p-value < 0.001). Scale bar = 500µm.

significantly. However, this softening was not observed inside the tumor since NTD caused a 2-

fold increase in stiffness of the ECM-rich regions of the macrometastasis when compared to mice that received no treatment (6.39±3.4kPa and 12.35±5.74kPa, respectively, p=0.0584). Most surprisingly, not only was the NTD treated tumor ECM much stiffer, but the amount of ECM-rich areas in macrometastases almost quadrupled (5.1±1.6% to 18.6±8.9%, p=0.0010).

The same DMA protocol and the two power-law model fit described previously was applied to NTD treated ECM-rich regions of the melanoma macrometastasis. NTD treatment caused a further increase in the values for storage (E') and loss modulus (E''), in-line with the stiffness increase already measured with AFM. In addition, NTD treatment also resulted in the increase in transition frequency from 176 to 231Hz, meaning there was a solidification of the ECM (**Figure 7.B,C**). However, the low frequency α index of NTD-treated ECM-rich regions was half of non-treated melanoma ECM (α=0.066 and 0.114, respectively).

i. Nintedanib increases tumor necrosis and proliferation

After determining that NTD clearly changed the mechanical properties of the tumor ECM, the next step was to assess changes in necrosis, proliferation, and ECM composition. The same ECM quantification method was applied to tumors treated with NTD and the results are (**Figure 8A**). Even though the NTD treated tumor ECM was more abundant and stiffer (as shown previously), the composition of said tumor ECM did not differ much from non-treated melanoma ECM, since there were no significant changes between the composition of both tumor types.

On the other hand, NTD treatment of melanoma metastasis caused a significant and prominent increase in the necrotic areas of the tumors, from 6.3±6.4% to 26.4±12.3% of the total tumor area (**Figure 8.A.1-3**, p<0.0001), as expected due to NTD's anti-angiogenic mode of action. There was also a significant increase in proliferation in the tumors (from 6.0±13.2% to 26.8±25.1 of total tumor area, p=0.0445). To study whether tumor necrosis and proliferation were connected to fibronectin deposition, we decided to compute the fibronectin enrichment of the TUNEL+ and KI67+ areas compared to the average fibronectin content of the whole tumor. Results equal to 100% mean that the distribution of the fibronectin in the area of interest is the same as the distribution in the rest of the tumor; results higher than 100% mean that the fibronectin is more concentrated in this area than in the rest of the tumor, meaning that this area is enriched with fibronectin; results lower than 100% mean that this area is poor in fibronectin compared to the average distribution throughout the tumor. Computing these parameters showed that there was substantial fibronectin enrichment in necrotic areas in tumors treated and not treated with NTD (173.7±72.14% and 131.6±37.4%) while this enrichment was only found in non-treated metastasis in ki67+ areas (117±15.43% and 85±9.8%, for non-treated and treated metastasis, respectively, p=0.0127).

j. Necrosis positively correlates with ECM deposition and stiffening, in mice treated with Nintedanib

As done previously, since most data followed a gaussian distribution, we decided to produce a Pearson correlation matrix using treated and non-treated tumor features (**Supplementary figure 2.A**) and then plotted the relationships that were significant and relevant (**Supplementary figure 2.B-E; Figure 9**).

Since NTD is anti-angiogenic and anti-fibrotic, we were especially interested is studying the relationship between melanoma tumor necrosis (caused by insufficient tumor vascularization), ECM deposition and tumor ECM stiffness. After suppression of tumor vascularization via NTD

treatment, a strong positive relationship between the amount of tumor necrosis and the amount of ECM deposition within the tumor (r=0.998, p<0.001) is clearly established (**Figure 9.A**), which is not observed in non-treated tumors (r=-0.285, p=0.494). This likely means that, in NTD treated mice, the more necrotic the tumor is, the more ECM has been produced. Tumor necrosis and tumor ECM stiffness show a similar association (**Figure 9.B**): the more necrotic the tumor is the stiffer its ECM-rich areas will be (r=0.900, p=0.014) a relationship that is, once again, not observed in non-treated tumors (r=-0.380, p=0.389). However, both tumor models show a positive relationship between ECM stiffness and ECM deposition (**Figure 9.C**), meaning that the more tumor ECM is produced the stiffer it is (r=0.773, p=0.002; r = 0.897, p=0.039 for NTD-treated and non-treated tumors, respectively). These relationships hint at an underlying mechanism that intimately connects tumor angiogenesis and tumor ECM deposition and stiffness.

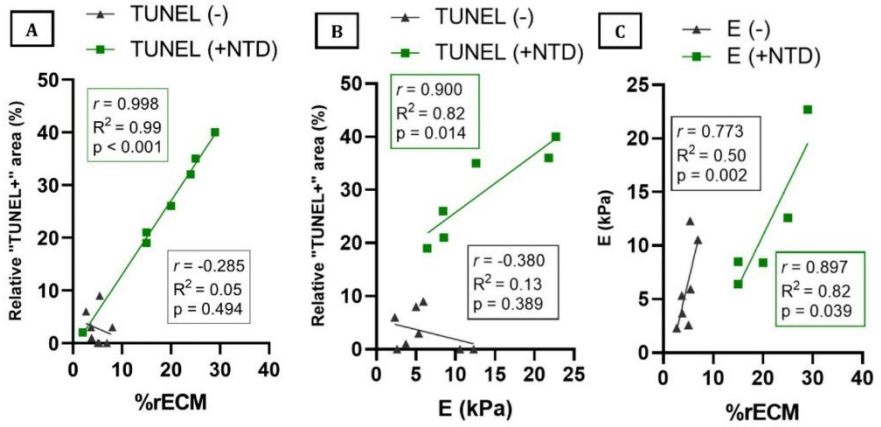

Figure 9 – Correlation analysis of ECM-rich area (%rECM), tumor necrosis (TUNEL+) and stiffness of the ECM-rich areas (E(kPa)) in melanoma macrometastases that received no treatment (-) and received nintedanib treatment (+NTD) for 10 days after initial cancer cell injection. (A) Correlation analysis between tumor necrosis and ECM production. (B) Correlation analysis between tumor necrosis and ECM stiffness of ECM-rich areas. (C) Correlation analysis between ECM-rich stiffness and relative tumor area. P-values (p) and correlation coefficient (*r)* obtained by computing the pearson correlation.

DISCUSSION

In this study, we set out to study the ECM of lung-seeking metastases by decellularizing tumorous sections from two different metastatic models: melanoma lung metastases (B16F10) and Lewis lung carcinoma metastases (LLC1). This study shows that the tumor ECM is not as disorganized and unregulated as previously thought (39,40) and that desmoplasia is not restricted to the tumor surroundings (5,41). Upon decellularization, it became clear that there were different ECM structures that were likely formed by different mechanisms, and not by random deposition or degradation of the pre-metastatic ECM. In contrast with previous studies, our work aimed to assess the mechanics of the ECM throughout metastases progression and with different primary site origins. We were able to show that ECM mechanics can reflect underlying malignant mechanisms and evolve alongside tumor progression, from initial stages of tumor invasion to macrometastases. This study also linked ECM mechanical changes to changes in ECM composition, such as softening caused by basement membrane degradation as well as identify

fibronectin as a key ECM protein displaying deposition changes in every stage of lung metastases progression. When comparing lung carcinoma and melanoma lung-seeking metastases, we found substantially different ECM phenotypes and mechanics, even though proliferation, cell death and ECM composition were the same. Nintedanib treatment of melanoma metastases further exposed the intimate link between angiogenesis and ECM deposition, which will aid in the development of new tumor microenvironment-targeting therapeutics.

One of the main objectives of this study was to compare the tumor ECM of two different metastatic origins (e.g. the "seeds") but on the same target-organ (e.g. the "soil"), according to the "seed and soil" hypothesis (42). Further developments of this hypothesis have postulated whether the seeds recreate their own microenvironment into the new soil or if they depend on the target-organs' features to establish a compatible metastatic niche after their arrival (40). In our study, there is evidence for both. The mechanical features of the tumor ECM support the theory that different origins produce different tumor environments, by attempting to recreate their original microenvironment. In fact, most mechanic parameters measured in lung carcinoma like stiffness, transition frequency and storage and loss modulus were much closer, and sometimes equal to that of the healthy lung ECM, the primary site of CAR metastases. On the contrary, melanoma metastases' ECM had strikingly different mechanics than the surrounding healthy tissue (**Figure 2**, **Figure 3**). This evidence suggests that the mechanical properties of the ECM is dependent on the primary site of the secondary lesions. However, even though ECM-rich regions' location within the tumor were different, their composition was roughly the same regardless of metastatic origin (**Figure 4**). In fact, proliferation, and cell death markers as well as the amount of ECM deposition were very similar in both mice models (**Figure 5**). These similarities could be attributed to an influence of the target organ environment (e.g. the "soil") on tumorigenesis rather than the primary organ site (e.g. the "seed").

Lung carcinoma and melanoma lung metastases also exhibited different invasion phenotypes: the melanoma metastasized to a different location, giving rise to micrometastases, while the lung carcinoma invaded nearby tissues resulting in tumor-infiltraded areas (TIAs). The difference in these presentations could be due to the differences in tumor encapsulation, since only melanoma metastases were fully encapsulated and thus could not easily expand and invade nearby tissues. In fact, it has been suggested that incomplete tumor capsules constitute a risk factor for invasion in hepatocellular carcinomas (43). Although different presentations, the ECM of these two early-stage invasion regions showed the same softening and a very similar composition (**Figure 1D, Figure 5**). In both cases, there was a clear degradation of the basement membrane components (laminin and collagen IV), which results from the cancer cell invasion of new tissues through the basement membrane and has been observed in many cancers, like ovarian and lung carcinomas (44–46). The degradation of the basement membrane is done by MMPs and facilitates the invasion of metastatic cancer cells, but also allows for the growth of new blood vessels during tumor progression (47). This degradation presumably led to the progressive softening of the ECM with increased tumor size we reported in micrometastases (**Figure 2**), which indicates the destabilization of the ECM as the tumor invades the tissue. Surprisingly however, both models of early-stage tumor invasion showed an increase of 18% in fibronectin. In the case of the melanoma micrometastases, fibronectin deposition could be overexpressed to generate a more suitable 'soil' for metastases, which is in line with reports that fibronectin promotes the settling of circulating cancer cells and has many pro-metastatic and tumorigenic qualities (13,48). In fact, recent work has shown that some tumors can prime "pre-metastatic niches" in target-organs before cancer cells leave the primary tumor site. In breast cancer (49), researchers have found that this preparation happens via the deployment of vesicles that will promote the production of growth factors and ECM proteins to create a welcoming environment for the establishment of a new tumor, namely of fibronectin to promote tumor cell engraftment, growth and the recruitment of MMPs to degrade the basement membrane (40), which is line with our results.

Macrometastases decellularization also revealed a dense ECM structure inside the tumor, which we called ECM-rich region. In melanoma metastases, the stiffness measured in this structure

could reach up to ~40kPa, which is 100 times stiffer than healthy ECM, while in the lung carcinoma model ECM stiffness reached a maximum of ~10kPa. In both metastatic mice models, this increase in stiffness can be partially explained by the stark increase in fibronectin when comparing healthy and macrometastasis ECM (**Figure 4**). However, the correlation between stiffness and fibronectin presence, although positive, is weak and non-significant (**Sup. Figure 1.C,E**). This observation indicates that the stiffness of the ECM cannot be solely determined by the amount of ECM components, which is corroborated by the fact that the CAR ECM, even though significantly softer than melanoma ECM, expressed more fibronectin, collagen type IV and laminin than melanoma metastases. The increase in stiffness could be then due to an ECM protein for which we haven't tested, but more likely its due to the well reported overexpression of LOX in intratumoral environments (22,23,50), which covalently crosslinks collagen thereby increasing tissue stiffness. LOX is induced by hypoxic conditions in the tumor (51,52) and its pro-tumorigenic role has been well described (53,54). Thus, hypoxia in the tumor induces ECM stiffening that will in turn promote angiogenesis by stimulating the release of growth factors like vascular endothelial growth factor (VEGF) (55). In fact, when analysing ECM stiffness and development in relation to tumor volume, we can see that the first ECM-rich regions were measured in ~1 mm^3 volume macrometastases, which is consistent with the reported volume at which tumors switch from relying on pre-existing blood supply to a angiogenic phenotype, of around 1-2mm^3 (56–58).

This hypothesis was further corroborated by the results obtained after treatment with nintedanib. Here, VEGF is inhibited (along with other angiogenic factors) which inhibits tumor angiogenesis and thus led to a sharp increase in cell death (**Figure 8.B.3**) when compared to non-treated tumors, which was consistent with previous studies using nintedanib (59). Since these hypoxic conditions are not ameliorated due to the lack of new blood vessels, LOX is continuously secreted into the tumor as hypoxia rises, which could thus explain the doubling in ECM stiffness we reported after nintedanib treatment. This hypoxia-LOX-stiffness relationship is further corroborated by the strong positive correlation between cell death and tumor ECM stiffness (**Figure 9.B**) that is established only after NTD treatment. The link between cell death and ECM deposition is further clarified in **Figure 9.A** since the administration of an anti-angiogenic drug causes a linear relationship between tumor necrosis and ECM deposition, where the more necrotic a tumor is the more ECM is produced. Once again, this relationship hints at the modulation of intra-tumoral ECM deposition as a tool to hinder tumor necrosis and hypoxia.

The relative locations of the ECM-rich regions within the tumor also pointed to a connection between ECM deposition and tumor necrosis, since they were virtually the same. To verify this hypothesis, we computed the fibronectin-enrichment of the TUNEL positive areas, since fibronectin is the main component of ECM-rich areas (which we have equated to ECM deposition). We found that, in fact, TUNEL positive areas had much more fibronectin than the rest of the tumor. This evidence implies that tumor hypoxia and cell death are connected to not only ECM deposition in general, but fibronectin deposition specifically which can also be explained by LOX overexpression. In fact, Wu and colleagues showed that LOX was not only upregulated in higher stiffness substrates in an in vitro model but also that it promoted the production of large quantities of fibronectin by resident fibroblasts (60,61). Of note, fibronectin expression is also linked to an increase in angiogenesis in the tumor, since it facilitates endothelial cell survival, a crucial step in the formation of new blood vessels (39), which could explain its overexpression in the necrotic core.

Even though many studies have singled out collagen I as the main player in tumor ECM (9,11,12,46), in our results fibronectin is the main protein overexpressed throughout the different stages of lung metastases progression, especially in macrometastases. Recent studies have begun to identify fibronectin as an important component in tumor ECM. In fact, in a 2021 study, Ghura and colleagues showed that inhibiting circulation of fibronectin in breast cancer and melanoma mice models led to significant suppression of tumor growth, while inhibition of collagen type I led to no such changes (13). Based on their findings, as well as the ones described

in this study, we propose that targeting of tumor fibronectin could not only suppress cancer growth but also prevent the formation of the pre-metastatic niche and consequent metastatic invasion, opening up a wide range of therapeutic possibilities. Future works should also delve deeper into fibronectin influence on tumor progression, namely on identifying the specific fibronectin isoforms produced in the tumor, as well as other relevant proteins that haven't been covered in this work, like tenascin-C and versican (62,63).

One of the currently approved therapeutic possibilities for lung cancer, specifically non-small cell lung cancer, is NTD. Even though NTD has been progressively recognized as an invaluable anti-fibrotic drug, especially for idiopathic pulmonary fibrosis, its anti-fibrotic actions have not been fully elucidated. As expected, after NTD treatment there was a generalized softening of most ECM structures, though not significant (**Figure 7**). Surprisingly however, NTD caused a 4-fold increase in ECM deposition and 2-fold increase in ECM stiffness in mice with melanoma metastases. Upon closer observation, the ECM structures that softened were the ones that were not directly produced by the tumor components, but rather derived from pre-existing lung ECM (the healthy ECM, the ECM capsule as a result of the tumor expansion, and the micrometastases ECM, resulting from the degradation of the healthy ECM after cancer cell invasion). This evidence suggests that the anti-fibrotic activity of NTD did not produce an effect inside the tumor but only on its surroundings and structures derived from lung ECM. Another explanation for the reported results is that the effects produced by the anti-angiogenic features of NTD override the supposed anti-fibrotic effects, namely the sharp increase in cell death as a result of poor tumor vasculature and hypoxia, which strongly correlated with increased tumor ECM stiffening and deposition (**Figure 9***).* Some previous studies have also shown limited anti-fibrotic action after NTD administration. Namely, some studies have shown no alteration in fibrosis markers or collagen I expression in IPF patients (64,65) after NTD administration. In a brain and breast cancer metastases model, NTD also had no anti-ECM effects (66,67). Collectively, our results and those of others suggest that further investigation in the effect of NTD on the ECM is required to fully understand the effects of this drug in the tumor microenvironment.

By measuring the mechanical characteristics of the tumor ECM, AFM measurements of the tissue can have applications in diagnostics by distinguishing healthy from malignant tissue or by determining the invasive potential of a tumour. Plodinec et al (2012) used AFM to measure the stiffness of human breast cancer biopsies. The study concluded that the mechanical properties of the tissue can be used as a distinct mechanical fingerprint of cancer-related changes, differentiating between normal, benign, and invasive tumours (30). If these findings can be applied to other types of cancers at different stages, nanomechanical signatures can have a high diagnostic potential. In the case of lung-seeking metastases, if the mechanics of the metastatic ECM is consistent with the primary tumor, clinical mechanical measurements could aid in the identification of the primary site especially in cases where histological assessment is not enough (e.g. cancer of unidentified primary, or CUPs).

Finally, our findings indicate missing opportunities in how tumor ECM are being considered in pharmacological approaches. The tumor ECM structures, namely the ECM-rich regions, are not typically targeted in cancer therapeutics and thus, even if cancer cells are removed, the patients are left with extremely stiff and large fibronectin-rich structures in their lungs. Therefore, if left untreated, these structures could not only leave them with lifelong breathing difficulties but, since fibronectin is a chemoattractant and promotes tumor growth, could facilitate "re-invasion" of the tissue. Collectively, our results bring new focus to the role of fibronectin in the reorganization and mechanical changes of the ECM during lung metastasis, but also point to the connection between fibronectin secretion, tumor hypoxia, cell necrosis and potentially LOX expression in the process of tumor development. As such, these interconnections suggest a new arena of signalling cascades that can be targeted against lung tumor development and metastasis.

MATERIALS AND METHODS

Cell culture

Murine melanoma cells B16-F10 (ATCC, #CRL6475) and Lewis lung carcinoma (LCC1) cell line (ATCC, #CRL1642) were kept in high glucose Dulbecco's Modified Eagle's Medium (DMEM) (41966, GIBCO, USA), buffered at pH 7.2–7.4 and supplemented with 10% fetal bovine serum (GIBCO, USA), penicillin–streptomycin solution (104 UI and 10 mg/mL, respectively) (P4333, Sigma–Aldrich, St. Louis, MO, USA), and amphotericin B solution (250 mg/mL) (A2942, Sigma–Aldrich). Cell expansion was achieved by removing the whole medium, detaching the cells by rinsing the culture with 0.25% (w/v) Trypsin–EDTA (1x) solution (25200, GIBCO, USA) and plating aliquots of the cell suspension in flasks incubated at 37 °C and 5% CO2. The cell preparation process took 10 days to complete.

Lung Metastasis Assays

All animal studies in this work were approved by the Institutional Committee of Universitat de Barcelona and the Animal Experimentation Committee of regional authorities (Generalitat de Catalunya, OB 168/19 and 10972) following local and European regulations.

This study was conducted on lungs from pathogen-free mice (8-12 weeks old; male; C57BL/6J; Charles River Laboratories, Saint Germain sur L'arbresle, France). All animals were housed in controlled cages and fed standard rodent chow (Panlab, Barcelona, Spain). Tap water was available ad libitum. Mice were injected intravenously either with 2×10^5 B16-F10 cells or 2.5×10^5 LCC1 cells in 100 µl of physiological saline on the tail vein. On day 21 post injection the animals were sacrificed, and the lungs were harvested and stored at -80ºC.

Sample preparation and cryosectioning

After harvesting, lungs were embedded in Optimum Cutting Temperature compound (OCT, Tissue-Tek, Sakura, Torrance, CA, United States) and stored at -80ºC. Lungs were sectioned at 20 µm using a cryostat with a working temperature of -20ºC. Two to three tissue slices were placed onto each positively charged glass slide (Superfrost Plus; Thermo Fischer Scientific) to minimize the number of slides needed. Consecutive lung slices were marked for further studies. The thickness of 20 µm was a compromise between optical transparency compatible with microscopic imaging and an appropriate thickness for mechanical testing via atomic force microscopy (AFM).

Tumor Decellularization

Decellularization of lung slices was performed as detailed in (68). Briefly, acellular sections were produced by careful and consecutive washes and rinses of the lung section without detachment from the glass slide. Before decellularization, tissue sections were thawed at room temperature for 20 min and the edges of each slide were traced with a liquid repellent slide marker pen (Sigma-Aldrich) to keep liquid from spilling and minimize reagent usage. The OCT was removed by a 20-min incubation of PBS. Cells were lysed by 2 consecutive 10-min washes of ultra-purified water followed by 2 incubations of 15-min each of a mild detergent, sodium deoxycholate 2% (SD), to dissolve the cell membrane and detach cells from the matrix. After the removal of SD with 3 washes of PBS, a 20-min incubation of DNAse I solution (0.3 mg/ml, 5 mM $MgCl_2$, 5mM $CaCl_2$ in 1

mM Tris-HCl) was performed to remove DNA remnants. The DNAse I was removed by 3 consecutive 5-min washes of PBS. After decellularization, samples were not frozen again and were immediately mechanically tested or stained.

Atomic Force Microscopy measurements

The lung and lung tumor ECM were mechanically probed while submersed in PBS at room temperature (RT). The cantilevers used had a nominal spring constant (k) value of 0.03 N/m and a silicon oxide bead with a 5 μm diameter attached to its end (Novascan Technologies, IA). Using our custom-built AFM system, the cantilever was moved by means of piezoactuators coupled to strain gauge sensors (Physik Instrumente, Germany) to measure the vertical displacement of the cantilever (z). The deflection of the cantilever (d) was measured with a four-quadrant photodiode (S4349, Hamamatsu, Japan). Prior to starting measurements, the slope of a deflection-displacement curve ($d - z$) was obtained from the indentation of a bare region of the glass slide. This curve was then used to calibrate the relationship between the photodiode signal and cantilever deflection – the deflection sensitivity. To check if the deflection sensitivity was calculated correctly, the bare region was indented again with this parameter updated. If this plot showed no indentation (perfectly perpendicular to the x axis) with a sharp contact point, then the calibration was considered successful, and it was taken as indicative of a clean undamaged tip.

With the visual assistance of the optical microscope, the tip was positioned macroscopically over the region of interest of the ECM. The deflection and displacement of the cantilever were recorded as the cantilever descended and contacted the sample surface at constant speed of 15 μm/s, which is within the suitable velocity range for lung tissue indentation (69). In each point, the sample was indented 5 times to reduce any measurement-to-measurement variability. In each region, each measuring point was separated by at least 20 μm. 3-5 points were measured in each region, and 3-5 regions were measured in the sample, for a total of 15-25 measurements per structure of interest (e.g. healthy lung ECM, tumor capsule, micrometastasis, etc) unless the complete structure was measured in full with less than 15 indentations. The total duration of each AFM measurements on a given lung sample was ~ 3h. At end of the measurements, the probe was cleaned using helizyme (B. Braun, Germany) followed by ethanol to remove any debris left on the probe.

Atomic Force Microscopy data analysis

Since the tip used in this work was spherical, we considered the Hertz contact model for a sphere indenting a semi-infinite half-space to be the most appropriate model as in line with previous works (18,70,71):

$$F = \frac{4E_m}{3(1 - \vartheta^2)} R^{1/2} \delta^{3/2}$$

where F is the force applied by the cantilever, δ is the sample indentation, R is the radius of the tip, ϑ the Poisson's ratio of the sample (assumed to be 0.5) and E_m is the microscale stiffness of the sample. To compute the model's parameters, each force-deflection curve was fitted through a custom MATLAB code (MATLAB, The MathWorks Inc. MA, United States) by using a maximum of 2 μm of the indenting curve (due to the sample thickness of 20μm and the tip radius of 2.5μm). In this code, the maximum indentation that was taken in the Young's modulus fitting was performed

using the approaching curve and fitting the appropriate tip sample contact model to the force-indentation curve, as described in (71).

Dynamic mechanical analysis and modelling

Viscoelastic properties can be quantified by a frequency-dependent complex shear modulus $E^*(f)$ (18,72,73). This modulus can then be split between its real and imaginary components, as such:

$$E^*(f) = E'(f) + iE''(f)$$

Where E' represents the storage modulus and E'' the loss modulus. The storage and loss modulus were measured by using the "Dynamic Mechanical Analysis" module of the Chiaro nanoindentation instrument (Optics11 Life, Amsterdam) using the same setup as in (74). The spherical tip used was similar to the one chosen for AFM measurements (glass, spring constant = 0.025N/m and tip radius = 3μm). In brief, for each probed location, the tip was set at an operating indentation of ≈1 μm. After a 30 second relaxation period, five 50nm amplitude sine waves separated by 4 second relaxation periods were applied to the sample: 1Hz (5 periods), 5 Hz (10 periods), 10 Hz (20 periods), 20 Hz (20 periods) and 50 Hz (20 periods). Measurements were performed at room temperature (25ºC). Each multifrequency acquisition had a duration of 120s. A total of 6-10 locations were measured for each ECM region (i.e. healthy, ECM-rich). These values were averaged and then fitted in the complex plane to a two power-law model:

$$E^*(f) = A(if)^{\alpha} + B(if)^{\beta}$$

Where the first term of this model describes a low-frequency regime characterized by a weak exponent α, and the second term describes the high-frequency regime. As in previous works (18,38,72), we have fixed the parameter β to ¾ and all fits were performed using online platform *fitteia* (75)(fitteia.org) that applies the non-linear least-squares minimization method.

Based on the two-power law model, we defined the transition frequency (f_t) as the frequency where $A(if_t)^{\alpha} = B(if_t)^{\beta}$, which represents the frequency at which the material, in this case the ECM, transitions from a storage modulus dominated domain (more solid-like) to a loss modulus dominated domain (more fluid-like), hence:

$$f_t = \exp\left(\frac{\ln(B) - \ln(A)}{\alpha - \beta}\right)$$

Volumetric tumor determination

To perform non-invasive volumetric tumor determination we assumed the three-dimensional shape of tumors conforms to a hemielipsoid, as per the current literature (76–79), defined by the following formula:

$$Volume = \frac{\pi}{6}(length) \cdot (width) \cdot (height) \quad (77).$$

The length and width of the tumor can be measured with great precision since they are directly observed, presenting a total error of 3% of the volume (80). However, the height of the tumor presents a challenge, which can add 10.5% error to the volume value (77,81). In order to reduce

this error, an approach based solely on length and width measurements using the modified ellipsoidal formula was used:

$$Tumor\ volume = \frac{1}{2}\ (length \cdot width^2) \qquad (82)$$

The length is the largest longitudinal diameter perpendicular to the largest transverse diameter, or width. The measurements were taken with ImageJ digital image processing software (83) and were performed using either microscopic images of lung slices (micrometastasis) or a mixture of microscopic images and photos of the whole tumor (macrometastasis).

Immunostaining of ECM proteins, TUNEL and Ki-67

Cellular and lung ECM sections were fixed with paraformaldehyde (PFA) 4% for 10 minutes at room temperature (RT). Samples were then blocked using a solution composed of 10% fetal bovine serum (FBS) and supplemented with 3% bovine serum albumin (BSA) for 1 h at RT and constant agitation (80rpm). Lung sections were stained for ECM proteins: laminin, collagen type I, collagen type IV and fibronectin. Cellular lung sections were additionally stained for Ki-67 which was pre-conjugated with Alexa Fluor™ 488 fluorophore (Ki-67 Monoclonal Antibody (SolA15), Alexa Fluor™ 488, eBioscience™, Thermo Fisher) to detect proliferation and terminal deoxynucleotidyl transferase dUTP nick end labelling (TUNEL) to detect final stage apoptotic cells labelled using the Click-iT™ Plus TUNEL Assay Kit (Thermo Fisher, invitrogen) which was also pre-conjugated with Alexa Fluor™ 488 fluorophore. Subsequently, primary antibodies against laminin (1:100, rabbit anti-laminin, Thermo Fisher), collagen type I (1:100, rabbit polyclonal to Collagen I, ab21286, Abcam), collagen type IV (1:100, Rabbit polyclonal to Collagen IV, ab6586, Abcam) and fibronectin (1:100, rabbit anti-fibronectin, ab2413, Abcam) were diluted in the same formulation as the blocking buffer and administered as to submerge the samples completely. Samples were incubated in primary antibody overnight, at 4ºC at constant agitation (80rpm). To remove the primary antibody, sections were washed 3 times for 10 minutes with blocking solution at constant agitation (80rpm). The secondary antibody (1:200, Goat Anti-Rabbit Cy3, ab97075, Abcam) was incubated diluted in the blocking buffer for 2 h, at 37°C and constant agitation (80 rpm). Three 10 min rinses with PBS were performed to wash out the unbound secondary antibodies. DNA was stained by incubation with Hoechst 33342 (NucBlue™ Live ReadyProbes™ Reagent, Thermo Fisher, invitrogen)—for 20min at 80 rpm followed by three 5-min PBS washes to remove the solution. Hoechst staining's concentration was 2 drops per ml, as per the manufacturer's instructions. Finally, samples were mounted using Fluoromount mounting media (Invitrogen™ Fluoromount-G™ Mounting Medium, Thermo Fisher, invitrogen).

Imaging and image processing

For full sample scanning and image stitching, epifluorescent imaging was performed with a Leica DMI 6000 epifluorescent microscope equipped with a Hammamatsu camera ORCA-Spark digital CMOS C11440-36U and a 5× objective. For higher resolution, fluorescent images of the tissue were acquired with a Leica SP5 inverted microscope equipped with a CCD camera (C9100, Hamamatsu Photonics K.K. Hamamatsu, Japan) and using a 10× and 20× Plan Fluor objective (Nikon).

Since the same secondary antibody was used for staining all ECM proteins, the appearance of laminin, collagen I and IV in fluorescent images was changed after image acquisition from red to yellow, blue and green, respectively, solely for easier figure presentation in Fig. 3. Brightness and contrast of phase contrast images of **Figure 2** were improved for the same purpose.

Signal quantification was performed using ImageJ software. For ECM protein quantification, the 'Freehand selections' tool was used to trace the edges of the area of interest (e.g. macrometastasis, micrometastasis, healthy area) using the phase-contrast image of the tumor ECM. Next, a mask was obtained based on this selection and applied to the corresponding fluorescent image (e.g. fibronectin, laminin, collagen). This selected area was then measured for mean intensity value and normalized using the mean intensity of the healthy ECM of the same lung section, as:

$$Tumor\ protein\ intensity = \frac{Protein\ mean\ intensity\ in\ the\ tumor}{Protein\ mean\ intensity\ in\ the\ healthy\ region} \times 100\%$$

A similar procedure was followed for the computation of the area of the region of interest, but by normalizing with the area of the full tumor, as:

$$Area\ of\ ROI = \frac{Area\ of\ ROI\ (pixels)}{Full\ tumor\ area\ (pixels)} \times 100\%$$

such was the case for the computation of the necrotic, proliferative area and macrometastasis' ECM production.

To compute the coincidence of necrotic and proliferative areas with fibronectin and laminin tumor presence, the necrotic/proliferative positive areas in the FITC channel were traced and then masked. This mask was then applied to the fibronectin/laminin channel to determine the intensity of these proteins in the necrotic or proliferative tumor regions. This value would then be compared to the presence of the ECM proteins of the complete tumor area, as:

$$Protein\ coincidence = \frac{Protein\ mean\ intensity\ in\ the\ ROI}{Protein\ mean\ intensity\ in\ the\ whole\ tumor} \times 100\%$$

A random distribution of the protein would yield results of approximately 100% whereas a value of $> 100\%$ means that the protein displays larger concentrations in the ROI than in the rest of the tumor. By always normalizing the results with regions of the same lung section, we decrease the influence of errors caused by irregular cryosections and immunostaining inconsistencies.

Decellularization quantification was performed using the custom python algorithm described in detail in (84).

Nintedanib treatment assay

To simulate a clinical timeline, after 10 days post metastatic cancer cell injection, mice previously injected with the murine melanoma cells B16-F10 started receiving treatment with Nintedanib (50 mg/kg, dissolved in PBS) by oral gavage. This treatment was administered daily for 11 days. On day 21 post injection the animals were sacrificed, and the lungs were harvested and frozen at -80ºC.

Statistical Analysis

All data are mean ±SD. Normal and lognormal distribution of the datasets was tested using Shapiro-Wilk normality and lognormality tests. For comparison between two groups, since most groups followed a gaussian distribution, unpaired parametric student's t-tests were used. Datasets with more than one group followed a lognormal distribution. To achieve the gaussian distribution necessary for further statistical analysis, datasets were converted to their logarithm

and a two-way analysis of variance (ANOVA) with a Tukey post-doc multiple comparisons test was used. The relationship between variables were computed using Pearson correlations, since most datasets followed a gaussian distribution. To avoid clinically irrelevant correlations, we have only plotted relevant and/or significant correlations in supplementary figure 1-2. Differences were considered statistically significant for p-value < 0.05. Statistical analysis and the generation of graphs was performed using GraphPad Prism (GraphPad software 9.1.0, Inc., San Diego, CA, USA).

CONFLICT OF INTEREST

The authors declare no conflicts of interest.

ETHICS STATEMENT

This work was approved by the Institutional Committee of Universitat de Barcelona and the Animal experimentation Committee of regional authorities (Generalitat de Catalunya, OB 168/19 and 10972).

AUTHOR CONTRIBUTIONS

Conceptualization, M.N., R.F., I.A. and N.G.; Formal analysis, M.N. and N.G.; Funding acquisition, D.N. and R.F.; Investigation, M.N., A.M, A.U., N.D., K.N, M.B.; Methodology, M.N., C.J., A.M., N.D., J.A., I.A. and N.G.; Data Analysis, M.N., C.J., A.M., M.B., Project administration, D.N., R.F., I.A. and N.G.; Resources, D.N., R.F., J.A., N.G. and I.A.; Supervision, I.A. and N.G.; Writing of original draft, M.N. and N.G. All authors have read and agreed to the published version of the manuscript.

FUNDING

MN and CJ were funded by the H2020 European Research and Innovation Programme under the Marie Skłodowska-Curie grant agreement “Phys2BioMed” contract no. 812772. IA is funded by Ministerio de Ciencia e Innovación (PID2019-108958RB-I00/ AEI/ 10.13039/501100011033) and SEPAR (900-2019). RF, JO, and NG were funded by the Spanish Ministry of Sciences, Innovation and Universities, PID2020-113910RB-I00-AEI/10.13039/501100011033, PGC2018-097323-A-I00, and PID2020-116808RB-I00 AEI-Retos, respectively.

ACKNOWLEDGEMENTS

We thank the Advanced Optical Microscopy Unit from Scientific and Technological Centres from University of Barcelona for their support and advice with the epifluorescent microscopy technique.

SUPPLEMENTARY MATERIAL

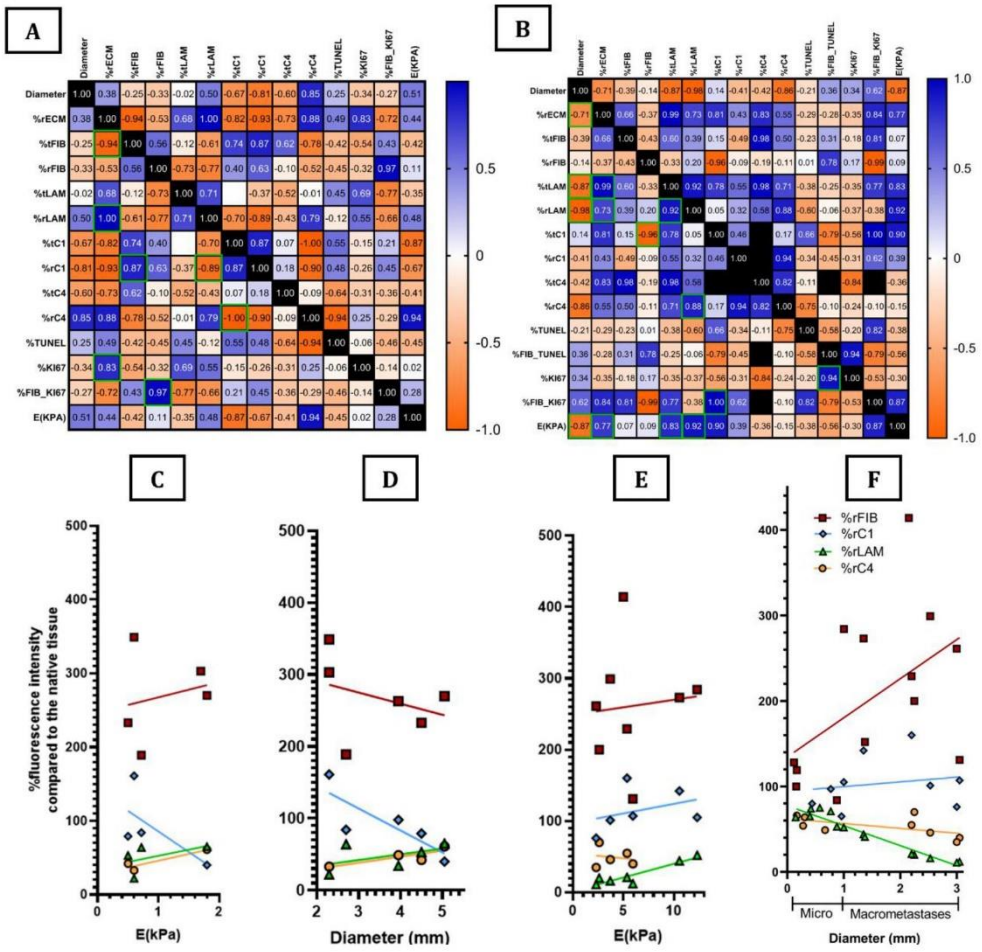

Supplementary Figure 1 - Correlation analysis between all measured variables in CAR and MEL metastases. (A-B) Pearson correlation matrix with Pearson correlation coefficients for CAR and MEL metastases, respectively. Green boxes indicate statistically significant correlations ($p<0.05$). Relationship between ECM proteins (fibronectin, laminin, collagen I and IV) and (C) stiffness in CAR; (D) diameter in CAR; (E) stiffness in MEL and (F) diameter in MEL micro and macro metastases. Only significant and/or biologically relevant correlations were plotted.

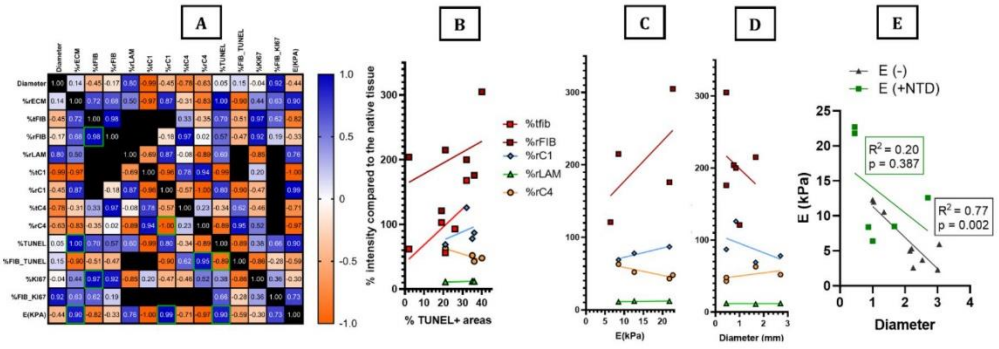

Supplementary Figure 2 - Correlation analysis between all measured variables in NTD-treated MEL metastases. (A) Pearson correlation matrix with Pearson correlation coefficients for NTD-treated MEL metastases. Green boxes indicate statistically significant correlations ($p<0.05$). Relationship between ECM proteins (fibronectin, laminin, collagen I and IV) and (B) tumor necrosis, measured by TUNEL+ areas; (C) ECM stiffness and (D) macrometastases' diameter. Correlation analysis in MEL (treated (-) and non-treated (+)) between stiffness of the ECM-rich areas and (E) macrometastases diameter. P-values (p) obtained by computing the pearson correlation. Only significant and/or biologically relevant correlations were plotted.

REFERENCES

1. Wang SB, Chen ZX, Gao F, Zhang C, Zou MZ, Ye JJ, et al. Remodeling extracellular matrix based on functional covalent organic framework to enhance tumor photodynamic therapy. Biomaterials. 2020 Mar;234:119772.

2. Lu P, Weaver VM, Werb Z. The extracellular matrix: A dynamic niche in cancer progression. J Cell Biol. 2012 Feb 20;196(4):395–406.

3. Nelson MT, Short A, Cole SL, Gross AC, Winter J, Eubank TD, et al. Preferential, enhanced breast cancer cell migration on biomimetic electrospun nanofiber 'cell highways'. BMC Cancer. 2014 Dec;14(1):825.

4. Giussani M, Merlino G, Cappelletti V, Tagliabue E, Daidone MG. Tumor-extracellular matrix interactions: Identification of tools associated with breast cancer progression. Semin Cancer Biol. 2015 Dec;35:3–10.

5. Conti JA, Kendall TJ, Bateman A, Armstrong TA, Papa-Adams A, Xu Q, et al. The Desmoplastic Reaction Surrounding Hepatic Colorectal Adenocarcinoma Metastases Aids Tumor Growth and Survival via αv Integrin Ligation. Clin Cancer Res. 2008 Oct 15;14(20):6405–13.

6. Schober M, Jesenofsky R, Faissner R, Weidenauer C, Hagmann W, Michl P, et al. Desmoplasia and Chemoresistance in Pancreatic Cancer. Cancers. 2014 Oct 21;6(4):2137–54.

7. Rice AJ, Cortes E, Lachowski D, Cheung BCH, Karim SA, Morton JP, et al. Matrix stiffness induces epithelial–mesenchymal transition and promotes chemoresistance in pancreatic cancer cells. Oncogenesis. 2017 Jul;6(7):e352–e352.

8. Laklai H, Miroshnikova YA, Pickup MW, Collisson EA, Kim GE, Barrett AS, et al. Genotype tunes pancreatic ductal adenocarcinoma tissue tension to induce matricellular fibrosis and tumor progression. Nat Med. 2016 May;22(5):497–505.

9. Acerbi I, Cassereau L, Dean I, Shi Q, Au A, Park C, et al. Human breast cancer invasion and aggression correlates with ECM stiffening and immune cell infiltration. Integr Biol. 2015 Oct 5;7(10):1120–34.

10. Qiu X, Tan H, Fu D, Zhu Y, Zhang J. Laminin is over expressed in breast cancer and facilitate cancer cell metastasis. J Cancer Res Ther. 2018;14(7):1170.

11. Provenzano PP, Inman DR, Eliceiri KW, Knittel JG, Yan L, Rueden CT, et al. Collagen density promotes mammary tumor initiation and progression. BMC Med. 2008 Dec;6(1):11.

12. Mammoto T, Jiang A, Jiang E, Panigrahy D, Kieran MW, Mammoto A. Role of Collagen Matrix in Tumor Angiogenesis and Glioblastoma Multiforme Progression. Am J Pathol. 2013 Oct;183(4):1293–305.

13. Ghura H, Keimer M, von Au A, Hackl N, Klemis V, Nakchbandi IA. Inhibition of fibronectin accumulation suppresses tumor growth. Neoplasia. 2021 Sep;23(9):837–50.

14. Yang N, Mosher R, Seo S, Beebe D, Friedl A. Syndecan-1 in Breast Cancer Stroma Fibroblasts Regulates Extracellular Matrix Fiber Organization and Carcinoma Cell Motility. Am J Pathol. 2011 Jan;178(1):325–35.

15. Provenzano PP, Inman DR, Eliceiri KW, Trier SM, Keely PJ. Contact Guidance Mediated Three-Dimensional Cell Migration is Regulated by Rho/ROCK-Dependent Matrix Reorganization. Biophys J. 2008 Dec;95(11):5374–84.

16. Conklin MW, Eickhoff JC, Riching KM, Pehlke CA, Eliceiri KW, Provenzano PP, et al. Aligned Collagen Is a Prognostic Signature for Survival in Human Breast Carcinoma. Am J Pathol. 2011 Mar;178(3):1221–32.

17. Nagelkerke A, Bussink J, Rowan AE, Span PN. The mechanical microenvironment in cancer: How physics affects tumours. Semin Cancer Biol. 2015 Dec;35:62–70.

18. Júnior C, Narciso M, Marhuenda E, Almendros I, Farré R, Navajas D, et al. Baseline Stiffness Modulates the Non-Linear Response to Stretch of the Extracellular Matrix in Pulmonary Fibrosis. Int J Mol Sci. 2021 Nov 29;22(23):12928.

19. Chaudhuri O, Koshy ST, Branco da Cunha C, Shin JW, Verbeke CS, Allison KH, et al. Extracellular matrix stiffness and composition jointly regulate the induction of malignant phenotypes in mammary epithelium. Nat Mater. 2014 Oct;13(10):970–8.

20. Vogel V, Sheetz M. Local force and geometry sensing regulate cell functions. Nat Rev Mol Cell Biol. 2006 Apr;7(4):265–75.

21. Engler AJ, Sen S, Sweeney HL, Discher DE. Matrix Elasticity Directs Stem Cell Lineage Specification. Cell. 2006 Aug;126(4):677–89.

22. Baker AM, Bird D, Lang G, Cox TR, Erler JT. Lysyl oxidase enzymatic function increases stiffness to drive colorectal cancer progression through FAK. Oncogene. 2013 Apr 4;32(14):1863–8.

23. Barker HE, Chang J, Cox TR, Lang G, Bird D, Nicolau M, et al. LOXL2-Mediated Matrix Remodeling in Metastasis and Mammary Gland Involution. Cancer Res. 2011 Mar 1;71(5):1561–72.

24. Levental KR, Yu H, Kass L, Lakins JN, Egeblad M, Erler JT, et al. Matrix Crosslinking Forces Tumor Progression by Enhancing Integrin Signaling. Cell. 2009 Nov;139(5):891–906.

25. Wei SC, Fattet L, Tsai JH, Guo Y, Pai VH, Majeski HE, et al. Matrix stiffness drives epithelial–mesenchymal transition and tumour metastasis through a TWIST1–G3BP2 mechanotransduction pathway. Nat Cell Biol. 2015 May;17(5):678–88.

26. Yilmaz M, Christofori G. EMT, the cytoskeleton, and cancer cell invasion. Cancer Metastasis Rev. 2009 Jun;28(1–2):15–33.

27. Ulbricht A, Eppler FJ, Tapia VE, van der Ven PFM, Hampe N, Hersch N, et al. Cellular Mechanotransduction Relies on Tension-Induced and Chaperone-Assisted Autophagy. Curr Biol. 2013 Mar;23(5):430–5.

28. Nagelkerke A, Sweep FCGJ, Geurts-Moespot A, Bussink J, Span PN. Therapeutic targeting of autophagy in cancer. Part I: Molecular pathways controlling autophagy. Semin Cancer Biol. 2015 Apr;31:89–98.

29. Nagelkerke A, Bussink J, Geurts-Moespot A, Sweep FCGJ, Span PN. Therapeutic targeting of autophagy in cancer. Part II: Pharmacological modulation of treatment-induced autophagy. Semin Cancer Biol. 2015 Apr;31:99–105.

30. Plodinec M, Loparic M, Monnier CA, Obermann EC, Zanetti-Dallenbach R, Oertle P, et al. The nanomechanical signature of breast cancer. Nat Nanotechnol. 2012 Nov;7(11):757–65.

31. Cross SE, Jin YS, Rao J, Gimzewski JK. Nanomechanical analysis of cells from cancer patients. Nat Nanotechnol. 2007 Dec;2(12):780–3.

32. Ansardamavandi A, Tafazzoli-Shadpour M, Omidvar R, Jahanzad I. Quantification of effects of cancer on elastic properties of breast tissue by Atomic Force Microscopy. J Mech Behav Biomed Mater. 2016 Jul;60:234–42.

33. Panzetta V, Musella I, Rapa I, Volante M, Netti PA, Fusco S. Mechanical phenotyping of cells and extracellular matrix as grade and stage markers of lung tumor tissues. Acta Biomater. 2017 Jul;57:334–41.

34. Costa-Silva B, Aiello NM, Ocean AJ, Singh S, Zhang H, Thakur BK, et al. Pancreatic cancer exosomes initiate pre-metastatic niche formation in the liver. Nat Cell Biol. 2015 Jun;17(6):816–26.

35. Mohammed TLH, Chowdhry A, Amorosa JK, Ginsburg ME, Heitkamp DE, MacMahon H, et al. ACR Appropriateness Criterias Screening for Pulmonary Metastases. :3.

36. Almendros I, Montserrat JM, Torres M, Bonsignore MR, Chimenti L, Navajas D, et al. Obesity and intermittent hypoxia increase tumor growth in a mouse model of sleep apnea. Sleep Med. 2012 Dec;13(10):1254–60.

37. Marhuenda E, Campillo N, Gabasa M, Martínez-García MA, Campos-Rodríguez F, Gozal D, et al. Effects of Sustained and Intermittent Hypoxia on Human Lung Cancer Cells. 2019;61(4):5.

38. Luque T, Melo E, Garreta E, Cortiella J, Nichols J, Farré R, et al. Local micromechanical properties of decellularized lung scaffolds measured with atomic force microscopy. Acta Biomater. 2013 Jun;9(6):6852–9.

39. Ribeiro Franco PI, Rodrigues AP, de Menezes LB, Pacheco Miguel M. Tumor microenvironment components: Allies of cancer progression. Pathol - Res Pract. 2020 Jan;216(1):152729.

40. Ghajar CM, Correia AL, Bissell MJ. The Role of the Microenvironment in Tumor Initiation, Progression, and Metastasis. In: The Molecular Basis of Cancer [Internet]. Elsevier; 2015 [cited 2022 Jul 3]. p. 239-256.e5. Available from: https://linkinghub.elsevier.com/retrieve/pii/B9781455740666000160

41. Stella GM, Kolling S, Benvenuti S, Bortolotto C. Lung-Seeking Metastases. Cancers. 2019 Jul 19;11(7):1010.

42. Fidler IJ. The pathogenesis of cancer metastasis: the 'seed and soil' hypothesis revisited. Nat Rev Cancer. 2003 Jun;3(6):453–8.

43. Zhu F, Yang F, Li J, Chen W, Yang W. Incomplete tumor capsule on preoperative imaging reveals microvascular invasion in hepatocellular carcinoma: a systematic review and meta-analysis. Abdom Radiol. 2019 Sep;44(9):3049–57.

44. Cox TR. The matrix in cancer. Nat Rev Cancer. 2021 Apr;21(4):217–38.

45. Bar JK, Grelewski P, Popiela A, Noga L, Rabczyñski J. Type IV collagen and CD44v6 expression in benign, malignant primary and metastatic ovarian tumors: correlation with Ki-67 and p53 immunoreactivity. Gynecol Oncol. 2004 Oct;95(1):23–31.

46. Fang S, Dai Y, Mei Y, Yang M, Hu L, Yang H, et al. Clinical significance and biological role of cancer-derived Type I collagen in lung and esophageal cancers: Type I collagen in NSCLC and ESCC. Thorac Cancer. 2019 Feb;10(2):277–88.

47. Chang J, Chaudhuri O. Beyond proteases: Basement membrane mechanics and cancer invasion. J Cell Biol. 2019 Aug 5;218(8):2456–69.

48. Lin TC, Yang CH, Cheng LH, Chang WT, Lin YR, Cheng HC. Fibronectin in Cancer: Friend or Foe. Cells. 2019 Dec 20;9(1):27.

49. Chen X, Feng J, Chen W, Shao S, Chen L, Wan H. Small extracellular vesicles: from promoting pre-metastatic niche formation to therapeutic strategies in breast cancer. Cell Commun Signal. 2022 Sep 12;20(1):141.

50. Wei B, Zhou X, Liang C, Zheng X, Lei P, Fang J, et al. Human colorectal cancer progression correlates with LOX-induced ECM stiffening. Int J Biol Sci. 2017;13(11):1450–7.

51. Gilkes DM, Bajpai S, Chaturvedi P, Wirtz D, Semenza GL. Hypoxia-inducible Factor 1 (HIF-1) Promotes Extracellular Matrix Remodeling under Hypoxic Conditions by Inducing P4HA1, P4HA2, and PLOD2 Expression in Fibroblasts. J Biol Chem. 2013 Apr;288(15):10819–29.

52. Pez F, Dayan F, Durivault J, Kaniewski B, Aimond G, Le Provost GS, et al. The HIF-1–Inducible Lysyl Oxidase Activates HIF-1 via the Akt Pathway in a Positive Regulation Loop and Synergizes with HIF-1 in Promoting Tumor Cell Growth. Cancer Res. 2011 Mar 1;71(5):1647–57.

53. Vázquez-Naharro A, Bustos-Tauler J, Floristán A, Yuste L, Oltra SS, Vinyals A, et al. Loxl3 Promotes Melanoma Progression and Dissemination Influencing Cell Plasticity and Survival. Cancers. 2022 Feb 25;14(5):1200.

54. Saatci O, Kaymak A, Raza U, Ersan PG, Akbulut O, Banister CE, et al. Targeting lysyl oxidase (LOX) overcomes chemotherapy resistance in triple negative breast cancer. Nat Commun. 2020 Dec;11(1):2416.

55. Laczko R, Csiszar K. Lysyl Oxidase (LOX): Functional Contributions to Signaling Pathways. Biomolecules. 2020 Jul 22;10(8):1093.

56. Ribatti D. Judah Folkman, a pioneer in the study of angiogenesis. Angiogenesis. 2008 Mar;11(1):3–10.

57. Hillen F, Griffioen AW. Tumour vascularization: sprouting angiogenesis and beyond. Cancer Metastasis Rev. 2007 Dec;26(3–4):489–502.

58. Anderson NM, Simon MC. The tumor microenvironment. Curr Biol. 2020 Aug;30(16):R921–5.

59. Tu J, Xu H, Ma L, Li C, Qin W, Chen X, et al. Nintedanib enhances the efficacy of PD-L1 blockade by upregulating MHC-I and PD-L1 expression in tumor cells. Theranostics. 2022;12(2):747–66.

60. Wu S, Zheng Q, Xing X, Dong Y, Wang Y, You Y, et al. Matrix stiffness-upregulated LOXL2 promotes fibronectin production, MMP9 and CXCL12 expression and BMDCs recruitment to assist pre-metastatic niche formation. J Exp Clin Cancer Res. 2018 Dec;37(1):99.

61. Wu S, Xing X, Wang Y, Zhang X, Li M, Wang M, et al. The pathological significance of LOXL2 in pre-metastatic niche formation of HCC and its related molecular mechanism. Eur J Cancer. 2021 Apr;147:63–73.

62. Gocheva V, Naba A, Bhutkar A, Guardia T, Miller KM, Li CMC, et al. Quantitative proteomics identify Tenascin-C as a promoter of lung cancer progression and contributor to a signature prognostic of patient survival. Proc Natl Acad Sci [Internet]. 2017 Jul 11 [cited 2022 Oct 3];114(28). Available from: https://pnas.org/doi/full/10.1073/pnas.1707054114

63. dos Reis DC, Damasceno KA, de Campos CB, Veloso ES, Pêgas GRA, Kraemer LR, et al. Versican and Tumor-Associated Macrophages Promotes Tumor Progression and Metastasis in Canine and Murine Models of Breast Carcinoma. Front Oncol. 2019 Jul 3;9:577.

64. Lehmann M, Buhl L, Alsafadi HN, Klee S, Hermann S, Mutze K, et al. Differential effects of Nintedanib and Pirfenidone on lung alveolar epithelial cell function in ex vivo murine and human lung tissue cultures of pulmonary fibrosis. Respir Res. 2018 Dec;19(1):175.

65. Decaris ML, Schaub JR, Chen C, Cha J, Lee GG, Rexhepaj M, et al. Dual inhibition of αvβ6 and αvβ1 reduces fibrogenesis in lung tissue explants from patients with IPF. Respir Res. 2021 Dec;22(1):265.

66. Brooks D, Zimmer A, Wakefield L, Lyle LT, Difilippantonio S, Tucci FC, et al. Limited fibrosis accompanies triple-negative breast cancer metastasis in multiple model systems and is not a preventive target. Oncotarget. 2018 May 4;9(34):23462–81.

67. Kovalchuk B, Berghoff AS, Karreman MA, Frey K, Piechutta M, Fischer M, et al. Nintedanib and a bi-specific anti-VEGF/Ang2 nanobody selectively prevent brain metastases of lung adenocarcinoma cells. Clin Exp Metastasis. 2020 Dec;37(6):637–48.

68. Narciso M, Ulldemolins A, Júnior C, Otero J, Navajas D, Farré R, et al. Novel Decellularization Method for Tissue Slices. Front Bioeng Biotechnol. 2022 Mar 9;10:832178.

69. Liu F, Tschumperlin DJ. Micro-Mechanical Characterization of Lung Tissue Using Atomic Force Microscopy. J Vis Exp. 2011 Aug 28;(54):2911.

70. Liu F, Mih JD, Shea BS, Kho AT, Sharif AS, Tager AM, et al. Feedback amplification of fibrosis through matrix stiffening and COX-2 suppression. J Cell Biol. 2010 Aug 23;190(4):693–706.

71. Jorba I, Beltrán G, Falcones B, Suki B, Farré R, García-Aznar JM, et al. Nonlinear elasticity of the lung extracellular microenvironment is regulated by macroscale tissue strain. Acta Biomater. 2019 Jul;92:265–76.

72. Andreu I, Luque T, Sancho A, Pelacho B, Iglesias-García O, Melo E, et al. Heterogeneous micromechanical properties of the extracellular matrix in healthy and infarcted hearts. Acta Biomater. 2014 Jul;10(7):3235–42.

73. Rigato A, Miyagi A, Scheuring S, Rico F. High-frequency microrheology reveals cytoskeleton dynamics in living cells. Nat Phys. 2017 Aug;13(8):771–5.

74. Antonovaite N, Beekmans SV, Hol EM, Wadman WJ, Iannuzzi D. Regional variations in stiffness in live mouse brain tissue determined by depth-controlled indentation mapping. Sci Rep. 2018 Dec;8(1):12517.

75. Sebastião PJ. The art of model fitting to experimental results. Eur J Phys. 2014 Jan 1;35(1):015017.

76. Faustino-Rocha A, Oliveira PA, Pinho-Oliveira J, Teixeira-Guedes C, Soares-Maia R, Da Costa RG, et al. Estimation of rat mammary tumor volume using caliper and ultrasonography measurements. Lab Anim. 2013 Jun;42(6):217–24.

77. Feldman JP, Goldwasser R, Mark S, Shwartz J, Orion I. A mathematical model for volume evaluation using two-dimensions. J Appl Quant Methods. 2009;4(4):455–62.

78. Singhal S, Gill M, Srivastava C, Gupta D, Kumar A, Kaushik A, et al. Simplifying Tumor Volume Estimation from Linear Dimensions for Intra-Cranial Lesions Treated with Stereotactic Radiosurgery.pdf. J Med Phys. 2020;45(4):199–205.

79. Voss B, Wilop S, Jonas S, El-komy MHM, Unit KA ainy P. Tumor Volume as a Prognostic Factor in Resectable Malignant Melanoma. 2014;(June).

80. Tomayko MM, Reynolds CP. Determination of subcutaneous tumor size in athymic (nude) mice. Cancer Chemother Pharmacol. 1989;24(3):148–54.

81. Dethlefsen LA, Prewitt JMS, Mendelsohn ML. Analysis of tumor growth curves. J Natl Cancer Inst. 1968;40(2):389–405.

82. Jensen MM, Jørgensen JT, Binderup T, Kjær A. Tumor volume in subcutaneous mouse xenografts measured by microCT is more accurate and reproducible than determined by 18F-FDG-microPET or external caliper. BMC Med Imaging. 2008 Oct 16;8:16.

83. Schneider CA, Rasband WS, Eliceiri KW. NIH Image to ImageJ: 25 years of image analysis. Nat Methods 2012 97. 2012 Jun 28;9(7):671–5.

84. Narciso M, Otero J, Navajas D, Farré R, Almendros I, Gavara N. Image-Based Method to Quantify Decellularization of Tissue Sections. Int J Mol Sci. 2021 Aug 5;22(16):8399.

Chapter IV.

DISCUSSION

Discussion

The overarching objective of this doctoral thesis is to study the ECM of lung cancer, both mechanically and biochemically. To achieve this goal, it was necessary to isolate the ECM from the surrounding cancer cells, e.g. to decellularize the tumor, while preserving the tumor's structure. Even though decellularization had become commonplace for many research applications and samples, from tissues (90) to cell culture derived ECM (52), there were scarce examples of tumor decellularization protocols and these did not meet the requirements for our research question. For instance, decellularization has been performed on discarded human tumor tissue from colon resections to create tumor-derived ECM hydrogels (116). Tumor pieces of 3x3mm were decellularized using SDC, Triton X-100 and dH_2O at constant 300rpm agitation. Another example is the procedure followed by Wishart and colleagues where they excised breast cancer tumors from mice and proceeded to decellularize them in SDS, Triton and dH_2O (91). Albeit successful, these decellularization procedures were not suitable for our experimental setup for several reasons:

(1) These procedures did not preserve the original tumor architecture, as can be seen in the change in physical appearance before and after decellularization in (91), where the tumor has significantly reduced in size. In retrospect, had we used one of these protocols, the ECM-rich regions would most likely have been disrupted. ECM-rich regions are centrally located in melanoma tumors and surrounded only by cancer cells, so by removing the cells, the ECM-rich regions would have most likely been removed as well.
(2) In the melanoma metastases model used in our project, the tumors produced are highly viscous and can easily be ruptured, complicating their excision tremendously, so a protocol where tumor isolation is required is not recommended for this application.
(3) The aforementioned protocols are only suitable for large and highly distinct macrometastases and in our work we were interested in characterizing tumors in different stages of tumor progression, which included micrometastases.

(4) Some tumors in the lung carcinoma model had to be located beforehand using haematoxylin and eosin staining, which requires two consecutive slices of the same tumor, one to be decellularized and another one to be stained. This requirement is incompatible with decellularization of the full organ.
(5) To properly study the tumor ECM, we decided on the thickness of 20 µm to be both suitable for staining and imaging and mechanical testing. Both of these procedures took over one week to produce acellular tissues, required long incubation periods and were performed at high agitation. Tissue sections of 20 µm would be too fragile to endure such a procedure.

For these reasons, we concluded that we needed to develop a new decellularization protocol that would maintain the tumor architecture, be gentle, fast, efficient and capable of preserving the native consecutive sections of the decellularized tissue for further analysis. When developing this necessary tool for our research question, we realized that such a protocol filled an important gap in the decellularization methods literature and could aid in many other research questions. With that in mind, we decided to attempt to decellularize biological samples from different tissues and animal origins whilst attached to a glass slide, thus enabling the decellularization of a single tissue section as opposed to the full organ or tissue block.

To achieve a gentler but highly efficient decellularization, the developed protocol is composed of consecutive washes and rinses of several decellularizing agents with different modes of action, such as hypotonic agents, a surfactant, and an enzymatic reagent. For protocol optimization purposes, we compared the effects on ECM preservation and cellular removal of six decellularizing agents previously described in the literature (72,84,90,94,117,118) and selected SD as the best compromise between decellularization efficiency, ECM preservation and sample detachment. After publishing the work on selecting the best method for on-slide decellularization, and providing information on its mechanical and biochemical effects, as well as its biocompatibility, we decided to publish a second manuscript describing a step-by-step guide of the decellularization protocol, including details on sample preparation and decellularization assessment (*see Scientific Article III in Chapter III*).

The total decellularization time of this protocol was reduced to 2 hours, making it an easy and accessible tool for many applications, such as (1) studies of scarce and

valuable samples, like clinical biopsies and mice embryonic tissues, since it is possible to decellularize sections as thin as 10 µm while leaving the rest of the sample untouched for other clinical testing, like cellular biomarkers; (2) studies that require the identification of cellular regions that can only be detected in native sections, like inflammation hotspots, and thus require consecutive sections where one sample is decellularized and the other is used for region identification; (3) cell culture applications, since the ECM can be used as a substrate for cellular assays and these results can be correlated with features of consecutive native sections, like tumor cell death or LOX expression, and finally, (4) studies that required the mechanical characterization of a sample before and after decellularization, since this protocol allows for the mechanical testing of the exact same structure in both settings. In fact, this method also allows for the "re-decellularization" of tissue sections. In theory, it is possible to mechanically test a native tissue section, decellularize it, perform mechanical characterization again on the ECM scaffold, seed cells of interest (e.g., fibroblasts) on the decellularized tissue, "re-decellularize" it after the cellular assays are complete and mechanically characterize the ECM after cellular remodelling. This feature opens a wide range of possibilities regarding *in vitro* models of ECM remodelling in both health and disease.

The main limitation of the new decellularization procedure, however, is the potential detachment of samples during the consecutive washes and rinses with decellularizing agents. Among all the different tested tissues (lungs, heart, kidneys and bladder), the lung was the only tissue that occasionally detached during decellularization, suggesting that sample detachment is rather tissue dependent and is related to section morphology. In fact, the lungs have some features that complicate their attachment, like the large areas of empty spaces that correspond to the alveoli and airways. The presence of these structures results in a reduced contact area between the tissue and the glass slide in comparison to other tissues. Furthermore, the tissue sample loses all cells during the decellularization procedure, further decreasing the contact area with the glass slide. This hypothesis is consistent with the results obtained, since the most effective decellularizing agents (SD and SDS) had higher detachment rates than less effective treatments, like triton and CHAPS. It is also important to mention that the nature of the surfactant employed might also play a part. In fact, ionic detergents (SDS and SD) caused lower attachment when compared to zwitterionic and non-ionic

detergents (CHAPS and Triton X-100, respectively). We thus hypothesise that the ionic nature of these surfactants reacts with the ionic coating of the glass slides responsible for sample attachment and thus disrupting it. To achieve higher attachment levels in samples such as the lungs, there are several options available, like coating glass slides in gelatin, APTES, transglutaminase or celTAK.

During the development of the 'on-slide' decellularization protocol, there was a need to quantify the decellularization levels (i.e. amount of cellular removal) resulting from each of the decellularizing agents, in order to determine the most efficient method. However, we realized that the standard decellularization quantification methods were not easily applicable to our new section-by-section decellularization approach. The gold-standard for decellularization quantification was to use commercially available DNA quantitation kits, where the sample is digested, the DNA is purified and later measured based on UV-absorbance (83–85). To assess the decellularization degree of tissue sections resulting from the 'on-slide' decellularization method in accordance with the aforementioned gold-standard, we needed to use a cell scraper to remove a minimum of 30 consecutive lung sections from the glass slides in order to amount to the sufficient weight necessary for the subsequent tissue digestion. Although possible, it is extremely time-consuming, delicate, and incompatible with studies where the tissue sections are scarce. When faced with this obstacle, we hypothesised that an image-based method to quantify decellularization via nuclear staining quantification would pose a quicker, cheaper, less wasteful and more reliable alternative.

When reviewing the literature, the majority of the available image-based methods were qualitative, where a H&E (77,78) or DAPI (79,80) stained tissue section was considered 'decellularized' or 'not-decellularized' based on the presence or absence of visible nuclei. To us, a quantitative approach was fundamental since we wanted to establish concrete and statistical relationships regarding decellularization levels. Magliaro et. al developed an open-source, image-based quantitative method for histological sections named 'HisTOOLogy' (119), which was used to quantify the decellularization of liver sections based on H&E staining. It works by counting the number of nuclei in the "decellularized" section and comparing it to the number of nuclei in a corresponding native sample. Although a clear improvement from qualitative methods, this tool has the major drawback of only considering the number

of nuclei as an indicator of decellularization and does not account for the DNA that has been released into the matrix but not fully removed. This parameter is extremely important in decellularization quantification since DNA presence is detrimental for cell culture and tissue engineering applications that often require decellularized tissues (120). Additionally, DNA (and not nuclei) quantification is necessary for the comparison between different decellularizing agents, since many will succeed in lysing cells and partially decellularizing the sample, and some also have the well documented effect of DNA agglutination and attachment to the matrix, like SD (74). For these reasons it was important to develop an automated image-based algorithm that would quantify DNA (and ECM protein presence) before and after decellularization.

The developed algorithm is based on image entropy which is a measure of the morphological heterogeneity that is natural of biological tissues, as opposed to other cell/tissue image segmentation methods which are based in pixel intensity. However, performing segmentation on a tissue imaged based on pixel intensity poses a translational problem, since intensity will depend on microscope setup and magnification. For this specific application, a microscopic image of a tissue before and after decellularization will have completely different intensity profiles since pixel intensity is related to tissue density, and decellularized tissues are much less dense than native tissues due to the loss of the cellular component. Even within a given sample there is a high level of tissue heterogeneity which would translate into intensity heterogeneity as well. For that reason, our entropy-based algorithm is much more universal, and was able to successfully segment bladder, heart, lung and kidney microscopic images without further adjustments. However, since the tissue is detected based on the entropy of the image it is fundamental that the background be as homogeneous and empty as possible, which requires the thorough cleaning of the glass slide before imaging.

The DNA reduction observed after tissue decellularization was extremely similar when comparing the novel image-based method and the standard DNA quantification kits. However, not only are DNA quantification kits more costly and time-consuming, but they typically require a large amount of tissue and yield a single metric – milligrams of DNA per dry weight. Our novel image-based approach, on the other hand, is fully automated and can quantify the DNA presence in tissue sections from dozens of

images in a matter of minutes. In addition, it can simultaneously gather information on the ECM composition after decellularization due to its multichannel image analysis feature. However, it is important to note that this method might not be suited for thicker tissue sections (more than 100 µm), where the opacity of the tissue would hinder the fluorescent signal quantification. In these cases, the DNA quantitation kits still pose a viable alternative. In the future, the algorithm here developed could be expanded to provide further information on the effects of the decellularization procedure on the ECM, like fibre density, protein distribution and tissue structural integrity.

The ‘on-slide’ decellularization method and the image-based algorithm together form a perfectly matched pipeline that is suited for a variety of tissues and research applications. In addition to being used to quantify the cellular removal and ECM preservation of different decellularizing agents, since its publication, this method combination has been used in a bleomycin-induced fibrosis rat model to decellularize the lung ECM and later quantify the decellularization and fibrotic level (fibronectin and elastin presence) of affected lungs, in a paper that has been submitted for review. It has also been used in an ongoing study of the ageing lung ECM, where it has been applied to decellularize the samples, as well as detect ECM changes in the lungs of ageing mice for downstream cell culture applications (expected publication 2023). In both these studies the lung ECM was mechanically characterized by AFM and its mechanical properties were correlated with the biochemical composition of the ECM, further supporting the wide range of research applications this dual method can facilitate.

After establishing the methodology required to produce lung tumor ECM sections, we decided to study the ECM of lung metastases from 2 different origins: exogeneous (melanoma) and endogenous (lung carcinoma). Until now, the tumor extracellular matrix had been classified as disorganized and unstructured (121,122) while desmoplasia in the TME has often been described in the periphery of the tumor alone (24,42). However, after tumor decellularization, we were able to observe distinct ECM structures in the inner and outer regions of the tumor, suggesting a tumor ECM architecture made up of ECM rich and ECM poor areas. Due to the biochemical and morphological signature of these regions, we equated the tumor ECM-rich regions to ECM that was produced by the tumor, or tumor ECM deposition. For the most part,

both ECM-rich and poor regions were present in both metastatic models, even if in different locations and concentrations. Still, AFM measurements showed that the ECM produced by melanoma metastases was significantly stiffer than the ECM produced by the lung carcinoma model, suggesting that ECM production in the tumor is not dependent on the secondary location, but on the primary organ. These findings are consistent with previous reports in a mouse model, which suggested that the mechanical signature of a breast cancer secondary lesion in the lung is consistent with the mechanical signature of the primary breast cancer lesion (106). Further studies should be performed on the ECM of melanoma and lung primary lesions to be able to properly distinguish between those tumor features derived from the lung to which it has metastasized and the primary melanoma/lung microenvironment.

Nonetheless, there were also close similarities between the two metastatic lung tumor models. In fact, even though the early-stage invasion phenotypes were different, the softening of the ECM and the depletion of the basement membrane was nearly identical in the tumor-infiltrated areas of the lung carcinoma and the melanoma micrometastases. Furthermore, both tissues also showed an equal overexpression of fibronectin in these early stages. This similarity suggests that tumor invasion is secondary site dependent, and it progresses in the same manner regardless of the primary lesion: cancer cells leave the primary site and invade the new location through the basement membrane, degrading it and consequently destabilizing the ECM, softening it in the process. Fibronectin is overexpressed either by the invading cancer cells, or by vesicles released by the primary tumor that arrived at the target-site before circulating cancer cells did, in order to establish a tumor-promoting “pre-metastatic” niche (123,124). In any case, fibronectin has been shown to promote tumor engraftment, growth and the depletion of the basement membrane (125), thus facilitating metastases formation.

Fibronectin was not only overexpressed in early stages of invasion but also in the late stages of tumor progression – the macrometastases. The ECM-rich region of both models showed a sharp increase in stiffness when compared to healthy lung tissue and a clear over deposition of fibronectin and collagen type I. However, since the ECM in melanoma macrometastases was much stiffer than in lung macrometastases while their fibronectin content was similar, fibronectin overexpression alone is not enough to

explain the sharp increase in stiffness. This increase could be then due to an ECM protein for which we haven't tested, like osteopontin or tenascin-C, that have been implicated in the breast cancer metastases to the lungs as metastases-promoting components (126,127). Nonetheless, we believe it is more likely that this increase in stiffness is due to the well described overexpression of LOX in tumor miroenvironments (35,109,128). The hypoxia- induced LOX enzyme covalently crosslinks collagens which leads to an increase in tissue stiffness (129,130). Thus, an hypoxic tumor microenvironment leads to LOX overexpression which induces ECM stiffening that will in turn promote angiogenesis by stimulating the release of endothelial growth factors (131). In fact, the first ECM-rich regions, which we hypothesise are produced by the tumor, appear in macrometastases of ~1 mm^3 volume, which is consistent with the reported volume at which tumors switch from relying on direct diffusion from native vasculature to a more angiogenic phenotype, of around 1-2mm^3 (20,132,133). Future works should focus on the effects that different hypoxic conditions have on ECM deposition and stiffness, as well as the specific correlation of LOX activity and tumor ECM characteristics.

Throughout our work, tumor ECM measurements were consistently compared to "healthy" ECM regions of the same tissue section. It could be argued that these "healthy" regions were not truly healthy if they are from the same animal that was previously injected with cancer cells. However, we decided on this methodology to mimic clinical conditions since, in cancer patients, when a biopsy is performed, the suspected tumor tissue is compared with a biopsy from a nearby "healthy" region of the same patient to establish a baseline. Many times, these patients have comorbidities such as COPD or other smoking-related disorders and control biopsies are still not taken from perfectly healthy patients, which would be impractical. Nevertheless, AFM measurements of "healthy" ECM regions of mice injected with either B16-F10 or LLC1 cells were consistent with the AFM measurements of the mice lung ECM used for the development of the decellularization method, where mice were considered to be in perfect health and had not taken part in any disease modelling experiment.

After clearly defining the mechanical and compositional differences between lung metastases' ECM and healthy lung ECM, we wanted to test the hypothesis that ECM-

targeting drugs could affect ECM deposition and stiffness, and potentially lead to a less permissive microenvironment for tumor progression and metastases. For that reason, we chose the melanoma metastasis model since it had shown the most mechanical changes when compared to healthy lung ECM. Surprisingly, our hypothesis was not confirmed, and the opposite was observed: NTD caused a 4-fold increase in ECM deposition and a 2- fold increase in tumor ECM stiffness. Both the increase in ECM deposition and stiffness formed a significant and strong correlation with the sharp increase in tumor cell death caused by NTD's anti-angiogenic effects, which suggests an underlying mechanism linking angiogenesis and/or hypoxia with ECM deposition and mechanics. Once again, a likely suspect of this interaction is the hypoxia-induced LOX enzyme which crosslinks collagen and increases overall ECM stiffness. The anti-fibrotic effects of NTD are yet to be fully elucidated, and other recent disease models have found limited anti-fibrotic effects: recent works have shown no alteration in fibrosis markers or collagen I expression in IPF patients (134,135) and in a brain and breast cancer metastases model, NTD also had no anti-ECM effects (136,137). For these reasons, there are still many unanswered questions regarding NTD therapeutics in cancer. Not only should the relationship between NTD, hypoxia and the ECM be further explored, but future studies should focus on the different effects NTD produces on the tumor ECM, when administered at different time-points, including as a preventative measure (before the injection of metastatic cells).

The findings described throughout this doctoral thesis highlight how the tumor ECM should become an important consideration in a clinical setting. The tumor ECM structures, namely the ECM-rich regions, are not targeted in typical cancer therapeutics and thus, even if malignant cells are completely removed, patients are left with extremely stiff and large fibronectin-rich structures in their lungs. These structures could not only leave them with lifelong breathing difficulties but, since fibronectin is a chemoattractant and promotes tumor growth (125,138), could facilitate "re-invasion" of the tissue. Additionally, the mechanical characterization of the tumor ECM can have applications in diagnostics by distinguishing healthy from malignant (or premalignant) tissue or by determining the invasive potential of a tumour. For instance, Plodinec et al (2012) used AFM to measure the stiffness of breast cancer metastases to the lungs in mice. This study concluded that the mechanical properties of the secondary lesions share distinct stiffness peaks with its primary tumor site (106). For

lung-seeking metastases, if the mechanics of the secondary lesions' ECM is similar to the primary tumor, mechanical measurements of tumor biopsies could aid in the identification of the primary site especially in cases where histological assessment cannot clarify tumor origin (e.g. cancer of unidentified primary, or CUPs). In fact, based on her findings, Plodinec later founded a medical device company based on AFM technology (ARTIDIS) that aims to use the tumor nanomechanical signatures for cancer diagnostics and prognosis in a clinical setting.

In this thesis we have thus described a complete experimental pipeline for studies of the tumor ECM alongside its application to the analysis of the lung metastases' ECM. This pipeline describes every step, from tumor decellularization to decellularization quantification, ECM protein quantification, ECM mechanical characterization and the correlation between cellular tumor features and ECM mechanics. In this work, this methodology allowed for the study of the micromechanical and biochemical properties of the acellular lung tumors in mice, but due to its universal nature, it can also be applied to many other tumor types, as well as to other diseases that are characterized by an aberrant deposition of the extracellular matrix, like IPF, inflammatory bowel disease, cardiac fibrosis and many others. This doctoral thesis can therefore be an invaluable tool to one day incorporating the study of the ECM and its mechanics in every day clinical settings.

Chapter V.

CONCLUSIONS

Conclusions

1. The novel decellularization protocol developed in this project provides a useful tool for many research applications by allowing the simultaneous decellularization and preservation of consecutive native sections in tissues of different organs and origins.

2. The newly described image-based decellularization quantification algorithm poses a viable alternative to the standard DNA quantification methods, since it is cheaper, faster, less wasteful of biological materials, provides information on the sample heterogeneity and can also assess extracellular matrix preservation after decellularization.

3. Different origins of lung metastases result in different extracellular matrix mechanical properties but with similar biochemical composition.

4. The stiffness of lung tumor extracellular matrix changes along with tumor progression: early stages of invasion are characterized by extracellular matrix softening and basement membrane degradation, while later tumorigenic stages are characterized by extracellular matrix stiffening and deposition.

5. Fibronectin plays an important role in all stages of metastatic progression in both endogenous and exogeneous metastatic origins.

6. Tumor necrosis and tumor angiogenesis are intimately connected to extracellular matrix deposition and stiffening.

7. Nintedanib treatment caused increased fibrosis inside the tumor, leading to increased extracellular matrix deposition and stiffening.

Chapter VI.

REFERENCES

References

1. López A, Martinson SA. Respiratory system, mediastinum, and pleurae. In: Pathologic Basis of Veterinary Disease [Internet]. Elsevier; 2017 [cited 2022 Sep 19]. p. 471-560.e1. Available from: https://linkinghub.elsevier.com/retrieve/pii/B9780323357753000096

2. Patwa A, Shah A. Anatomy and physiology of respiratory system relevant to anaesthesia. Indian J Anaesth. 2015 Sep;59(9):533–41.

3. Weibel ER. It takes more than cells to make a good lung. Am J Respir Crit Care Med. 2013 Feb 15;187(4):342–6.

4. Damjanov I. Pathophysiology [E-book] [Internet]. 1st edition. Elsevier Health Sciences; 2008 [cited 2022 Sep 19]. Available from: https://books.google.ch/books?hl=en&lr=&id=fy8gb5zThOgC&oi=fnd&pg=PP1&dq=Pathophysiology+ivan+&ots=4qIsnrroXE&sig=o7jRaZEVBUrzgoWJIR1KNpNZQP8&redir_esc=y#v=onepage&q&f=false

5. Han S, Mallampalli RK. The role of surfactant in lung disease and host defense against pulmonary infections. Ann Am Thorac Soc. 2015 May;12(5):765–74.

6. Knudsen L, Ochs M. The micromechanics of lung alveoli: structure and function of surfactant and tissue components. Histochem Cell Biol. 2018 Dec;150(6):661–76.

7. Siegel RL, Miller KD, Fuchs HE, Jemal A. Cancer statistics, 2021. CA Cancer J Clin. 2021 Jan;71(1):7–33.

8. Cryer AM, Thorley AJ. Nanotechnology in the diagnosis and treatment of lung cancer. Pharmacol Ther. 2019 Jun;198:189–205.

9. de Groot PM, Wu CC, Carter BW, Munden RF. The epidemiology of lung cancer. Transl Lung Cancer Res. 2018 Jun;7(3):220–33.

10. Chen Z, Fillmore CM, Hammerman PS, Kim CF, Wong KK. Non-small-cell lung cancers: a heterogeneous set of diseases. Nat Rev Cancer. 2014 Aug;14(8):535–46.

11. Travis WD. Pathology of lung cancer. Clin Chest Med. 2011 Dec;32(4):669–92.

12. Abdel-Rahman O. Correlation between PD-L1 expression and outcome of NSCLC patients treated with anti-PD-1/PD-L1 agents: A meta-analysis. Crit Rev Oncol Hematol. 2016 May;101:75–85.

13. Tu J, Xu H, Ma L, Li C, Qin W, Chen X, et al. Nintedanib enhances the efficacy of PD-L1 blockade by upregulating MHC-I and PD-L1 expression in tumor cells. Theranostics. 2022;12(2):747–66.

14. Pawelczyk K, Piotrowska A, Ciesielska U, Jablonska K, Gletzel-Plucinska N, Grzegrzolka J, et al. Role of pd-l1 expression in non-small cell lung cancer and their prognostic significance according to clinicopathological factors and diagnostic markers. Int J Mol Sci. 2019 Feb;20(4):824.

15. Ruscitto F, Roda N, Priami C, Migliaccio E, Pelicci PG. Beyond genetics: metastasis as an adaptive response in breast cancer. Int J Mol Sci. 2022 Jun 3;23(11):6271.

16. Yilmaz M, Christofori G. EMT, the cytoskeleton, and cancer cell invasion. Cancer Metastasis Rev. 2009 Jun;28(1–2):15–33.

17. Fischer KR, Durrans A, Lee S, Sheng J, Li F, Wong STC, et al. Epithelial-to-mesenchymal transition is not required for lung metastasis but contributes to chemoresistance. Nature. 2015 Nov;527(7579):472–6.

18. Popper HH. Progression and metastasis of lung cancer. Cancer Metastasis Rev. 2016 Mar;35(1):75–91.

19. Guan X. Cancer metastases: challenges and opportunities. Acta Pharm Sin B. 2015 Sep;5(5):402–18.

20. Anderson NM, Simon MC. The tumor microenvironment. Curr Biol. 2020 Aug;30(16):R921–5.

21. Muramatsu M, Akakura S, Gao L, Peresie J, Balderman B, Gelman IH. SSeCKS/Akap12 suppresses metastatic melanoma lung colonization by attenuating Src-mediated pre-metastatic niche crosstalk. Oncotarget. 2018 Sep;9(71):33515–27.

22. Altorki NK, Markowitz GJ, Gao D, Port JL, Saxena A, Stiles B, et al. The lung microenvironment: an important regulator of tumour growth and metastasis. Nat Rev Cancer. 2019 Jan;19(1):9–31.

23. Mohammed TLH, Chowdhry A, Amorosa JK, Ginsburg ME, Heitkamp DE, MacMahon H, et al. Acr appropriateness criterias screening for pulmonary metastases. J Thorac Imaging. 2011 Feb;26(1):W1-3.

24. Stella GM, Kolling S, Benvenuti S, Bortolotto C. Lung-seeking metastases. Cancers. 2019 Jul;11(7):1010.

25. Makino A, Tsuruta M, Okabayashi K, Ishida T, Shigeta K, Seishima R, et al. The impact of smoking on pulmonary metastasis in colorectal cancer. OncoTargets Ther. 2020 Sep;13:9623–9.

26. Abrams JA, Lee PC, Port JL, Altorki NK, Neugut AI. Cigarette smoking and risk of lung metastasis from esophageal cancer. Cancer Epidemiol Biomarkers Prev. 2008 Oct;17(10):2707–13.

27. Burgstaller G, Oehrle B, Gerckens M, White ES, Schiller HB, Eickelberg O. The instructive extracellular matrix of the lung: basic composition and alterations in chronic lung disease. Eur Respir J. 2017 Jul;50(1):1601805.

28. Pompili S, Latella G, Gaudio E, Sferra R, Vetuschi A. The charming world of the extracellular matrix: a dynamic and protective network of the intestinal wall. Front Med. 2021 Apr;8:610189.

29. Gattazzo F, Urciuolo A, Bonaldo P. Extracellular matrix: A dynamic microenvironment for stem cell niche. Biochim Biophys Acta BBA - Gen Subj. 2014 Aug;1840(8):2506–19.

30. Burgess JK, Mauad T, Tjin G, Karlsson JC, Westergren-Thorsson G. The Extracellular Matrix – the under-recognised element in lung disease? J Pathol. 2016 Dec;240(4):397–409.

31. Grau-Bové X, Ruiz-Trillo I, Rodriguez-Pascual F. Origin and evolution of lysyl oxidases. Sci Rep. 2015 Sep;5(1):10568.

32. Suki B, Bates JHT. Extracellular matrix mechanics in lung parenchymal diseases. Respir Physiol Neurobiol. 2008 Nov;163(1–3):33–43.

33. Balestrini JL, Niklason LE. Extracellular matrix as a driver for lung regeneration. Ann Biomed Eng. 2015 Mar;43(3):568–76.

34. Ariza de Schellenberger A, Bergs J, Sack I, Taupitz M. The extracellular matrix as a target for biophysical and molecular magnetic resonance imaging. In: Sack I, Schaeffter T, editors. Quantification of biophysical parameters in medical imaging [Internet]. Cham: Springer International Publishing; 2018 [cited 2022 Nov 28]. p. 123–50. Available from: http://link.springer.com/10.1007/978-3-319-65924-4_6

35. Barker HE, Chang J, Cox TR, Lang G, Bird D, Nicolau M, et al. Loxl2-mediated matrix remodeling in metastasis and mammary gland involution. Cancer Res. 2011 Mar;71(5):1561–72.

36. Chen L, Li S, Li W. LOX/LOXL in pulmonary fibrosis: potential therapeutic targets. J Drug Target. 2019 Aug;27(7):790–6.

37. Huang C, Chen J. Laminin-332 mediates proliferation, apoptosis, invasion, migration and epithelial-to-mesenchymal transition in pancreatic ductal adenocarcinoma. Mol Med Rep. 2020 Nov 3;23(1):1–1.

38. Roman J. Fibronectin and fibronectin receptors in lung development. Exp Lung Res. 1997 Jan;23(2):147–59.

39. Boedtkjer E, Pedersen SF. The acidic tumor microenvironment as a driver of cancer. Annu Rev Physiol. 2020 Feb 10;82(1):103–26.

40. Ribeiro Franco PI, Rodrigues AP, de Menezes LB, Pacheco Miguel M. Tumor microenvironment components: Allies of cancer progression. Pathol - Res Pract. 2020 Jan;216(1):152729.

41. Ghajar CM, Correia AL, Bissell MJ. The role of the microenvironment in tumor initiation, progression, and metastasis. In: The Molecular Basis of Cancer

[Internet]. Elsevier; 2015 [cited 2022 Jul 3]. p. 239-256.e5. Available from: https://linkinghub.elsevier.com/retrieve/pii/B9781455740666000160

42. Conti JA, Kendall TJ, Bateman A, Armstrong TA, Papa-Adams A, Xu Q, et al. The desmoplastic reaction surrounding hepatic colorectal adenocarcinoma metastases aids tumor growth and survival via αv integrin ligation. Clin Cancer Res. 2008 Oct 15;14(20):6405–13.

43. Schober M, Jesenofsky R, Faissner R, Weidenauer C, Hagmann W, Michl P, et al. Desmoplasia and chemoresistance in pancreatic cancer. Cancers. 2014 Oct 21;6(4):2137–54.

44. Mueller MM, Fusenig NE. Friends or foes — bipolar effects of the tumour stroma in cancer. Nat Rev Cancer. 2004 Nov;4(11):839–49.

45. Qiu X, Tan H, Fu D, Zhu Y, Zhang J. Laminin is over expressed in breast cancer and facilitate cancer cell metastasis. J Cancer Res Ther. 2018 Dec;14(12):1170.

46. Provenzano PP, Inman DR, Eliceiri KW, Knittel JG, Yan L, Rueden CT, et al. Collagen density promotes mammary tumor initiation and progression. BMC Med. 2008 Dec;6(1):11.

47. Mammoto T, Jiang A, Jiang E, Panigrahy D, Kieran MW, Mammoto A. Role of collagen matrix in tumor angiogenesis and glioblastoma multiforme progression. Am J Pathol. 2013 Oct;183(4):1293–305.

48. Cho C, Horzempa C, Longo CM, Peters DM, Jones DM, McKeown-Longo PJ. Fibronectin in the tumor microenvironment activates a tlr4-dependent inflammatory response in lung cancer cells. J Cancer. 2020 Mar;11(11):3099–105.

49. Qin S, Zhang B, Xiao G, Sun X, Li G, Huang G, et al. Fibronectin protects lung cancer cells against docetaxel-induced apoptosis by promoting Src and caspase-8 phosphorylation. Tumor Biol. 2016 Oct;37(10):13509–20.

50. Götte M, Kovalszky I. Extracellular matrix functions in lung cancer. Matrix Biol. 2018 Nov;73:105–21.

51. Sofeu Feugaing DD, Götte M, Viola M. More than matrix: The multifaceted role of decorin in cancer. Eur J Cell Biol. 2013 Jan;92(1):1–11.

52. Yang N, Mosher R, Seo S, Beebe D, Friedl A. Syndecan-1 in breast cancer stroma fibroblasts regulates extracellular matrix fiber organization and carcinoma cell motility. Am J Pathol. 2011 Jan;178(1):325–35.

53. Provenzano PP, Inman DR, Eliceiri KW, Trier SM, Keely PJ. Contact guidance mediated three-dimensional cell migration is regulated by rho/rock-dependent matrix reorganization. Biophys J. 2008 Dec;95(11):5374–84.

54. Conklin MW, Eickhoff JC, Riching KM, Pehlke CA, Eliceiri KW, Provenzano PP, et al. Aligned collagen is a prognostic signature for survival in human breast carcinoma. Am J Pathol. 2011 Mar;178(3):1221–32.

55. Kunz LIZ, Strebus J, Budulac SE, Lapperre TS, Sterk PJ, Postma DS, et al. Inhaled steroids modulate extracellular matrix composition in bronchial biopsies of copd patients: a randomized, controlled trial. Taube C, editor. PLoS ONE. 2013 May 7;8(5):e63430.

56. de Kluijver J, Schrumpf JA, Evertse CE, Sont JK, Roughley PJ, Rabe KF, et al. Bronchial matrix and inflammation respond to inhaled steroids despite ongoing allergen exposure in asthma. Clin Htmlent Glyphamp Asciiamp Exp Allergy. 2005 Oct;35(10):1361–9.

57. Roth GJ, Binder R, Colbatzky F, Dallinger C, Schlenker-Herceg R, Hilberg F, et al. Nintedanib: from discovery to the clinic. J Med Chem. 2015 Feb 12;58(3):1053–63.

58. Ruwanpura SM, Thomas BJ, Bardin PG. Pirfenidone: molecular mechanisms and potential clinical applications in lung disease. Am J Respir Cell Mol Biol. 2020 Apr;62(4):413–22.

59. Song W, Kuang J, Li CX, Zhang M, Zheng D, Zeng X, et al. Enhanced immunotherapy based on photodynamic therapy for both primary and lung metastasis tumor eradication. ACS Nano. 2018 Feb 27;12(2):1978–89.

60. Awasthi N, Schwarz R. Profile of nintedanib in the treatment of solid tumors: the evidence to date. OncoTargets Ther. 2015 Dec;8:3691.

61. Levental KR, Yu H, Kass L, Lakins JN, Egeblad M, Erler JT, et al. Matrix crosslinking forces tumor progression by enhancing integrin signaling. Cell. 2009 Nov;139(5):891–906.

62. Saatci O, Kaymak A, Raza U, Ersan PG, Akbulut O, Banister CE, et al. Targeting lysyl oxidase (LOX) overcomes chemotherapy resistance in triple negative breast cancer. Nat Commun. 2020 Dec;11(1):2416.

63. Duch P, Díaz-Valdivia N, Ikemori R, Gabasa M, Radisky ES, Arshakyan M, et al. Aberrant TIMP-1 overexpression in tumor-associated fibroblasts drives tumor progression through CD63 in lung adenocarcinoma. Matrix Biol. 2022 Aug;111:207–25.

64. Liu YT, Sun ZJ. Turning cold tumors into hot tumors by improving T-cell infiltration. Theranostics. 2021 Mar;11(11):5365–86.

65. Ren X, Guo S, Guan X, Kang Y, Liu J, Yang X. Immunological classification of tumor types and advances in precision combination immunotherapy. Front Immunol. 2022 Feb 28;13:790113.

66. Ohata K, Ott HC. Human-scale lung regeneration based on decellularized matrix scaffolds as a biologic platform. Surg Today. 2020 Jul;50(7):633–43.

67. Agmon G, Christman KL. Controlling stem cell behavior with decellularized extracellular matrix scaffolds. Curr Opin Solid State Mater Sci. 2016 Aug;20(4):193–201.

68. Marhuenda E, Villarino A, Narciso ML, Camprubí-Rimblas M, Farré R, Gavara N, et al. Lung Extracellular Matrix Hydrogels Enhance Preservation of Type II Phenotype in Primary Alveolar Epithelial Cells. Int J Mol Sci. 2022 Apr 28;23(9):4888.

69. Júnior C, Narciso M, Marhuenda E, Almendros I, Farré R, Navajas D, et al. Baseline stiffness modulates the non-linear response to stretch of the extracellular matrix in pulmonary fibrosis. Int J Mol Sci. 2021 Nov 29;22(23):12928.

70. Mendibil U, Ruiz-Hernandez R, Retegi-Carrion S, Garcia-Urquia N, Olalde-Graells B, Abarrategi A. Tissue-specific decellularization methods: rationale and strategies to achieve regenerative compounds. Int J Mol Sci. 2020 Jul 30;21(15):5447.

71. Choudhury D, Yee M, Sheng ZLJ, Amirul A, Naing MW. Decellularization systems and devices: State-of-the-art. Acta Biomater. 2020 Oct;115:51–9.

72. Jorba I, Beltrán G, Falcones B, Suki B, Farré R, García-Aznar JM, et al. Nonlinear elasticity of the lung extracellular microenvironment is regulated by macroscale tissue strain. Acta Biomater. 2019 Jul;92:265–76.

73. Wüthrich T, Lese I, Haberthür D, Zubler C, Hlushchuk R, Hewer E, et al. Development of vascularized nerve scaffold using perfusion-decellularization and recellularization. Mater Sci Eng C. 2020 Dec;117:111311.

74. Gilpin A, Yang Y. Decellularization strategies for regenerative medicine: from processing techniques to applications. BioMed Res Int. 2017;2017:1–13.

75. Seddon AM, Curnow P, Booth PJ. Membrane proteins, lipids and detergents: not just a soap opera. Biochim Biophys Acta BBA - Biomembr. 2004 Nov;1666(1–2):105–17.

76. le Maire M, Champeil P, Møller JV. Interaction of membrane proteins and lipids with solubilizing detergents. Biochim Biophys Acta BBA - Biomembr. 2000 Nov;1508(1–2):86–111.

77. Hsieh DJ, Srinivasan P, Yen KC, Yeh YC, Chen YJ, Wang HC, et al. Protocols for the preparation and characterization of decellularized tissue and organ scaffolds for tissue engineering. BioTechniques. 2021 Feb;70(2):107–15.

78. Alshaikh AB, Padma AM, Dehlin M, Akouri R, Song MJ, Brännström M, et al. Decellularization and recellularization of the ovary for bioengineering applications; studies in the mouse. Reprod Biol Endocrinol. 2020 Dec;18(1):75.

79. Nonaka PN, Campillo N, Uriarte JJ, Garreta E, Melo E, de Oliveira LVF, et al. Effects of freezing/thawing on the mechanical properties of decellularized lungs: decellularized lung mechanics after freezing/thawing. J Biomed Mater Res A. 2014 Feb;102(2):413–9.

80. Hoshiba T, Lu H, Kawazoe N, Chen G. Decellularized matrices for tissue engineering. Expert Opin Biol Ther. 2010 Dec;10(12):1717–28.

81. Fischer I, Westphal M, Rossbach B, Bethke N, Hariharan K, Ullah I, et al. Comparative characterization of decellularized renal scaffolds for tissue engineering. Biomed Mater. 2017 Jul 4;12(4):045005.

82. Zhang J, Hu ZQ, Turner NJ, Teng SF, Cheng WY, Zhou HY, et al. Perfusion-decellularized skeletal muscle as a three-dimensional scaffold with a vascular network template. Biomaterials. 2016 May;89:114–26.

83. Lü WD, Zhang L, Wu CL, Liu ZG, Lei GY, Liu J, et al. Development of an acellular tumor extracellular matrix as a three-dimensional scaffold for tumor engineering. Burns JS, editor. PLoS ONE. 2014 Jul 29;9(7):e103672.

84. Xiong G, Flynn TJ, Chen J, Trinkle C, Xu R. Development of an *ex vivo* breast cancer lung colonization model utilizing a decellularized lung matrix. Integr Biol. 2015 Dec 30;7(12):1518–25.

85. Shojaie S, Ermini L, Ackerley C, Wang J, Chin S, Yeganeh B, et al. Acellular lung scaffolds direct differentiation of endoderm to functional airway epithelial cells: requirement of matrix-bound hs proteoglycans. Stem Cell Rep. 2015 Mar;4(3):419–30.

86. Crapo PM, Gilbert TW, Badylak SF. An overview of tissue and whole organ decellularization processes. Biomaterials. 2011 Apr;32(12):3233–43.

87. Pouliot RA, Link PA, Mikhaiel NS, Schneck MB, Valentine MS, Kamga Gninzeko FJ, et al. Development and characterization of a naturally derived lung extracellular matrix hydrogel. J Biomed Mater Res A. 2016 Aug;104(8):1922–35.

88. Sullivan DC, Mirmalek-Sani SH, Deegan DB, Baptista PM, Aboushwareb T, Atala A, et al. Decellularization methods of porcine kidneys for whole organ engineering using a high-throughput system. Biomaterials. 2012 Nov;33(31):7756–64.

89. Yam GHF, Yusoff NZBM, Goh TW, Setiawan M, Lee XW, Liu YC, et al. Decellularization of human stromal refractive lenticules for corneal tissue engineering. Sci Rep. 2016 Sep;6(1):26339.

90. Rosmark O, Åhrman E, Müller C, Elowsson Rendin L, Eriksson L, Malmström A, et al. Quantifying extracellular matrix turnover in human lung scaffold cultures. Sci Rep. 2018 Dec;8(1):5409.

91. Wishart AL, Conner SJ, Guarin JR, Fatherree JP, Peng Y, McGinn RA, et al. Decellularized extracellular matrix scaffolds identify full-length collagen VI as a driver of breast cancer cell invasion in obesity and metastasis. Sci Adv. 2020 Oct;6(43):eabc3175.

92. Hill RC, Calle EA, Dzieciatkowska M, Niklason LE, Hansen KC. Quantification of extracellular matrix proteins from a rat lung scaffold to provide a molecular readout for tissue engineering. Mol Cell Proteomics. 2015 Apr;14(4):961–73.

93. Maghsoudlou P, Georgiades F, Tyraskis A, Totonelli G, Loukogeorgakis SP, Orlando G, et al. Preservation of micro-architecture and angiogenic potential in a

pulmonary acellular matrix obtained using intermittent intra-tracheal flow of detergent enzymatic treatment. Biomaterials. 2013 Sep;34(28):6638–48.

94. Mendoza-Novelo B, Avila EE, Cauich-Rodríguez JV, Jorge-Herrero E, Rojo FJ, Guinea GV, et al. Decellularization of pericardial tissue and its impact on tensile viscoelasticity and glycosaminoglycan content. Acta Biomater. 2011 Mar;7(3):1241–8.

95. Calle EA, Hill RC, Leiby KL, Le AV, Gard AL, Madri JA, et al. Targeted proteomics effectively quantifies differences between native lung and detergent-decellularized lung extracellular matrices. Acta Biomater. 2016 Dec;46:91–100.

96. Trubelja A, Bao G. Molecular mechanisms of mechanosensing and mechanotransduction in living cells. Extreme Mech Lett. 2018 Apr;20:91–8.

97. Engler AJ, Sen S, Sweeney HL, Discher DE. Matrix elasticity directs stem cell lineage specification. Cell. 2006 Aug;126(4):677–89.

98. Rhee WJ, Ni CW, Zheng Z, Chang K, Jo H, Bao G. HuR regulates the expression of stress-sensitive genes and mediates inflammatory response in human umbilical vein endothelial cells. Proc Natl Acad Sci. 2010 Apr 13;107(15):6858–63.

99. Marchioni A, Tonelli R, Cerri S, Castaniere I, Andrisani D, Gozzi F, et al. Pulmonary stretch and lung mechanotransduction: implications for progression in the fibrotic lung. Int J Mol Sci. 2021 Jun 16;22(12):6443.

100. Chen CS. Mechanotransduction – a field pulling together? J Cell Sci. 2008 Oct 15;121(20):3285–92.

101. Qian L, Zhao H. Nanoindentation of soft biological materials. Micromachines. 2018 Dec 11;9(12):654.

102. Fischer-Cripps AC. A review of analysis methods for sub-micron indentation testing. Vacuum. 2000 Sep;58(4):569–85.

103. Alcaraz J, Buscemi L, Grabulosa M, Trepat X, Fabry B, Farré R, et al. Microrheology of human lung epithelial cells measured by atomic force microscopy. Biophys J. 2003 Mar;84(3):2071–9.

104. Alibert C, Goud B, Manneville JB. Are cancer cells really softer than normal cells?: Mechanics of cancer cells. Biol Cell. 2017 May;109(5):167–89.

105. Lekka M, Laidler P, Gil D, Lekki J, Stachura Z, Hrynkiewicz AZ. Elasticity of normal and cancerous human bladder cells studied by scanning force microscopy. Eur Biophys J. 1999 May 25;28(4):312–6.

106. Plodinec M, Loparic M, Monnier CA, Obermann EC, Zanetti-Dallenbach R, Oertle P, et al. The nanomechanical signature of breast cancer. Nat Nanotechnol. 2012 Nov;7(11):757–65.

107. Ansardamavandi A, Tafazzoli-Shadpour M, Omidvar R, Jahanzad I. Quantification of effects of cancer on elastic properties of breast tissue by Atomic Force Microscopy. J Mech Behav Biomed Mater. 2016 Jul;60:234–42.

108. Panzetta V, Musella I, Rapa I, Volante M, Netti PA, Fusco S. Mechanical phenotyping of cells and extracellular matrix as grade and stage markers of lung tumor tissues. Acta Biomater. 2017 Jul;57:334–41.

109. Baker AM, Bird D, Lang G, Cox TR, Erler JT. Lysyl oxidase enzymatic function increases stiffness to drive colorectal cancer progression through FAK. Oncogene. 2013 Apr 4;32(14):1863–8.

110. Ulbricht A, Eppler FJ, Tapia VE, van der Ven PFM, Hampe N, Hersch N, et al. Cellular mechanotransduction relies on tension-induced and chaperone-assisted autophagy. Curr Biol. 2013 Mar;23(5):430–5.

111. Pankova D, Jiang Y, Chatzifrangkeskou M, Vendrell I, Buzzelli J, Ryan A, et al. RASSF 1A controls tissue stiffness and cancer stem-like cells in lung adenocarcinoma. EMBO J. 2019 Jul;38(13):e100532.

112. Alonso-Nocelo M, Raimondo TM, Vining KH, López-López R, de la Fuente M, Mooney DJ. Matrix stiffness and tumor-associated macrophages modulate epithelial to mesenchymal transition of human adenocarcinoma cells. Biofabrication. 2018 Mar 28;10(3):035004.

113. Nagelkerke A, Bussink J, Rowan AE, Span PN. The mechanical microenvironment in cancer: How physics affects tumours. Semin Cancer Biol. 2015 Dec;35:62–70.

114. Voutouri C, Stylianopoulos T. Accumulation of mechanical forces in tumors is related to hyaluronan content and tissue stiffness. Garikipati K, editor. PLOS ONE. 2018 Mar 21;13(3):e0193801.

115. Notari M, Ventura-Rubio A, Bedford-Guaus SJ, Jorba I, Mulero L, Navajas D, et al. The local microenvironment limits the regenerative potential of the mouse neonatal heart. Sci Adv. 2018 May;4(5):eaao5553.

116. Romero-López M, Trinh AL, Sobrino A, Hatch MMS, Keating MT, Fimbres C, et al. Recapitulating the human tumor microenvironment: Colon tumor-derived extracellular matrix promotes angiogenesis and tumor cell growth. Biomaterials. 2017 Feb;116:118–29.

117. Ng WH, Ramasamy R, Yong YK, Ngalim SH, Lim V, Shaharuddin B, et al. Extracellular matrix from decellularized mesenchymal stem cells improves cardiac gene expressions and oxidative resistance in cardiac C-kit cells. Regen Ther. 2019 Dec;11:8–16.

118. Schenke-Layland K, Vasilevski O, Opitz F, König K, Riemann I, Halbhuber KJ, et al. Impact of decellularization of xenogeneic tissue on extracellular matrix integrity for tissue engineering of heart valves. J Struct Biol. 2003 Sep;143(3):201–8.

119. Magliaro C, Tirella A, Mattei G, Pirone A, Ahluwalia A. HisTOOLogy: an open-source tool for quantitative analysis of histological sections: H IS TOOL OGY. J Microsc. 2015 Dec;260(3):260–7.

120. Hussein KH, Park KM, Kang KS, Woo HM. Biocompatibility evaluation of tissue-engineered decellularized scaffolds for biomedical application. Mater Sci Eng C. 2016 Oct;67:766–78.

121. Henke E, Nandigama R, Ergün S. Extracellular matrix in the tumor microenvironment and its impact on cancer therapy. Front Mol Biosci. 2020 Jan 31;6:160.

122. Lu P, Weaver VM, Werb Z. The extracellular matrix: A dynamic niche in cancer progression. J Cell Biol. 2012 Feb 20;196(4):395–406.

123. Chen X, Feng J, Chen W, Shao S, Chen L, Wan H. Small extracellular vesicles: from promoting pre-metastatic niche formation to therapeutic strategies in breast cancer. Cell Commun Signal. 2022 Sep 12;20(1):141.

124. Costa-Silva B, Aiello NM, Ocean AJ, Singh S, Zhang H, Thakur BK, et al. Pancreatic cancer exosomes initiate pre-metastatic niche formation in the liver. Nat Cell Biol. 2015 Jun;17(6):816–26.

125. Lin TC, Yang CH, Cheng LH, Chang WT, Lin YR, Cheng HC. Fibronectin in cancer: friend or foe. Cells. 2019 Dec 20;9(1):27.

126. Oskarsson T, Acharyya S, Zhang XHF, Vanharanta S, Tavazoie SF, Morris PG, et al. Breast cancer cells produce tenascin C as a metastatic niche component to colonize the lungs. Nat Med. 2011 Jul;17(7):867–74.

127. Insua-Rodríguez J, Pein M, Hongu T, Meier J, Descot A, Lowy CM, et al. Stress signaling in breast cancer cells induces matrix components that promote chemoresistant metastasis. EMBO Mol Med [Internet]. 2018 Oct [cited 2022 Oct 13];10(10). Available from: https://onlinelibrary.wiley.com/doi/10.15252/emmm.201809003

128. Wei B, Zhou X, Liang C, Zheng X, Lei P, Fang J, et al. Human colorectal cancer progression correlates with LOX-induced ECM stiffening. Int J Biol Sci. 2017;13(11):1450–7.

129. Gilkes DM, Bajpai S, Chaturvedi P, Wirtz D, Semenza GL. Hypoxia-inducible factor 1 (HIF-1) promotes extracellular matrix remodeling under hypoxic conditions by inducing P4HA1, P4HA2, and PLOD2 expression in fibroblasts. J Biol Chem. 2013 Apr;288(15):10819–29.

130. Pez F, Dayan F, Durivault J, Kaniewski B, Aimond G, Le Provost GS, et al. The HIF-1–inducible lysyl oxidase activates HIF-1 via the akt pathway in a positive regulation loop and synergizes with HIF-1 in promoting tumor cell growth. Cancer Res. 2011 Mar 1;71(5):1647–57.

131. Laczko R, Csiszar K. Lysyl oxidase (LOX): Functional contributions to signaling pathways. Biomolecules. 2020 Jul 22;10(8):1093.

132. Ribatti D. Judah Folkman, a pioneer in the study of angiogenesis. Angiogenesis. 2008 Mar;11(1):3–10.

133. Hillen F, Griffioen AW. Tumour vascularization: sprouting angiogenesis and beyond. Cancer Metastasis Rev. 2007 Dec;26(3–4):489–502.

134. Lehmann M, Buhl L, Alsafadi HN, Klee S, Hermann S, Mutze K, et al. Differential effects of nintedanib and pirfenidone on lung alveolar epithelial cell function in ex vivo murine and human lung tissue cultures of pulmonary fibrosis. Respir Res. 2018 Dec;19(1):175.

135. Decaris ML, Schaub JR, Chen C, Cha J, Lee GG, Rexhepaj M, et al. Dual inhibition of αvβ6 and αvβ1 reduces fibrogenesis in lung tissue explants from patients with IPF. Respir Res. 2021 Dec;22(1):265.

136. Brooks D, Zimmer A, Wakefield L, Lyle LT, Difilippantonio S, Tucci FC, et al. Limited fibrosis accompanies triple-negative breast cancer metastasis in multiple model systems and is not a preventive target. Oncotarget. 2018 May 4;9(34):23462–81.

137. Kovalchuk B, Berghoff AS, Karreman MA, Frey K, Piechutta M, Fischer M, et al. Nintedanib and a bi-specific anti-VEGF/Ang2 nanobody selectively prevent brain metastases of lung adenocarcinoma cells. Clin Exp Metastasis. 2020 Dec;37(6):637–48.

138. Ghura H, Keimer M, von Au A, Hackl N, Klemis V, Nakchbandi IA. Inhibition of fibronectin accumulation suppresses tumor growth. Neoplasia. 2021 Sep;23(9):837–50.